

## Development of Quenching and Partitioning Processed Martensitic Stainless Steels: Microstructure Evolution and Corrosion

Li, Gaojie

**DOI**

[10.4233/uuid:3fd6abe0-149c-409a-b8a3-6e04f97e9376](https://doi.org/10.4233/uuid:3fd6abe0-149c-409a-b8a3-6e04f97e9376)

**Publication date**

2025

**Document Version**

Final published version

**Citation (APA)**

Li, G. (2025). *Development of Quenching and Partitioning Processed Martensitic Stainless Steels: Microstructure Evolution and Corrosion*. [Dissertation (TU Delft), Delft University of Technology]. <https://doi.org/10.4233/uuid:3fd6abe0-149c-409a-b8a3-6e04f97e9376>

**Important note**

To cite this publication, please use the final published version (if applicable). Please check the document version above.

**Copyright**

Other than for strictly personal use, it is not permitted to download, forward or distribute the text or part of it, without the consent of the author(s) and/or copyright holder(s), unless the work is under an open content license such as Creative Commons.

**Takedown policy**

Please contact us and provide details if you believe this document breaches copyrights. We will remove access to the work immediately and investigate your claim.

**Development of Quenching and Partitioning  
Processed Martensitic Stainless Steels:  
Microstructure Evolution and Corrosion**

**Gaojie LI**



# **Development of Quenching and Partitioning Processed Martensitic Stainless Steels: Microstructure Evolution and Corrosion**

## **Dissertation**

for the purpose of obtaining the degree of doctor  
at Delft University of Technology,  
by the authority of the Rector Magnificus prof. dr. ir. T.H.J.J. van der Hagen,  
chair of the Board for Doctorates,  
to be defended publicly on  
Monday 3 March 2025 at 12:30 hours

by

**Gaojie LI**

Master of Engineering in Materials Science and Engineering,  
University of Science and Technology Beijing, China,  
born in Shandong, China.

This dissertation has been approved by the promotor.

Composition of the doctoral committee:

Rector Magnificus	Chairperson
Prof. dr. M.J. Santofimia Navarro	Delft University of Technology, promotor
Dr. Y. Gonzalez-Garcia	Delft University of Technology, copromotor

Independent members:

Prof. dr. ir. H.E.J.G. Schlangen	Delft University of Technology
Prof. dr. ir. R.H. Petrov	Ghent University, Belgium
Prof. dr. I. De Graeve	Vrije Universiteit Brussel, Belgium
Dr. D. San Martin	CENIM-CSIC, Spain

Reserve member:

Prof. dr. J. Dik	Delft University of Technology
------------------	--------------------------------

The research described in this dissertation was carried out in the Department of Materials Science and Engineering at Delft University of Technology, The Netherlands.

This research was carried out with the financial support of the Research Fund for Coal and Steel (RFCS) through the RFCS Grant, proposal number 847195.



*Printed by: Ridderprint || [www.ridderprint.nl](http://www.ridderprint.nl)*

*Cover by: Patrick Jakhari Sanders | [www.ridderprint.nl](http://www.ridderprint.nl)*

Copyright © 2025 by Gaojie LI

ISBN 978-94-6506-939-5

An electronic version of this dissertation is available at TU Delft repository.

# Contents

<b>Summary .....</b>	<b>vii</b>
<b>Samenvatting.....</b>	<b>ix</b>
<b>1 Introduction .....</b>	<b>1</b>
1.1 State of the Art.....	3
1.2 Research Objectives.....	7
1.3 Outline .....	8
<b>2 Heat Treatment and Chemical Composition.....</b>	<b>15</b>
2.1 Introduction .....	17
2.2 Materials and Experimental Methods .....	17
2.3 Design of Heat Treatments .....	19
2.4 Results and Discussion .....	29
2.5 Summary.....	33
<b>3 Microstructure Development of Q&amp;P Processed Martensitic Stainless Steels with Different Manganese Content.....</b>	<b>37</b>
3.1 Introduction .....	39
3.2 Materials and Experimental Methods .....	41
3.3 Heat Treatments.....	43
3.4 Results .....	46
3.5 Discussion.....	54
3.6 Conclusions .....	63
<b>4 Investigation of the Microstructure Development during Partitioning after Room Temperature Quenching.....</b>	<b>69</b>
4.1 Introduction .....	71
4.2 Approach .....	72
4.3 Results .....	74
4.4 Discussion.....	79
4.5 Conclusions .....	84
<b>5 Pit Initiation in Quenching and Partitioning Processed Martensitic Stainless Steels .....</b>	<b>89</b>

5.1 Introduction.....	91
5.2 Experimental Procedure.....	92
5.3 Results.....	95
5.4 Discussion.....	106
5.5 Conclusions.....	109
<b>6 Intergranular Corrosion of TiNb-microalloyed Martensitic Stainless Steels Processed by Quenching and Partitioning.....</b>	<b>117</b>
6.1 Introduction.....	119
6.2 Experimental Procedure.....	120
6.3 Results.....	122
6.4 Discussion.....	130
6.5 Conclusions.....	132
<b>7 General Discussions and Conclusions .....</b>	<b>137</b>
<b>Appendix.....</b>	<b>143</b>
A: Supplementary Materials of Chapter 4 .....	143
B: Supplementary Materials of Chapter 5 .....	147
<b>Acknowledgement .....</b>	<b>149</b>
<b>Curriculum Vitae .....</b>	<b>151</b>
Professional Experience.....	151
Education .....	151
Languages .....	151
<b>List of Publications .....</b>	<b>153</b>
Journal Papers.....	153
Conferences .....	154

## Summary

An effective way for the automotive industry to tackle the growing concern of increasing CO<sub>2</sub> emissions is to reduce the vehicle's overall weight, without compromising its performance and passenger safety. With the increasing demand for steels with enhanced properties in the last decades, the development of advanced high-strength steels (AHSSs) has been focused on the design of complex microstructures, leading to exceptional combinations of strength and ductility. On the other hand, stainless steels also offer significant potential in automotive lightweight applications to complement carbon steel AHSS grades. Stainless steels can offer additional advantages, including better corrosion resistance (no need for galvanising) and increased strength and fatigue resistance. However, a significant barrier to their application is the alloying cost (nickel in austenitic stainless steels) or low ductility and formability (standard martensitic stainless steels).

A solution to this problem is to develop a new class of martensitic stainless steels by combining tailored chemistries and novel heat treatments, e.g., quenching and partitioning (Q&P). In Q&P processing, retained austenite is included in the (tempered) martensite microstructure, leading to the transformation-induced plasticity (TRIP) effect, enhancing ductility. Thus, low-cost, high-strength and ductile stainless steel can be developed for automotive applications. Finally, an essential benefit of using martensitic stainless steel type chemistries (including 13 wt% Cr) is that Q&P heat treatments can be significantly simplified. The optimum hardenability of these stainless steels allows austenite to remain retained at room temperature even at low cooling rates. This greatly simplifies heat treatment and facilitates industrial implementation. Besides the development of these microstructural processes, it is essential for the application of these steels that their stainless characteristics are maintained or further improved. Therefore, the research also aims at better understanding of corrosion processes in these steels.

Keeping this in mind, martensitic stainless steels varying in C, Mn, and Ti/Nb contents have been designed, with the room temperature quenching capability being an extra characteristic. Experimental and modelling approaches are employed in this Ph.D. thesis to investigate the microstructural evolution, microstructure–corrosion relationship, and the mechanisms involved during the Q&P process in the newly designed martensitic stainless steels.

This thesis begins with Chapter 1, which presents a brief history of steel development and includes a critical review that elucidates the way in which the work presented in this Ph.D. thesis fits within the broader context of steel research and development. Chapter 2 illustrates the design and scale-up selection of chemical compositions and the optimisation of heat treatment parameters for the investigated Q&P steels through theoretical calculations and experimental characterisation. Typical Q&P heat treatments with partitioning temperatures of 400 °C and 450 °C are applied. The

applicability of Q&P heat treatment on martensitic stainless steels is evaluated. Chapter 3 gives insight into the microstructural heterogeneity evolution and competitive reactions occurring in two steels with different Mn content during the application of the Q&P process. Theoretical calculations suggest that competing phenomena, such as carbide precipitation during the initial quench or the isothermal partitioning stage, deplete the carbon that would otherwise be available for partitioning into the austenite. This has a negative influence on the austenite stability and the Q&P microstructural development, as they reduce the volume fraction of retained austenite. The last part of this chapter proposes an approach aimed at determining the carbon concentration in austenite after partitioning, using the formation-start temperature of fresh martensite. This method addresses limitations observed in lattice parameter calculation formulas relying on X-ray diffraction measurements. In Chapter 4, based on the observations from Chapter 3, special attention is paid to the evolution of the microstructure heterogeneity into a more homogeneous distribution of phases after first quenching to room temperature and partitioning at 400 °C. A stage-to-stage characterisation reveals the elimination of microstructural banding during partitioning, especially in steel with high Mn content. The partitioning model considers interface movement and explains the evolution mechanisms influenced by local and global equilibrium.

Chapter 5 explores the corrosion resistance of industrial Q&P processed steels. The outcome of this chapter shows that, irrespective of the chemical composition and phase fraction, the inclusions in industrial production (MnS) and the precipitating microalloying particles (TiN) predominantly govern the localised corrosion initiation. Considering lab-processed Q&P steels with low density of MnS inclusions, Chapter 6 explores the impact of microalloying elements Ti and Nb on the corrosion behaviour of lab-processed Q&P steels. Results from microstructural and electrochemical characterisations revealed that the presence of TiN-Nb particles, in combination with Cr-carbides at prior austenite grain boundaries, intensifies the susceptibility of the steel to intergranular corrosion attack.

The last chapter of the thesis, Chapter 7, summarises the research findings and presents suggestions for further research.

The outcomes of this Ph.D. research result in the development of a new generation of competitive martensitic stainless steels for the automotive sector with unique benefits in corrosion resistance. The fundamental knowledge gained from this research about the mechanisms controlling microstructure development and the corrosion-microstructure relationship fills a critical knowledge gap and opens up the possibility of further exploiting the applicability of the Q&P process to enhance the properties of martensitic stainless steels.

## Samenvatting

Een effectieve manier voor de automobieliindustrie om de toenemende zorg over stijgende CO<sub>2</sub>-uitstoot aan te pakken, is het verlagen van het totale voertuiggewicht zonder afbreuk te doen aan de prestaties en passagiersveiligheid. Met de toenemende vraag naar staal met verbeterde eigenschappen in de afgelopen decennia, heeft de ontwikkeling van geavanceerde hoogsterkte-staalsoorten (AHSS) zich gericht op het ontwerpen van complexe microstructuren, hetgeen leidt tot uitzonderlijke combinaties van sterkte en vervormbaarheid. Aan de andere kant bieden roestvaste staalsoorten ook een aanzienlijk potentieel voor lichtgewicht toepassingen in de auto-industrie, complementair aan op koolstof gebaseerde AHSS-soorten. Roestvast staal biedt bijkomende voordelen, waaronder betere corrosiebestendigheid (geen noodzaak voor galvanisatie) en verhoogde sterkte en vermoeiingsbestendigheid. Een belangrijke hindernis voor hun toepassing zijn echter de legeringskosten (zoals voor nikkel in austenitisch roestvast staal) of de lage vervormbaarheid en verwerkbaarheid (standaard martensitisch roestvast staal).

Een oplossing voor dit probleem is de ontwikkeling van een nieuwe klasse martensitisch roestvast staal door het combineren van specifieke chemische samenstellingen en nieuwe warmtebehandelingsmethoden, zoals *quenching and partitioning* (Q&P). In het Q&P-proces is rest-austeniet opgenomen in de (ontlaten) martensiet-microstructuur, hetgeen leidt tot het transformatiegeïnduceerde plasticiteitseffect (TRIP) en zo de vervormbaarheid verhoogt. Zo kan relatief goedkoop, sterk en taai roestvast staal worden ontwikkeld voor automobieltoepassingen. Een belangrijk voordeel van het gebruik van martensitische roestvast staalsoorten (met 13 gew% Cr) is dat Q&P-warmtebehandelingen sterk vereenvoudigd kunnen worden. Door de optimale hardbaarheid van deze roestvast staalsoorten blijft austeniet behouden bij kamertemperatuur, zelfs bij lage afkoelsnelheden. Dit vereenvoudigt het warmtebehandelingsproces en vergemakkelijkt de industriële implementatie. Naast de ontwikkeling van deze microstructurele processen is het voor de toepassing van deze staalsoorten essentieel dat de roestvastheidseigenschappen behouden blijven of verder verbeterd worden. Daarom is het onderzoek ook gericht op een beter begrip van corrosieprocessen in deze staalsoorten.

Met dit in gedachten zijn martensitische roestvast staalsoorten ontworpen met variërende C-, Mn- en Ti/Nb-gehalten, waarbij de mogelijkheid om austeniet te behouden tijdens afschrikken naar kamertemperatuur een extra eigenschap is. Experimentele en modelmatige benaderingen worden in dit proefschrift gebruikt om de microstructurele evolutie, de relatie tussen microstructuur en corrosie en de mechanismen tijdens het Q&P-proces in de nieuw ontworpen martensitische roestvast staalsoorten te onderzoeken.

Dit proefschrift begint met Hoofdstuk 1, waarin een korte geschiedenis van de staalontwikkeling wordt gepresenteerd en een kritische bespreking wordt gegeven die toelicht hoe het werk in dit proefschrift past binnen de bredere context van staalonderzoek en -ontwikkeling. Hoofdstuk 2 illustreert de selectie en opschaling van chemische samenstellingen en de optimalisatie van warmtebehandelingsparameters voor de onderzochte Q&P-staalsoorten door middel van theoretische berekeningen en experimentele karakterisering. Typische Q&P-warmtebehandelingen met *partitioning* op 400 °C en 450 °C worden toegepast. De toepasbaarheid van Q&P-warmtebehandeling op martensitische roestvast staalsoorten wordt geëvalueerd. Hoofdstuk 3 geeft inzicht in de microstructurele heterogeniteit en concurrerende reacties die optreden in twee staalsoorten met verschillend Mn-gehalte tijdens de toepassing van het Q&P-proces. Theoretische berekeningen suggereren dat concurrerende fenomenen, zoals carbidenprecipitatie tijdens de initiële *quench* en de isotherme *partitioning step*, het koolstofgehalte verminderen dat anders beschikbaar zou zijn voor partitie in de austeniet. Dit heeft een negatieve invloed op de stabiliteit van austeniet en de Q&P-microstructuurontwikkeling, doordat ze de hoeveelheid koolstof die beschikbaar is voor partitie verminderen en dus de volumefractie van rest-austeniet verlagen. Het laatste deel van dit hoofdstuk stelt een benadering voor om de koolstofconcentratie in austeniet na partitie te bepalen, met behulp van de temperatuur waarbij nieuwe martensietvorming begint. Deze methode voorkomt beperkingen die worden waargenomen bij formules voor roosterparameterberekeningen gebaseerd op röntgendiffractie-metingen.

In Hoofdstuk 4 wordt, gebaseerd op de waarnemingen uit Hoofdstuk 3, speciale aandacht besteed aan de evolutie van de microstructurele heterogeniteit naar een meer homogene faseverdeling na een eerste *quench* tot kamertemperatuur en *partitioning* bij 400 °C. Een stapsgewijze karakterisering toont de eliminatie van microstructurele bandvorming tijdens *partitioning*, vooral in staal met een hoog Mn-gehalte. Het partitiemodel houdt rekening met grensvlakbeweging en verklaart de evolutiemechanismen die worden beïnvloed door lokaal en globaal evenwicht.

Hoofdstuk 5 onderzoekt de corrosiebestendigheid van industrieel Q&P-verwerkte staalsoorten. De uitkomst van dit hoofdstuk toont dat, ongeacht de chemische samenstelling en fasefracties, de insluitsels in industriële productie (MnS) en de microlegerings-deeltjes (TiN) in hoge mate de lokale corrosie-initiatie beïnvloeden. Q&P-staalsoorten bestuderend die in het laboratorium zijn verwerkt met een lage dichtheid aan MnS-insluitsels, onderzoekt Hoofdstuk 6 de invloed van microlegeringselementen Ti en Nb op het corrosiegedrag van deze Q&P-staalsoorten. Resultaten van microstructurele en elektrochemische karakterisering tonen dat de aanwezigheid van TiN-Nb-deeltjes, samen met Cr-carbiden bij vooraf bestaande austenietkorrelgrenzen, de gevoeligheid van het staal voor interkristallijne corrosie versterkt.

Het laatste hoofdstuk van het proefschrift, Hoofdstuk 7, vat de onderzoeksbevindingen samen en presenteert suggesties voor verder onderzoek.

De uitkomsten van dit promotieonderzoek resulteren in de ontwikkeling van een nieuwe generatie concurrerende martensitische roestvast staalsoorten voor de automobielsector met unieke voordelen in corrosiebestendigheid. De fundamentele kennis die is opgedaan over de mechanismen die de microstructuurontwikkeling en de relatie tussen corrosie en microstructuur beheersen, vult een kritieke kenniskloof op en opent de mogelijkheid om de toepasbaarheid van het Q&P-proces verder te benutten om de eigenschappen van martensitisch roestvast staal te verbeteren.



# 1

## Introduction



## 1.1 State of the Art

Advanced high strength steels (AHSSs) for automotive applications have been and remain a major driver in the development of new steels due to their large share in the steel market and the high pressure on the improvement of their performance over weight and price ratio. Over the past few decades, there have been major developments in their composition, hot- and cold-rolling processes, microstructure and properties. These advancements have led to the evolution of three generations of AHSSs, categorised based on their tensile strength and percentage elongation (ductility), as depicted in **Figure 1.1**, known as the global formability diagram or “banana diagram” [1].

The conventional generations of steels include high-strength low-alloy (HSLA) and bake-hardenable (BH) steels, which typically have an ultimate tensile strength of less than 600 MPa. The 1<sup>st</sup> generation AHSSs exhibit higher work-hardening rates and improved formability due to a ferrite matrix for ductility and a harder second phase for strength. Examples include dual-phase (DP) and transformation-induced plasticity (TRIP) grades [2]. The 2<sup>nd</sup> generation AHSSs demonstrate significantly higher ductility than the 1<sup>st</sup> generation AHSS grades, attributed to stabilised austenite in the final microstructure [3]. However, the addition of austenite-stabilising elements increases alloying costs, which has limited their widespread usage.

Since the beginning of the 2000s, efforts have been focused on producing steels with lower concentrations of alloying elements yet with an excellent combination of properties. These steels are known as the 3<sup>rd</sup> generation AHSSs [4].

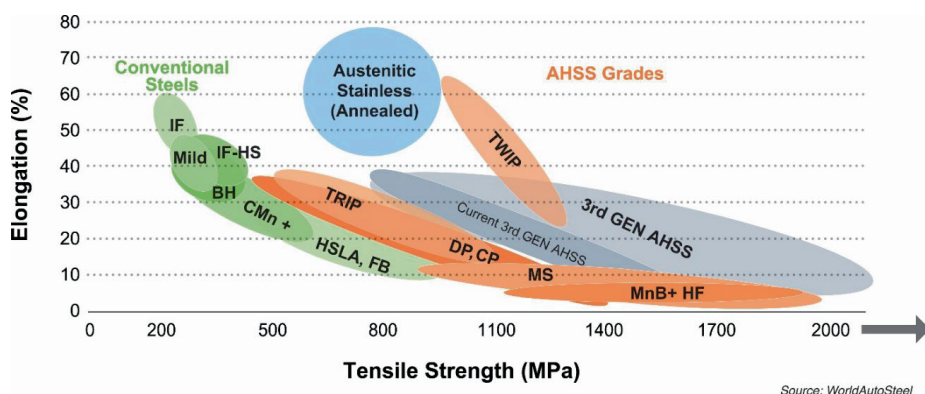


**Figure 1.1. Global formability diagram 2021 [1].**

In recent decades, quenching and partitioning (Q&P) steels, proposed by Speer et al. [5-7], as typical 3<sup>rd</sup> generation AHSSs, have attracted significant attention due to their excellent balance of strength and ductility. The Q&P process involves a heat treatment comprising mainly four steps, as

depicted in **Figure 1.2**: (1) the austenitisation step, during which the steel is fully or partially austenitised, and the characteristics of the parent austenite like grain size, composition homogeneity, and morphology are controlled via appropriate heat treatment parameters; (2) the quenching step, during which the austenitised microstructure is quenched to a temperature between the martensite start ( $M_s$ ) temperature and the martensite finish ( $M_f$ ) temperature, aiming to obtain a controlled combination of austenite and martensite in the microstructure; (3) the partitioning step, in which the material is kept at a constant temperature (same or higher than the quenching temperature) to promote the redistribution of carbon from martensite to austenite [8-10]; and (4) the final quenching step, during which the partitioned microstructure is cooled down to room temperature while the formation of fresh martensite is normally avoided [9-11]. The resulting microstructure is formed by carbon-depleted martensite and carbon-enriched retained austenite.

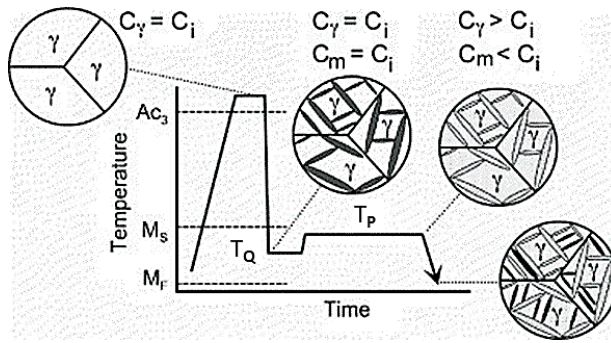


**Figure 1.2.** Concept of Q&P heat treatment of steels showing schematic of microstructure evolution [5,6].  $C_i$ ,  $C_\gamma$ , and  $C_m$  represent the carbon content in the original alloy, austenite, and martensite, respectively.  $T_Q$  and  $T_P$  correspond to the initial quenching temperature and partitioning temperature, respectively.

The carbon partitioning process from martensite to austenite plays a crucial role in stabilising austenite. The thermodynamics involved in this process were initially described by the constrained carbon equilibrium (CCE) model [5], as shown in **Figure 1.3**. The CCE model considers three main conditions for carbon partitioning: (1) carbon partitioning continues until the chemical potential of carbon in both martensite and austenite is equal; (2) the interface between martensite and austenite remains stationary during the carbon partitioning process; (3) no competing reactions, such as carbide precipitation or austenite decomposition, occur during the carbon partitioning process. The CCE model can also be used to predict the quenching temperature that results in a maximum volume fraction of retained austenite [12].

In practice, the CCE model is not fully applicable during actual Q&P processing because carbide precipitation and other competitive reactions may occur during the partitioning step [13-15]. These

competing reactions consume carbon that is otherwise available for partitioning into the austenite phase. Consequently, adaptations of the CCE model have been proposed to incorporate the influence of these competing processes [16-20].

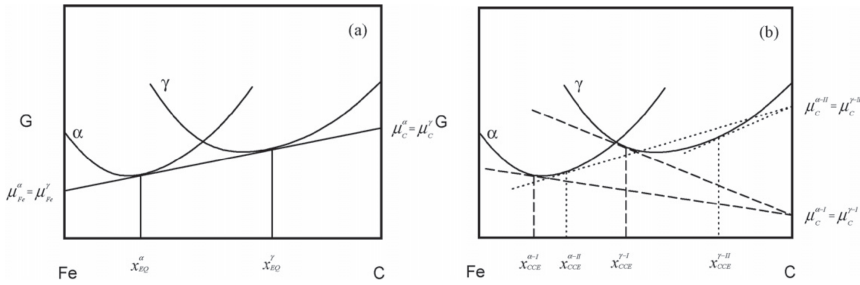


**Figure 1.3. Schematic molar Gibbs energy vs. composition diagrams illustrating metastable equilibrium at a particular temperature between ferrite and austenite in the Fe–C binary system: (a) equilibrium and (b) two possible constrained carbon equilibrium conditions (I and II) showing two possible ferrite and austenite compositions satisfying the CCE requirement that the chemical potential of carbon is equal in the two phases [5].**

Extensive scientific reports on the Q&P treatment applied to carbon steels [13-20] have shown a superior combination of strength and toughness due to the presence of martensite and retained austenite. Limited investigations refer to the application of the Q&P process to martensitic stainless steels. Mola et al. [21] systematically studied this process in martensitic stainless steels (Fe-0.31C-13.18Cr, in wt.%), providing a comprehensive analysis of the thermal and mechanical stability of austenite. The study found that austenite stabilisation is not solely due to the uniform carbon enrichment, but also the local carbon enrichment, which locks potential martensite nucleation sites within the austenite and at austenite/martensite boundaries. This stabilisation mechanism becomes increasingly important at lower quench temperatures, corresponding to higher primary martensite fractions.

Reverted austenite has been observed in Q&P treated martensitic stainless steels. The influence of quench temperature and partitioning time on the microstructure evolution was studied in a Q&P processed 0.45C-0.65Mn-13.95Cr (wt.%) martensitic stainless steel [22]. Reverted austenite was found during partitioning at 400°C with increasing partitioning times. This phenomenon is driven by local carbon enrichment at martensite/martensite and martensite/austenite interfaces, leading to the local reversion of martensite to austenite.

In another study [23], the nanoscale mechanism of austenite reversion has been referred to as the kinetic freezing of carbon. Carbon redistribution occurs in three main ways: a) During quenching, carbon segregates from the supersaturated martensite to both martensite/austenite and

martensite/martensite interfaces. b) During partitioning (referred to as tempering in [23]), carbon further partitions to martensite/austenite interfaces, driving the carbon-enriched areas towards austenite reversion. c) Carbon inside martensite, far away from any interfaces, tends to form carbides. This indicates that carbon becomes trapped and enriches the martensite-austenite interfaces due to its low mobility within austenite during low-temperature partitioning. This results in a significantly high local driving force for austenite reversion. Therefore, the formation of nanoscale reverted austenite depends primarily on the local chemical potential of carbon at internal interfaces rather than the global chemical potential. The proposed austenite reversion mechanism is illustrated schematically by **Figure 1.4** below.

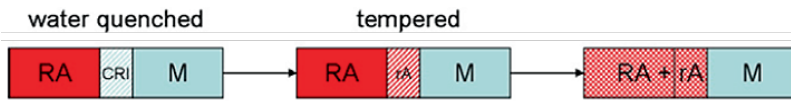


**Figure 1.4. Austenite reversion mechanism for 0.44C-13.6Cr steel following room temperature quenching and partitioning, adapted from [23]. M=martensite, RA=retained austenite, rA=reverted austenite, CRI=carbon rich interface.**

Another investigation [24] compared low-carbon martensitic stainless steels with varying silicon content. By calculating the optimal quenching temperature and selecting appropriate partitioning conditions, constrained carbon equilibrium conditions were achieved, resulting in almost all the carbon redistributing into the untransformed austenite during the partitioning process. The study demonstrated that silicon may not be essential in Q&P processed 12Cr steels [25-27].

The application of the CCE model to describe the carbon partitioning process in stainless steels has encountered difficulties due to competing reactions [21,23,24,28,29]. Carbide precipitation reduces the carbon content of retained austenite, thereby affecting its stability [21,24,28,29]. Additionally, austenite reversion [23] and the migration of martensite/austenite interfaces [29] influence the fraction of phase constituents. Nevertheless, nearly ideal CCE conditions were achieved by adding specific elements to the compositions [27]. This suggests that the applicability of the CCE model depends on the presence of specific elements that can inhibit competing reactions [30,31]. Overall, the process of carbon partitioning in stainless steels is influenced by complex mechanisms such as carbide precipitation, austenite reversion, and interface migration, which require further investigation.

Currently, research on Q&P processed steels primarily focuses on the correlation between microstructure and mechanical properties. Studies on the corrosion performance of Q&P processed steels are very limited. Both carbon steels [32,33] and stainless steels [34,35] treated with the Q&P

process exhibit improved corrosion resistance compared to traditionally quenched and tempered (Q&T) processed steels.

In Q&T treated steels, retained austenite is absent or present in very low fractions (typically less than 0.01). Therefore, carbon is dissolved in the martensite [32,33]. In Q&P treated steels, the C-depleted martensite is electrochemically more active than the C-rich retained austenite. The total cathodic area (C-rich retained austenite) in the Q&P steels is smaller than in the Q&T steels (C-rich martensite). Thus, the corrosion rate for Q&P steels is lower than for Q&T steels [29]. Moreover, the long tempering treatments applied to Q&T-processed steels (of the order of hours) allow Cr-carbides precipitation, leading to Cr-depletion at the carbide/matrix interfaces, which are susceptible to pitting corrosion. In the case of Q&P steels, the isothermal treatments applied are shorter (typically minutes), reducing, but not eliminating, the chances of Cr-carbide precipitation. Consequently, the Q&P processed steels might present better pitting corrosion resistance than the conventional Q&T steels [29,34,35]. These findings highlight the potential benefits of Q&P treatments in improving the corrosion resistance of steels.

Nevertheless, the occurrence of competing reactions, particularly carbide precipitation, and its potential role in initiating localised corrosion remains uncertain in Q&P steels. Q&P steels are multiphase materials where the presence of C-enriched austenite and C-depleted martensite are expected to exert additional influence. Bridging these gaps and comprehending the complex microstructural development during the application of Q&P treatment to stainless steels and unravelling the relationship between microstructural characteristics and corrosion properties is crucial to providing fundamental knowledge for the development of 3<sup>rd</sup> generation AHSSs.

## 1.2 Research Objectives

The primary research objective of this PhD thesis is to comprehensively investigate the evolution of microstructure and the underlying mechanisms involved during the Q&P process of martensitic stainless steels. This investigation will be conducted through a combination of experimental techniques and modelling approaches.

Furthermore, this thesis aims to understand the impact of heat treatment parameters, phase fractions, and chemical composition on the microstructure development and its subsequent influence on the corrosion properties of martensitic stainless steels produced via the Q&P process.

Microstructures are investigated by means of ex-situ and in-situ advanced characterisation techniques, such as dilatometry, electron back-scatter diffraction (EBSD), vibrating sample magnetometer (VSM), and X-ray diffraction (XRD), to determine the nature and morphology of all formed phases. Kinetics and thermodynamic analyses are carried out to investigate the applicability

of CCE model and to understand the microstructure development. The relationships between microstructure and corrosion are explored with scanning Kelvin probe force microscopy (SKPFM), scanning electrochemical microscopy (SECM), potentiodynamic polarisation (PDP), double loop electrochemical potentiokinetic reactivation (DL-EPR), X-ray photoelectron spectroscopy (XPS), and transmission electron microscopy (TEM), aiming to qualitatively and quantitatively determine the effect of chemical composition and phase fraction on the corrosion behaviour of the Q&P microstructures.

### 1.3 Outline

This PhD thesis contains one introduction chapter (Chapter 1), five main research chapters (Chapter 2 – 6) based on scientific papers that are or will be published in scientific journals, and one final chapter of general conclusions and recommendations for future work (Chapter 7). Chapter 2 presents the design, characterisation and optimisation of Q&P heat treatment parameters and chemical compositions of investigated materials. Chapters 3 and 4 present a deep analysis of the microstructure evolution during the Q&P process, combining both experimental and simulations approached. Chapters 5 and 6 present a detailed study of the corrosion performance of Q&P steels, and on their microstructure – corrosion property relationships.

The outline is summarised below:

**Chapter 2** illustrates the design of chemical compositions and optimisation of heat treatment parameters for the investigated Q&P treated steels. Initially, ten chemistries are designed based on Thermo-Calc predictions, which are then narrowed down to six chemistries through microstructure characterisation. Subsequently, three chemistries are selected for application-oriented performance characterisation. Q&P treatment parameters are optimised using kinetic simulations and literature research, followed by experimental characterisation and validation.

**Chapter 3** presents an investigation of the microstructure development during the application of the Q&P process to two stainless steels with different Mn content. The results are compared with calculations based on the constrained carbon equilibrium theory, paying special attention to the presence of reactions competing for the carbon available for partitioning and the effect of alloying element segregation. The insight gained from this study provides an understanding of the interplay between carbon partitioning, carbide formation, chemical segregation and phase transformation kinetics during Q&P processing.

**Chapter 4** investigates interface migration and partitioning kinetics in two martensitic stainless steels with different Mn content by combining cellular automation simulation and morphological characterisation via electron back scatter diffraction before and after partitioning. The influence of

topology, carbon partitioning and migration of austenite/martensite interfaces is discussed. The outcome of this chapter shows that during the partitioning stage, apart from the concentration gradient – driven carbon diffusion and interface partitioning, the interface migration must be taken into account.

**Chapter 5** investigates the role of inclusions on localised corrosion initiation in three fully-processed Q&P martensitic stainless steels through a combined ex-situ and in-situ probe microscopy study. The influence of chemical composition, heat treatment parameters and microstructure on corrosion performance is investigated using microstructural and electrochemical characterisation techniques. The localised corrosion initiation is investigated mainly by using the scanning Kelvin probe force and the electrochemical scanning microscopy. Microstructure homogeneity and interaction between matrix and inclusions are highlighted as the main factors for pitting initiation in Q&P microstructures.

**Chapter 6** explores the effects of microstructure (phase fraction) and micro-alloying elements (NbTi) on intergranular corrosion performance. Intergranular corrosion (IGC) of NbTi-free and NbTi-microalloyed Q&P produced martensitic stainless steels is investigated by the combined use of electrochemical test (DL-EPR) and microstructural analysis (TEM and SKPFM). Differences in the degree of sensitisation to IGC are discussed in terms of carbide formation, particle precipitation (Chapter 5), and nature of the phases formed after carbon partitioning.

The final **Chapter 7** concludes the thesis and gives recommendations for possible future work.

## Reference

- [1] <https://www.worldautosteel.org/steel-basics/automotive-advanced-high-strength-steel-ahss-definitions/>
- [2] W. Wang, M. Li, C.W. He, X.C. Wei, D.Z. Wang, H.B. Du, Experimental study on high strain rate behavior of high strength 600–1000 MPa dual phase steels and 1200 MPa fully martensitic steels. *Materials and Design*, 47(2013) 510–521. <https://doi.org/10.1016/j.matdes.2012.12.068>
- [3] M.R. Fekhreiddine, M. Tisza, Third generation of advanced high strength sheet steels for the automotive sector : A literature review. *Multidiszciplináris Tudományok*, 11(2021) 24 – 247. <http://dx.doi.org/10.35925/j.multi.2021.4.28>
- [4] A. Grajcar, R. Kuziak, W. Zalecki, Third generation of AHSS with increased fraction of retained austenite for the automotive industry. *Archives of Civil and Mechanical Engineering*, 12(2012) 334 – 341. <https://doi.org/10.1016/j.acme.2012.06.011>
- [5] J. Speer, D.K. Matlock, B.C. De Cooman, J.G. Schroth, Carbon partitioning into austenite after martensite transformation. *Acta Materialia*, 51(2003) 2611 – 2622. [https://doi.org/10.1016/S1359-6454\(03\)00059-4](https://doi.org/10.1016/S1359-6454(03)00059-4)
- [6] D.V. Edmonds, K. He, F.C. Rizzo, B.C. De Cooman, D.K. Matlock, J.G. Speer, Quenching and partitioning martensite—A novel steel heat treatment. *Materials Science and Engineering: A*, 25-34 (2006) 438–440. <https://doi.org/10.1016/j.msea.2006.02.133>
- [7] A. J. Clarke, J.G. Speer, M.K. Miller, R.E. Hackenberg, D.V. Edmonds, D.K. Matlock, F.C. Rizzo, K.D. Clarke, E. De Moor, Carbon partitioning to austenite from martensite or bainite during the quench and partition (Q&P) process: a critical assessment. *Acta Materialia*, 56 (2008) 16 – 22. <https://doi.org/10.1016/j.actamat.2007.08.051>
- [8] S. Ayenampudi, C. Celada-Casero, J. Sietsma, M.J. Santofimia, Microstructure evolution during high-temperature partitioning of a medium-Mn quenching and partitioning steel. *Materialia*, 8 (2019) 100492. <https://doi.org/10.1016/j.mtla.2019.100492>
- [9] A.S. Nishikawa, M.J. Santofimia, J. Sietsma, H. Goldensteina, Influence of bainite reaction on the kinetics of carbon redistribution during the Quenching and Partitioning process. *Acta Materialia*, 142 (2018) 142–151. <https://doi.org/10.1016/j.actamat.2017.09.048>
- [10] A.S. Nishikawa, G. Miyamoto, T. Furuhashi, A.P. Tschietschin, H. Goldenstein, Phase transformation mechanisms during Quenching and Partitioning of a ductile cast iron. *Acta Materialia*, 159 (2019) 1–16. <http://dx.doi.org/10.1016/j.actamat.2019.08.001>
- [11] D. De Knijf, R. Petrov, C. Föjer, L.A.I. Kestens, Effect of fresh martensite on the stability of retained austenite in quenching and partitioning steel. *Materials Science and Engineering: A*, 615 (2014) 107–115. <https://doi.org/10.1016/j.msea.2014.07.054>

- [12] D.P. Koistinen, R.E. Marburger, A general equation prescribing the extent of the austenite-martensite transformation in pure iron-carbon alloys and plain carbon steels. *Acta Metallurgica*, 7 (1959) 59–60. [https://doi.org/10.1016/0001-6160\(59\)90170-1](https://doi.org/10.1016/0001-6160(59)90170-1)
- [13] S. Kumar, S. BratSingh, Evolution of microstructure during the "quenching and partitioning (Q&P)" treatment. *Materialia*, 18 (2021) 101135. <https://doi.org/10.1016/j.mtla.2021.101135>
- [14] J.Z. Zhang, Z.B. Dai, L.Y. Zeng, X. Zuo, J.F. Wan, Y.H. Rong, N.L. Chen, J. Lu, H. Chen, Revealing carbide precipitation effects and their mechanisms during quenching-partitioning-tempering of a high carbon steel: Experiments and Modeling. *Acta Materialia*, 217 (2021) 117176. <https://doi.org/10.1016/j.actamat.2021.117176>
- [15] S. Ebner, C. Suppan, A. Stark, R. Schnitzer, C. Hofer, Austenite decomposition and carbon partitioning during quenching and partitioning heat treatments studied via in-situ X-ray diffraction. *Materials & Design*, 178 (2019) 107862. <https://doi.org/10.1016/j.matdes.2019.107862>
- [16] P.F. Gao, J.H. Liang, W.J. Chen, F. Li, Z.Z. Zhao, Prediction and evaluation of optimum quenching temperature and microstructure in a 1300 MPa ultra-high-strength Q&P steel. *Journal of Iron and Steel Research International*, 29 (2022) 307–315. <https://doi.org/10.1007/s42243-020-00535-5>
- [17] J.Y. Li, Y.B. Xu, B. Lu, Y.M. Yu, Y. Jing, W.H. Sun, Improvement of strength-ductility combination in ultra-high-strength medium-Mn Q&P steel by tailoring the characteristics of martensite/retained austenite constituents. *Journal of Materials Research and Technology*, 18 (2022) 352–369. <https://doi.org/10.1016/j.jmrt.2022.02.088>
- [18] F.M. Castro Cerda, E.I. Hernández, T. Ros-Yanez, R.H. Petrov, Isothermal Phase Transformations in a Low Carbon Steel During Single and Two-Step Partitioning. *Metallurgical and Materials Transactions A*, 51 (2020) 1506–1518. <https://doi.org/10.1007/s11661-020-05643-1>
- [19] Y. Li, S. Chen, C.C. Wang, D.S. Martín, W. Xu, Modelling retained austenite in Q&P steels accounting for the bainitic transformation and correction of its mismatch on optimal conditions. *Acta Materialia*, 188 (2020) 528–538. <https://doi.org/10.1016/j.actamat.2020.02.033>
- [20] Z.B. Dai, R. Ding, Z.G. Yang, C. Zhang, H. Chen, Elucidating the effect of Mn partitioning on interface migration and carbon partitioning during Quenching and Partitioning of the Fe-C-Mn-Si steels: Modeling and experiment. *Acta Materialia*, 144 (2018) 666–678. <https://doi.org/10.1016/j.actamat.2017.11.025>
- [21] J. Mola, B.C. De Cooman. Quenching and partitioning processing of martensitic stainless steels. *Metallurgical and Materials Transactions A*, 44 (2013) 946–966. doi: 10.1007/s11661-012-1420-

- [22] S. Dieck, P. Rosemann, A. Kromm, T. Halle, Reversed austenite for enhancing ductility of martensitic stainless steel. *IOP Conf. Series: Materials Science and Engineering* 181(2017) 012034. doi:10.1088/1757-899X/181/1/012034
- [23] L. Yuan, D. Ponge, J. Wittig, P. Choi, J.A. Jiménez, D. Raabe, Nanoscale austenite reversion through partitioning, segregation and kinetic freezing: Example of a ductile 2 GPa Fe–Cr–C steel. *Acta Materialia*, 60 (2012) 2790–2804. <https://doi.org/10.1016/j.actamat.2012.01.045>
- [24] T. Tsuchiyama, J. Tobata, T. Tao, N. Nakada, S. Takaki, Quenching and partitioning treatment of a low-carbon martensitic stainless steel. *Materials Science and Engineering: A*, 532 (2012) 585–592. <https://doi.org/10.1016/j.msea.2011.10.125>
- [25] S. Björklund, L.F. Donaghey, M. Hillert, Influence of the elements of the alloy on the oswald maturation rate of the cementite in steel. *Acta Metallurgica*. 20(1972) 867–874. [https://doi.org/10.1016/0001-6160\(72\)90079-X](https://doi.org/10.1016/0001-6160(72)90079-X)
- [26] T. Suzuki, Y. Ono, G. Miyamoto, T. Furuhashi, Effects of Si and Cr on bainite microstructure of medium carbon steels. *ISIJ International*, 50(2010) 1467–1482. <https://doi.org/10.2355/isijinternational.50.1476>
- [27] J. Tobata, K.L. Ngo-Huynh, N. Nakada, T. Tsuchiyama, S. Takaki, Role of silicon in quenching and partitioning treatment of low-carbon martensitic stainless steel. *ISIJ International*, 52 (2012) 1377–1382. <http://dx.doi.org/10.2355/isijinternational.52.1377>
- [28] Q.L. Huang, C. Schröder, H. Biermann, O. Volkova, J. Mola, Influence of martensite fraction on tensile properties of quenched and partitioned (Q&P) martensitic stainless steels. *Steel Research International*, 87 (2016) 1082–1094. <https://doi.org/10.1002/srin.201500472>
- [29] S.Y. Lu, K.F. Yao, Y.B. Chen, M.H. Wang, N. Chen, X.Y. Ge, Effect of quenching and partitioning on the microstructure evolution and electrochemical properties of a martensitic stainless steel. *Corrosion Science*, 103 (2016) 95–104. <https://doi.org/10.1016/j.corsci.2015.11.010>
- [30] Z.B. Dai, H. Chen, R. Ding, Q. Lu, C. Zhang, Z.G. Yang, S. van der Zwaag, Fundamentals and application of solid-state phase transformations for advanced high strength steels containing metastable retained austenite. *Materials Science and Engineering: R: Reports*, 143 (2021) 100590. <https://doi.org/10.1016/j.mser.2020.100590>
- [31] B. Kim, J. Sietsma, M.J. Santofimia, The role of silicon in carbon partitioning processes in martensite/austenite microstructures. *Materials & Design*, 127 (2017) 336–345. <https://doi.org/10.1016/j.matdes.2017.04.080>
- [32] J.L. Yang, Y.F. Lu, Z.H. Guo, J.F. Gu, C.X. Gu, Corrosion behaviour of a quenched and partitioned medium carbon steel in 3.5wt.% NaCl solution. *Corrosion Science*, 130(2018) 64 – 75. <https://doi.org/10.1016/j.corsci.2017.10.027>

- [33] T. Mehner, R. Morgenstern, P. Frint, I. Scharf, M. F-X Wagner, T. Lampke, Corrosion characteristics of a quenching and partitioning steel determined by electrochemical impedance spectroscopy. IOP Conference Series: Materials Science and Engineering, 373(2018) 012003. <https://doi.org/10.1088/1757-899X/373/1/012003>
- [34] G. Luo, H.Y. Li, Y.G. Li, J.Q. Mo, Microstructures and properties of a low-carbon-chromium ferritic stainless steel treated by a quenching and partitioning process. Materials, 12 (2019) 1704. <https://doi.org/10.3390/ma12101704>
- [35] S.K. Bonagani, V. Bathula, V. Kain, Influence of tempering treatment on microstructure and pitting corrosion of 13 wt.% Cr martensitic stainless steel. Corrosion Science, 131(2018) 340 – 354. <https://doi.org/10.1016/j.corsci.2017.12.012>



# 2

2

## Heat Treatment and Chemical Composition



## 2.1 Introduction

This chapter covers the fundamental aspects of alloy composition design, the selection process of Quenching and Partitioning (Q&P) heat treatment parameters, and the microstructure characterisation of the developed alloys.

## 2.2 Materials and Experimental Methods

### 2.2.1 Materials

**Table 2.1** shows the chemical composition of the newly-designed martensitic stainless steels used in this thesis. The chemical composition of steel ACX390, provided by the industrial partner ACERINOX, is also presented, as it is used to study optimal austenitisation conditions.

In this chapter, the alloys are listed according to their order of generation. In subsequent chapters of this thesis, the alloys will be referred to based on their specific C and Mn content, where 0.7% Mn is considered low (LMn) and 3.0% Mn is considered high (HMn). The designations are as follows: alloy 1C, alloy 2C LMn, alloy 2C HMn, alloy 3C LMn, alloy 3C HMn, and alloy 3C HMn-NbTi. Please note that in the following chapters, for the specific samples investigated in each case, material heterogeneity may lead to composition variations, with  $\pm 0.02$  wt.% for C and  $\pm 0.1$  wt.% for Mn relative to the designed composition.

**Table 2.1. The chemical composition of the steels investigated, in wt.%.**

Alloy	C	Mn	Si	Cr	Ni	Al	N	Nb	Ti
1C	0.13	0.7	0.35	12.0	0.20	0.01	0.03		
2C LMn	0.20	0.7	0.35	12.5	0.20	0.01	0.03		
2C HMn	0.20	3.0	0.35	12.5	0.20	0.01	0.03		
3C LMn	0.30	0.7	0.35	13.0	0.20	0.01	0.03		
3C HMn	0.30	3.0	0.35	13.0	0.20	0.01	0.03		
3C HMn-NbTi	0.30	3.0	0.35	13.0	0.20	0.01	0.03	0.05	0.05
ACX390	0.39	0.7	0.42	13.7	0.20	0.01	0.03		

The levels of C are systematically varied to achieve different microstructures. The contents of C and Mn are adjusted to obtain alloys in which room temperature falls between their characteristic martensite start (Ms) and martensite finish (Mf) temperatures. The impact of microalloying with Nb and Ti in the Q&P processing of martensitic stainless steels is also considered.

After casting (in ACERINOX, Spain), the ingots are homogenised for 3 hours at 1270 °C (in CSM, Italy). This is followed by hot rolling in 5-7 passes to produce thick plates of 20 mm thickness. The

final pass temperature is around 1000 °C. Each plate is wrapped in a ceramic cloth to induce slow cooling to room temperature. The realised cooling rate at the plate surface is measured via a thermocouple at around 0.1 °C/s. Finally, all plates are subjected to an annealing treatment at 600 °C for 24 hours. This final heat treatment is intended to reduce the hardness of the plates to allow sample machining, but also to reproduce, at least partly, the industrial batch annealing process, which is commonly used for 13Cr steel hot rolled coils.

The dimensions of these plates are of 500 mm in length along the rolling direction (RD), width in the range of 200 mm to 250 mm along transverse direction (TD), and thickness of about 20 mm. Cylindrical specimens (10 mm in length  $\times$  4 mm in diameter) for dilatometry experiments are machined with the main axis parallel to RD.

### 2.2.2 Experimental Methods

The heat treatments are carried using a DIL805 Bähr dilatometer. The temperature is controlled using a thermocouple spot-welded onto the middle of the sample. All samples are heated in vacuum and cooled with helium. The dilatometric data are post-processed using Origin 2019 software. The dilatometry specimens of the six designed alloys are cylindrical (10 mm length and 4 mm diameter). In all cases, machining of dilatometry specimens is performed using a wire electro-discharge machine (EDM).

Thermodynamic calculations are performed with Thermo-Calc software (2019b, TCFe9 database). These calculations are performed mainly to theoretically predict phase stabilities and critical temperatures Ae1 (lower transformation temperature of austenite) and Ae3 (upper transformation temperature of austenite).

After the application of heat treatments, specimens are metallographically prepared for optical and electron microscopy by grinding and polishing with a final polishing step of 0.05  $\mu\text{m}$  using an OPS suspension for 15 min and etching with Vilella. In order to obtain reliable metallographic pictures, the etching time is varied in the range 10 s to 40 s, depending on the specimen. Optical microscopy examinations are performed with a Leica DMLM optical microscope, whereas a JEOL JSM-6500F field emission gun scanning electron microscope (FEG-SEM) equipped with energy-dispersive X-ray spectroscopy (EDS) detector is used to characterise the microstructures and analyse the elemental composition. All SEM/EDS data are collected at an accelerating voltage of 15 kV.

The fraction of retained austenite in final microstructures are investigated by X-ray diffraction (XRD) and magnetic measurements.

- XRD measurements are carried out on a Bruker D8 Advance diffractometer equipped with a Vantec position sensitive detector, using CoK $\alpha$  radiation. Measurements are performed in the 2 $\theta$  range

from  $40^\circ$  to  $130^\circ$ , using a step size of  $0.034^\circ 2\theta$ , with a counting time per step of 2 s. The profile fitting software DiffracSuit EVA vs 5.2 from Bruker is used to analyse the diffraction peaks. The fraction of retained austenite is determined from XRD measurements by comparing the areas under the ferrite peaks  $\{110\}$ ,  $\{200\}$ ,  $\{211\}$  and  $\{220\}$  with the areas under the austenite peaks  $\{111\}$ ,  $\{200\}$ ,  $\{220\}$  and  $\{311\}$  following the procedure described in [1].

- Magnetic measurements are performed in a LakeShore 7307 Vibration Sample Magnetometer (VSM) using 60–100 mg specimens cut from the middle part of the dilatometry specimens. A standard National Institute of Standards and Technology nickel specimen is used for the calibration. During the measurement, magnetisation curves at room temperature are measured by stepwise changing the applied magnetic field from +1.6 T to -1.6 T. The saturation magnetisation values are obtained by fitting the saturation part of the experimentally obtained magnetisation curve. The volume fraction of retained austenite is determined by comparing the saturation magnetisation values in the austenite-containing specimen and in an austenite-free specimen.

XRD measurement primarily analyses the surface of samples, and the surface preparation process can introduce errors due to the unknown mechanical stability of phases such as retained austenite on sample surface. To complement this, VSM is employed for the preliminary design of heat treatment because it measures bulk material properties. In the following chapters, XRD measurements are conducted separately for each chapter, even when different chapters focus on the same material. This approach ensures that the surface characterisation corresponds accurately to the story in each chapter. While the measured results, particularly the fraction of retained austenite, may vary, they fall within the expected error range, ensuring reliability.

## 2.3 Design of Heat Treatments

### 2.3.1 Austenitisation Conditions

This study starts with the investigation of the austenitisation conditions required to have a fully austenitic microstructure in which carbides are dissolved. This analysis is performed with the material ACX390. Thermocalc calculations of the equilibrium structures present in the materials are shown in **Figure 2.1**, where FCC\_A1 phase represents austenite, BCC\_A2 phase represents ferrite and the rest of phases displayed represent different types of carbides or metastable phases. Note that the “y-axis” indicating phase content is on a logarithmic scale to facilitate visualisation. Results show that austenite starts forming at  $780^\circ\text{C}$ , reaching a volume fraction higher than 0.95 at approximately  $820^\circ\text{C}$ . However, the complete dissolution of carbides occurs at  $1070^\circ\text{C}$ , where full austenitisation is achieved.

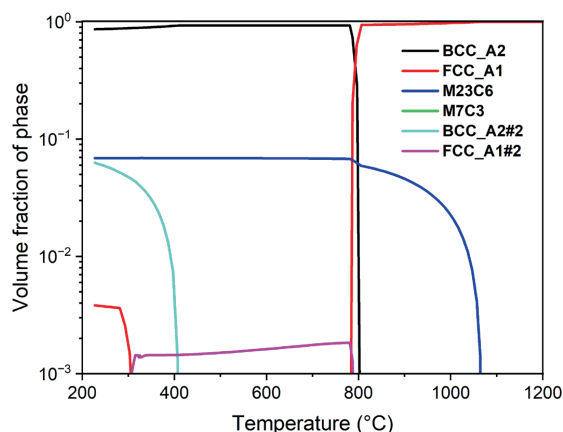
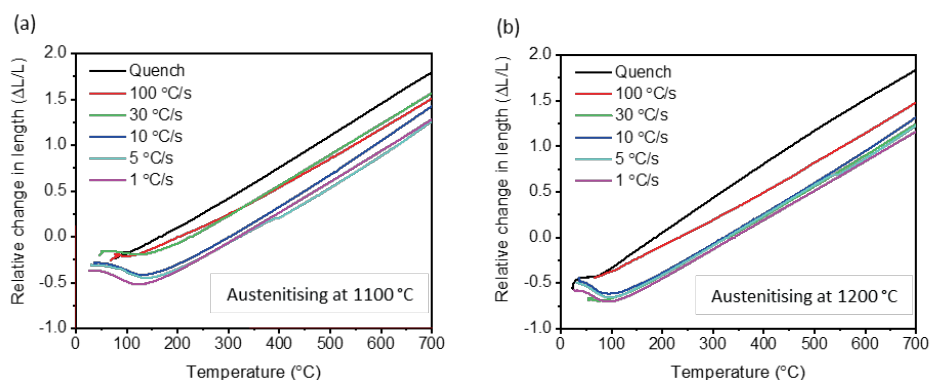


Figure 2.1. Phase diagram of ACX390 calculated with Thermo-Calc.

Considering these calculations, heat treatments including austenitisation at 1100 °C and 1200 °C for 5 minutes, are applied to ACX390. In the same set of experiments, the effect of cooling rate is also investigated, covering 1 °C/s, 5 °C/s, 10 °C/s, 30 °C/s, 100 °C/s and direct quenching. “Quenching” refers to an experiment in which the maximum cooling rate that the current instrument can achieve is applied. Although the cooling rate may not remain constant over the short duration, it is consistently above 100 °C/s. The resulting dilatometry measurements of change in length versus temperature are shown in **Figure 2.2** (a) and (b).

Dilatometry experiments allow the measurement of the  $M_s$  temperature in the steel for all the presented conditions. The  $M_s$  values extracted in this study are intended to assess the completeness of austenitisation rather than to compare exact  $M_s$  temperatures. All  $M_s$  values were derived from dilation curves using a consistent procedure and accounting for the same artificial errors to ensure reliability across the research. Importantly, the  $M_s$  temperature is independent of the cooling rate, and an error margin of 5–10 °C falls well within the accuracy of the testing conditions. When examining **Figure 2.2**, it is evident that the cooling curves for experiments conducted at higher cooling rates are inaccurate. These curves lack a consistent slope during cooling, suggesting potential instrumental issues. Consequently, the corresponding  $M_s$  measurements for these higher cooling rates are unreliable and should be interpreted with caution.

Results are presented in **Table 2.2**.  $M_s$  temperatures are generally higher for samples austenitised at 1100 °C compared to those austenitised at 1200 °C, suggesting that carbides may not fully dissolve after austenitising at 1100 °C for 5 minutes. Additionally, for each austenitisation condition, variations in cooling rates have minimal effect on determining the  $M_s$  temperatures except for the 100 °C/s rate and quenching.

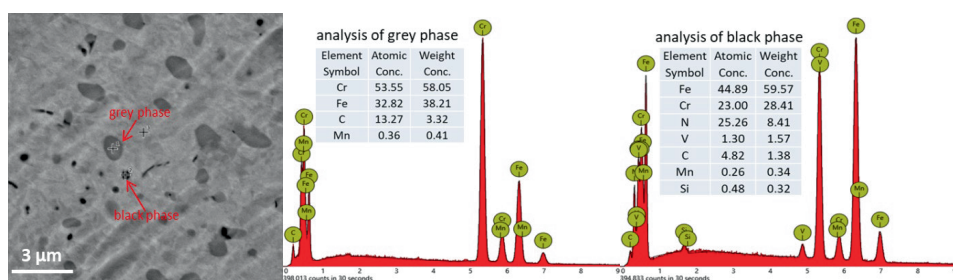


**Figure 2.2.** Dilatometry curves of ACX390 with different cooling rates after austenitising at (a) 1100 °C and (b) 1200 °C.

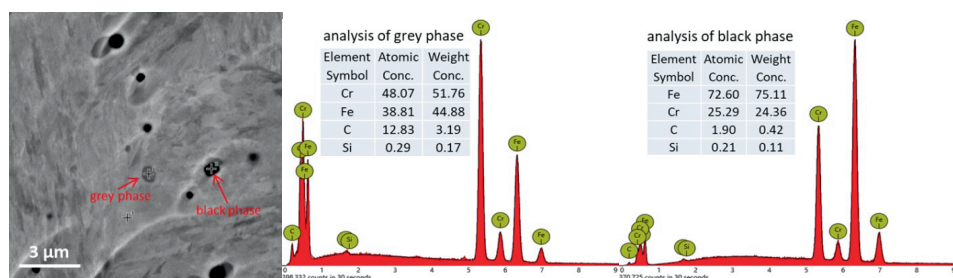
**Table 2.2.** Ms temperatures ( $\pm 5$  °C) after the application of different austenitisation and cooling conditions.

Cooling rate Austenitising	1 °C/s	5 °C/s	10 °C/s	30 °C/s	100 °C/s	Quench
1100 °C 5 min	180	180	185	190	<100	145
1200 °C 5 min	140	145	142	145	<100	90

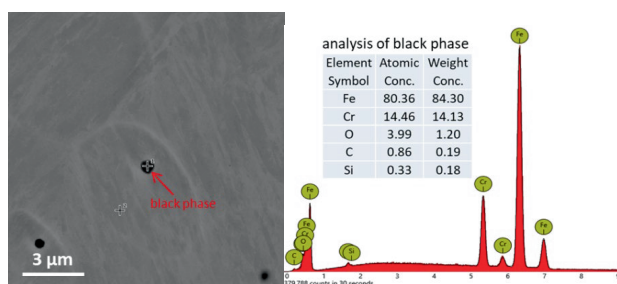
**Figure 2.3** displays the SEM images and EDS analysis of ACX390 at different states to evaluate the presence of undissolved carbides in quenched specimens. Note that the EDS data is not intended for quantitative characterisation. While the presence of C and N is detected, its content is not quantified. **Figure 2.3** (a) shows the initial microstructures, while **Figure 2.3** (b) depicts specimens quenched after austenitisation at 1100 °C for 5 minutes. Both figures reveal two types of precipitates: (i) grey precipitates with large size and irregular shape, that can reach up to 2  $\mu\text{m}$  in length; (ii) small black phase particles, having less than 1  $\mu\text{m}$  in diameter. The analysis showed that the grey particles are chromium carbides while the small black particles are nitrides. Both are present in the initial microstructure. After austenitisation at 1100 °C, chromium carbides are mostly dissolved, leaving small-size particles while nitrides are fully dissolved. After austenitisation at 1200 °C, as shown in **Figure 2.3** (c), almost all carbides are dissolved into the matrix, and only several small particles remained.



(a) Initial microstructure



(b) Austenitising at 1100 °C and quenched microstructure



(c) Austenitising at 1200 °C and quenched microstructure

**Figure 2.3. SEM images and EDS analysis of ACX390 under different conditions: (a) initial microstructure; (b) after austenitising at 1100 °C; (c) after austenitising at 1200 °C. Note: The EDS data is not intended for quantitative characterization. While the presence of carbon (C) and nitrogen (N) is detected, its content is not quantified.**

Investigations performed with alloy ACX390 shows that the dissolution of nitrides seems complete at 1100 °C, while the full dissolution of chromium carbides is not achieved in the studied cases. This may indicate that the austenitisation time selected of 5 min is not long enough to allow full dissolution. Considering the high carbon content in ACX390, Alloy 1C with low carbon is employed to investigate austenitisation time.

Dilatometry curves in **Figure 2.4 (a)** corresponding to Alloy 1C show that austenitising at 1200 °C for 3 minutes and 5 minutes do not lead to full dissolution of carbides. Besides, austenitising for 10 minutes and 15 minutes gives identical martensite transformation curves. **Figure 2.4 (b)** shows the measurement of change in length versus temperature after austenitisation at 1100 °C and 1200 °C for 15 minutes followed by quench in Alloy 1C. The dilatometry curves show similar  $M_s$  temperature in both cases, indicating that austenitisation condition of 1100 °C for 15 minutes can be used in the alloy.

Such a detailed analysis is not performed for the rest of the materials. Instead, austenitisation conditions of 1100 °C and 15 minutes are considered in all cases. According to thermodynamic calculations performed with Thermo-Calc, these conditions should lead to full dissolution of precipitates in all alloys except in the case of alloy 3C HMn-NbTi alloyed with Ti and Nb. In the following section, the response of the materials under different cooling rates is evaluated based on measured  $M_s$  temperatures. Obtaining  $M_s$  temperatures close to each other with increasing cooling rate can also be considered as an indication of full dissolution of carbides.

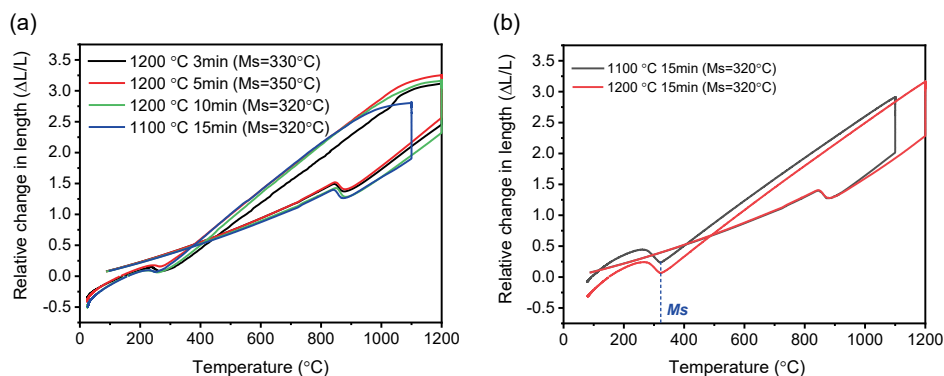


**Figure 2.4. Dilatometry curves corresponding to Alloy 1C: (a) different austenitisation conditions and (b) austenitisation for 15 min at 1100 °C and 1200 °C.**

### 2.3.2 Cooling Rate to Quenching Temperature

In this section, the dependence of the  $M_s$  temperature with cooling rate is investigated for all the six newly-designed alloys. Specimens are subjected to austenitisation at 1100 °C for 15 minutes, followed by cooling at rates of 1 °C/s, 5 °C/s, 10 °C/s, 20 °C/s and quench. Resulting dilatometry curves are shown in **Figure 2.5**. Dilatometry curves corresponding to highest cooling rate (quench) show certain instabilities at high temperatures. This is caused by the cooling gas pumping into the chamber. At that moment helium is injected and samples shift due to gas impact.

The critical temperatures read from the dilatometry curves are summarised in **Table 2.3**. A measurement error of  $\pm 5$  °C is considered. For the case of  $M_s$  measured on quenching, a higher indetermination can be assumed, due to the high temperature instabilities mentioned above. For the rest

of cooling rates, in the range from 1 °C/s to 20 °C/s, results show a slight variation on determining  $M_s$ , with differences that could be attributed to the measurement error.

Considering these observations, a cooling rate of 5 °C/s is selected for the Q&P experiments. This cooling rate allows better control of the microstructure development and a reliable  $M_s$  temperature measurement. Moreover, it is within the cooling rate acceptable for industrial processing, limited to 10 °C/s as maximum possible cooling rate for microstructural control.

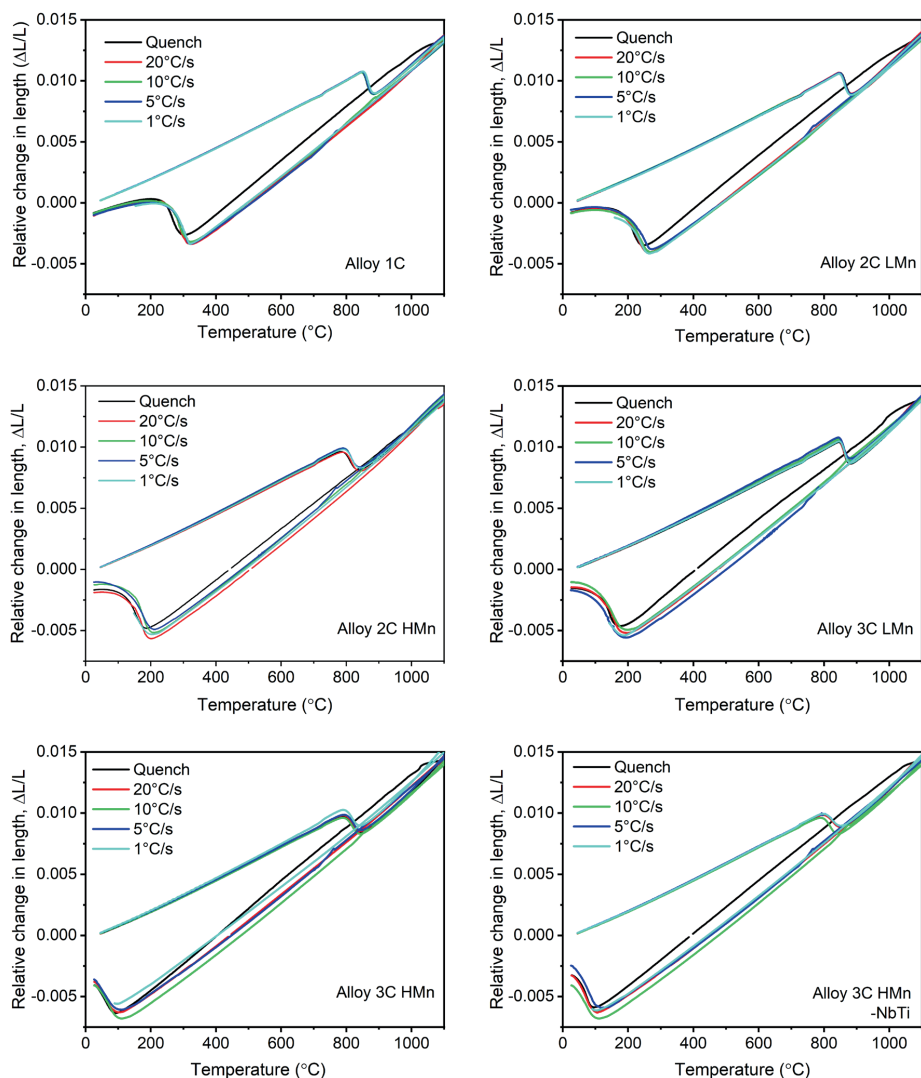


**Figure 2.5. Dilatometric curves of change in length versus temperature for the six steels corresponding to different cooling rates after fully austenitisation.**

**Table 2.3. Ms temperatures measured on cooling at different cooling rates, presented together with Ac1 and Ac3 temperatures determined from dilatometric curves (°C).**

Alloy	Ms- 1 °C/s	Ms- 5 °C/s	Ms- 10 °C/s	Ms- 20 °C/s	Ms- Quench	Ac1	Ac3
1C	340	340	350	340	330	850	920
2C LMn	300	310	310	310	275	850	920
2C HMn	240	240	240	230	230	780	870
3C LMn	230	235	230	230	230	835	930
3C HMn	150	150	155	145	145	780	975
3C HMn-NbTi	150	150	150	145	145	780	1005

### 2.3.3 Optimum Quenching Temperature

The optimum quenching temperature (OQT) is the temperature leading to the maximum fraction of retained austenite under the assumption of full carbon partitioning from martensite to austenite during the partitioning step. **Equation (2-1)**, developed in the QPINOX project ([www.qpinox.eu](http://www.qpinox.eu)), based on previous research [2-7] can be considered for the determination of the martensite start temperature of the carbon-enriched austenite:

$$M_s = 553.7 - 530.8X_C^Y - 9.7X_{Si}^Y - 12.1X_{Cr}^Y - 30.4X_{Mn}^Y \quad (2-1)$$

where  $M_s$  is the martensite transformation start temperature of the carbon-enriched austenite and  $X_i^Y$  indicates the concentration of element “i” in the austenite, in wt.%. The concentration of Si, Mn and Cr is considered equal to the nominal of the alloy, since partitioning takes place under conditions at which the diffusion of substitutionals is unlikely.  $X_C^Y$  represents the carbon in the carbon-enriched austenite. At the OQT, the  $M_s$  temperature of the C-enriched austenite is equal to room temperature, so all this austenite will be retained. By assuming  $M_s$  equal to room temperature, **Equation (2-1)** provides the minimum carbon content in austenite able to completely stabilise C-enriched austenite at room temperature. Under the conditions of full carbon partitioning from martensite to austenite, and considering austenite with the minimum carbon content needed to be fully stabilised at room temperature, the carbon balance in the material is such that [8]:

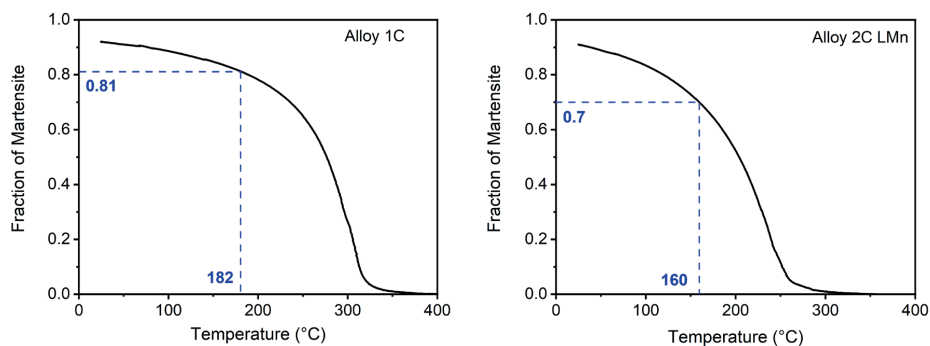
$$f_{OQT}^Y \cdot X_C^Y = X_C^{alloy} \quad (2-2)$$

Where  $X_C^{alloy}$  is the carbon concentration of the alloy and  $f_{OQT}^Y$  is the maximum volume fraction of austenite that can be fully stabilised after full carbon partitioning. The quenching temperature leading to a fraction of untransformed austenite equal to  $f_{OQT}^Y$  is the OQT.

The above procedure applied to the chemical compositions of the six alloys leads to the values of  $f_{OQT}^Y$  (calculated) shown in **Table 2.4**. In order to know the corresponding quenching temperature leading to these fractions of untransformed austenite during the quenching step, it is important to determine the kinetics of martensite formation on cooling. Heat treatments consisting of austenitisation to 1100 °C for 15 minutes followed by cooling at 5 °C/s are investigated. In order to convert dilatometry curves showing martensite formation into kinetic curves showing martensite fraction versus temperature, it is essential to experimentally determine the following data:

- The thermal expansion coefficient of austenite ( $CTE_{FCC}$ ), which can be obtained from the slope of the change in length versus temperature observed during cooling from the austenitisation conditions and before martensite forms.
- The thermal expansion coefficient of martensite ( $CTE_{BCC}$ ). Specimens after cooling at 5 °C/s were put into liquid nitrogen for 20 minutes to form a fully martensitic structure. These specimens are then reheated at 10 °C/s in the dilatometer to 700 °C. The measured slope of the change in length versus temperature during that reheating allowed the calculation of the thermal expansion coefficient of martensite.
- The volume fraction of martensite present at room temperature, in case martensite formation is not complete. In this work, these are determined by magnetic measurements (VSM).

**Table 2.4** shows the thermal expansion coefficients of austenite and martensite as well as the volume fractions of martensite present in the specimens at room temperature after austenitisation to 1100 °C for 15 minutes followed by cooling at 5 °C/s. These values allow the application of the lever rule to the dilatometry curves showing martensite formation, leading to the kinetic curves presented in **Figure 2.6**. These curves allow to determine the quenching temperatures leading to the fractions of untransformed austenite  $f_{OQT}^Y$ , giving rise to the OQT presented in **Table 2.4**.



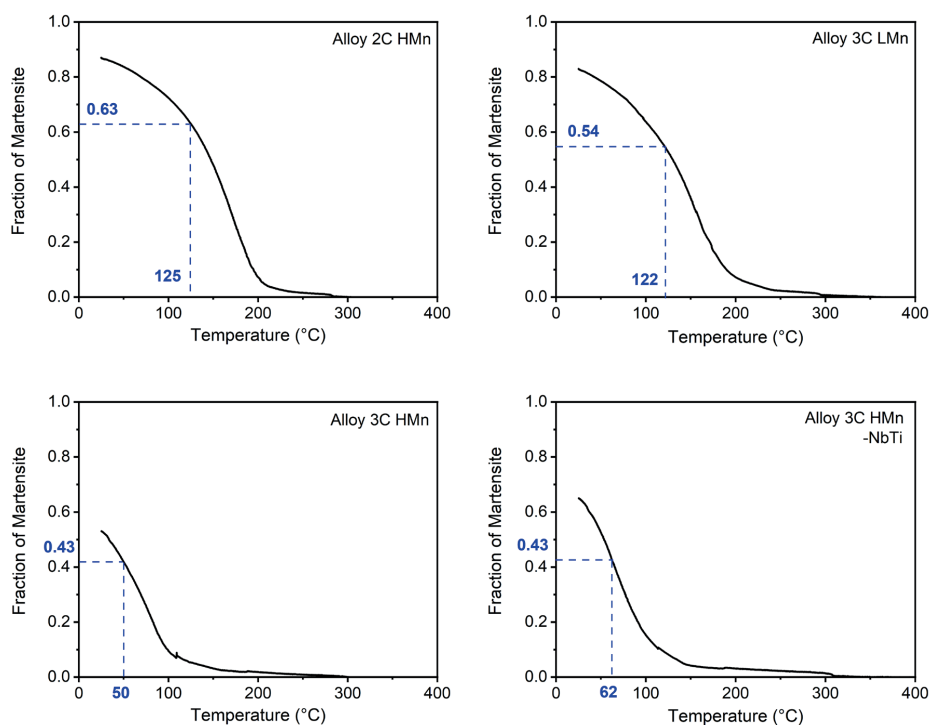


Figure 2.6. Fraction of martensite as a function of temperature formed during cooling at 5 °C/s.

Table 2.4. Calculated values of  $f_{OQT}^{\gamma}$  and OQT. The table also shows the fractions of martensite at room temperature and the thermal expansion coefficients of martensite and austenite.

Alloy	$f_{RT}^{\alpha}$ (VSM)	$CTE_{BCC}$ (K <sup>-1</sup> )	$CTE_{FCC}$ (K <sup>-1</sup> )	$f_{OQT}^{\gamma}$ (calculated)	OQT (°C) (calculated)
1C	0.92	$1.170 \times 10^{-5}$	$2.000 \times 10^{-5}$	0.19	182
2C LMn	0.91	$1.090 \times 10^{-5}$	$1.953 \times 10^{-5}$	0.30	160
2C HMn	0.87	$1.076 \times 10^{-5}$	$1.974 \times 10^{-5}$	0.37	125
3C LMn	0.83	$1.035 \times 10^{-5}$	$1.997 \times 10^{-5}$	0.46	122
3C HMn	0.53	$1.073 \times 10^{-5}$	$1.978 \times 10^{-5}$	0.57	50
3C HMn-NbTi	0.65	$1.028 \times 10^{-5}$	$1.969 \times 10^{-5}$	0.57	62

### 2.3.4 Partitioning Conditions

The partitioning conditions are investigated by referring to the results in published literature and via calculations.

Kinetic calculations are performed to understand the time needed for carbon partitioning during the Q&P process. Such calculations are useful for designing optimum partitioning heat treatments. Calculations are made using the physical model of Santofimia et al., [9,10] considering constrained carbon equilibrium. This model considers the 1 dimensional diffusion of carbon from martensite to austenite, assuming an austenite martensite film morphology, which is appropriate for the Q&P microstructures. In this case, martensite with  $0.2\ \mu\text{m}$  thickness was assumed to share an interface with austenite with  $0.05\ \mu\text{m}$  thickness. This situation corresponds to a system formed by 80 % fraction martensite and 20 % fraction austenite, according to [9,10]. Calculations were performed in half-thickness, assuming mirror conditions for different times at  $450\ ^\circ\text{C}$ . **Figure 2.7** shows the resulting carbon concentration profiles at different moments in time in martensite ( $\alpha'$ ) and austenite ( $\gamma$ ) for the partitioning temperature of  $450\ ^\circ\text{C}$ . The temperature is chosen as typical partitioning temperature, considering the literature on Q&P treatments in 13Cr steels [3,5,6,11,12].

As can be seen from **Figure 2.7**, the carbon distributions in austenite ( $\gamma$ ) show sharp gradients after partitioning for 0.1 s, where carbon concentrates at the austenite next to the martensite/austenite phase boundary. The simulation also illustrates that carbon can quickly escape from martensite. Still, it takes 10 times longer to be uniformly distributed in austenite, which causes a high carbon concentration at the austenite next to the M/A boundary during the early stage of partitioning. Since the sizes of the retained austenite grains can vary in the microstructure, a partitioning time of up to 5 minutes was considered sufficient to ensure carbon homogenisation in the austenite after the partitioning step. Based on these simulations, the partitioning conditions to be investigated are established as  $400\ ^\circ\text{C}$  and  $450\ ^\circ\text{C}$  for 2 and 5 minutes.

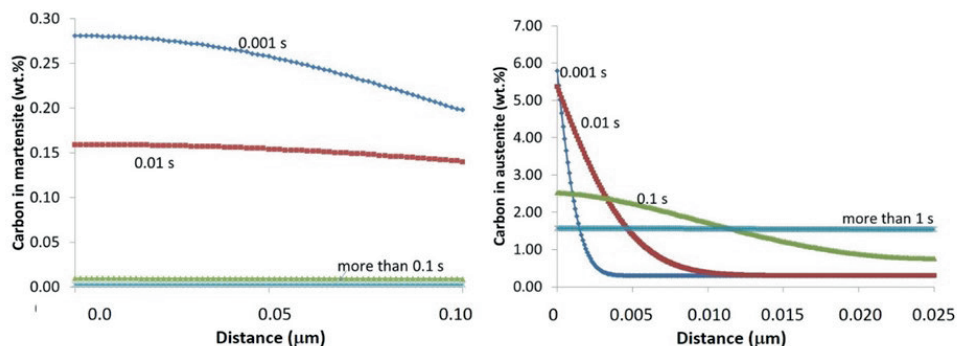


**Figure 2.7.** Carbon concentration profiles at different partitioning times in martensite ( $\alpha'$ ) and austenite ( $\gamma$ ) for Fe-0.3C level alloys for partitioning at  $450\ ^\circ\text{C}$ . Distance 0 indicates the position of the M/A boundary.

## 2.4 Results and Discussion

### 2.4.1 Application of Q&P treatments in the Dilatometer

As a result of the selection procedure explained in previous sections, thermal treatments following the schema presented in **Figure 2.8** are applied in the dilatometer to specimens of the six alloys. The quenching temperatures considered are the optimum quenching temperatures in **Table 2.4** for all alloys and room temperature for alloys 2C HMn, 3C LMn, 3C HMn and 3C HMn-NbTi.

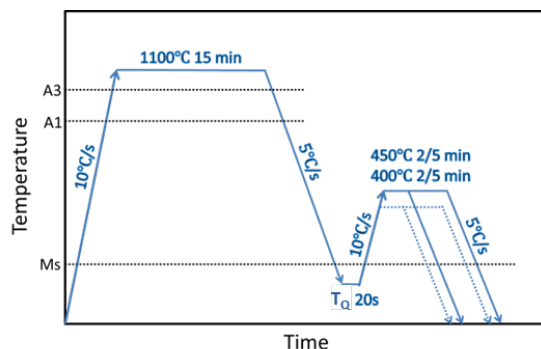


**Figure 2.8.** Selected Q&P heat treatments.

The final quenching step shows formation of martensite in specimens of alloy 2C HMn and 3C LMn after partitioning at 450 °C. In contrast, no fresh martensite formation is observed in the rest of the cases. These cases consider two additional quenching temperatures, assuming temperatures yielding to 0.05 and 0.10 less retained austenite (**Figure 2.6**). This leads to quenching temperatures of 119 °C and 104 °C for alloy 2C HMn and 114 °C and 99 °C for alloy 3C LMn. The resulting dilatometry curves show the absence of fresh martensite after partitioning at 450 °C for 5 minutes if the lowest quenching temperatures are used, that is, 104 °C for alloy 2C HMn and 99 °C for alloy 3C LMn. These two temperatures will substitute the previous OQTs. The theoretical analysis performed in the previous section shows alloys 2C HMn, 3C LMn, 3C HMn and 3C HMn-NbTi as suitable for Q&P treatments with the quenching temperature equal to room temperature (RT), as they display a significant fraction of retained austenite at this temperature. These heat treatments are applied in the dilatometer to the mentioned alloys considering the four selected partitioning conditions. **Table 2.5** provides a summary of the quenching conditions selected for each alloy.

It is important to note that the heat treatment design employed cylindrical specimens machined from a 20 mm-thick slab. Cylindrical specimens were chosen for their ability to provide more reliable and consistent results compared to thin flat specimens in dilatometry. All materials underwent the same rolling process, followed by the Q&P treatment. Austenitisation at 1100 °C for 15 minutes ensured complete recrystallisation. Consequently, the effect of texture can be excluded, and any differences in

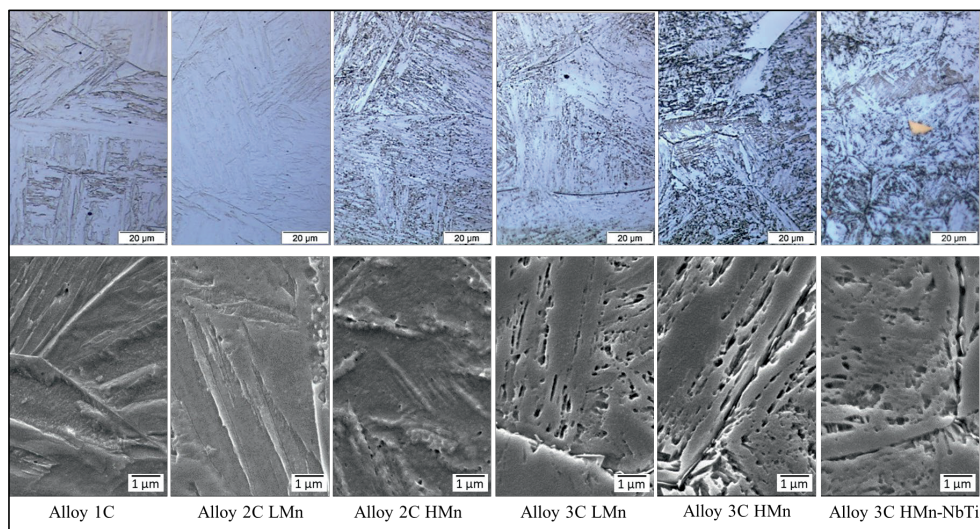
the subsequently characterised properties can be attributed solely to variations in the Q&P heat treatment.

Table 2.5. Summary of selected quenching conditions per alloy.

Alloy	Quenching temperature (°C)	Temperature identification	Aimed fraction of retained austenite
1C	182	OQT	0.19
2C LMn	160	OQT	0.30
2C HMn	104	OQT	0.29
	RT	RT	0.13
3C LMn	99	OQT	0.36
	RT	RT	0.17
3C HMn	50	OQT	0.57
	RT	RT	0.47
3C HMn-NbTi	62	OQT	0.57
	RT	RT	0.35

2.4.2 Microstructure Characterisation

Figure 2.9 displays the microstructure of the six alloys after direct cooling from austenitisation to room temperature. Optical microscopy shows the formation of an acicular structure. Prior austenite grain boundaries can be identified. For alloys 3C LMn, 3C HMn and 3C HMn-NbTi, precipitates inside prior austenite grain boundaries can be observed. In alloy 3C HMn-NbTi, bright yellow particles at grain boundaries are observed.



**Figure 2.9. OM (top row) and SEM (bottom row) microstructures of directly quenched alloys.**

**Figure 2.10** displays the microstructure of the six alloys cooled from austenitisation to optimum quenching temperature followed by partitioning at 450 °C for 5 minutes (OQT-Q&P). For alloys 1C, 2C LMn and 2C HMn, observations by optical microscopy reveal martensitic laths in a uniform etched matrix. Similar structures are observed by SEM analysis. The techniques do not clearly distinguish the different phases present in the microstructure. For alloys 3C LMn and 3C HMn, prior austenite grain boundaries are clearly depicted. SEM micrographs show the lath-shaped structure with small particles.

In alloy 3C HMn-NbTi, prior austenite grain boundaries are clearly visible in the optical micrographs, showing austenite grains smaller in size than those in other investigated alloys. SEM micrographs show similar microstructures to those in alloys 3C LMn and 3C HMn, combining lath-shaped features, small precipitates, and larger unetched areas, probably constituting retained austenite and/or fresh martensite.

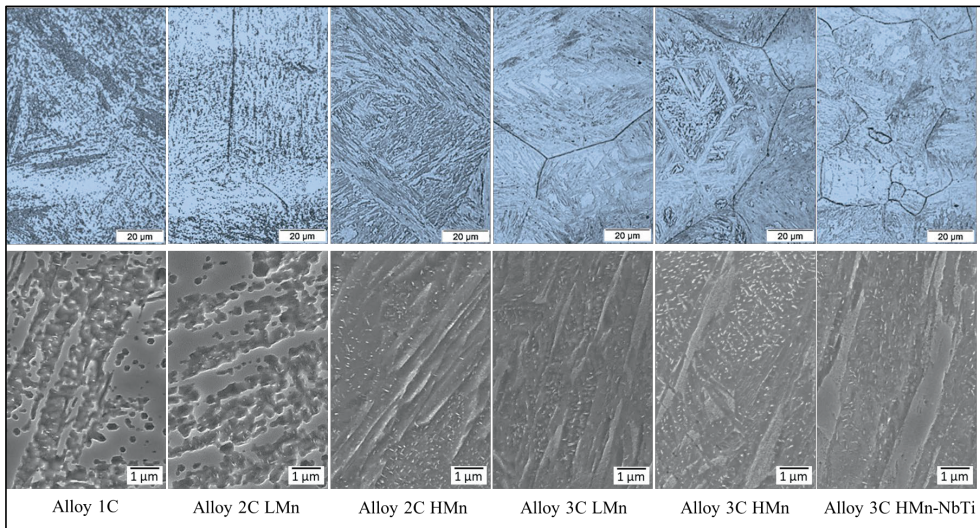


**Figure 2.10. OM (top row) and SEM (bottom row) microstructures of OQT-Q&P processed alloys.**

**Figure 2.11** displays the microstructure of the four alloys cooled from austenitisation to room temperature followed by partitioning at 450 °C for 5 minutes (RT- Q&P).

For alloy 2C HMn, microstructures look very similar before and after partitioning. Optical micrographs show lath-shaped structures, also visible in the SEM. Small white precipitates are revealed in the SEM, presumably retained austenite or carbide particles. In alloy 3C LMn, white needle-like precipitates are observed. Large white particles are distributed in the matrix. Both types of precipitates seem to have formed during the partitioning step.

For alloy 3C HMn, after partitioning, optical microscopy shows a banded morphology. Within the etched band, some regions remain unetched. These may contain fresh martensite and/or retained austenite. These unetched locations look like islands in the SEM micrographs, and are surrounded by laths of possibly tempered martensite. For alloy 3C HMn-NbTi, after partitioning, microstructural bands are more clearly observed. Prior austenite grain boundaries are clearly defined by OM and SEM, showing a substructure that seems to be different from the one present in the matrix. Ti precipitates are visible.

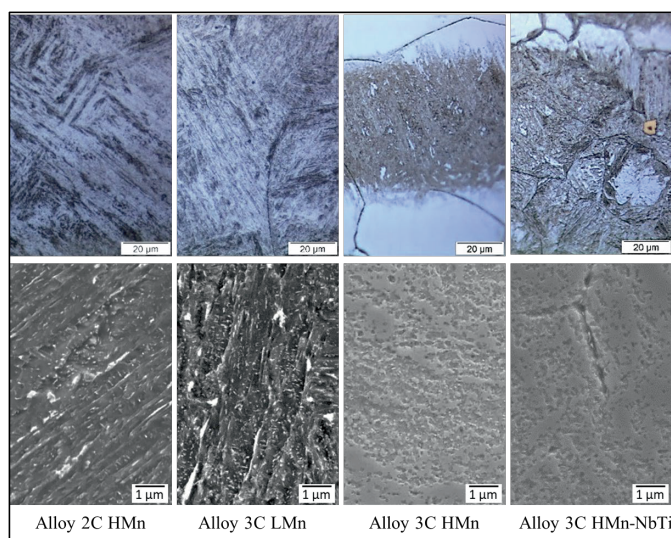


**Figure 2.11. OM (top row) and SEM (bottom row) microstructures of RT- Q&P processed alloys 2C HMn, 3C LMn, 3C HMn, 3C HMn-NbTi.**

## 2.5 Summary

Six chemistries have been designed, varying in C, Mn and microalloying elements. Quenching and partitioning heat treatments applicable to the designed alloys have been selected, with alloys 2C HMn, 3C LMn, 3C HMn, 3C HMn-NbTi having RT-Q&P capability. The research in the following chapters is based on these materials, as explained in **Table 2.6**.

**Table 2.6. Overview of alloys used in subsequent chapters.**

Chapter	Alloy	Processing	Aim
3	3C LMn 3C HMn	Varying $T_Q$ Partitioning at 450 °C for 5 minutes	To investigate the microstructure development during Q&P heat treatment and explore the competing reactions involved.
4	3C LMn 3C HMn	$T_Q = RT$ Partitioning at 400 °C for 5 minutes	To study the process of carbon partitioning and understand the microstructure development during partitioning.
5	2C LMn 3C LMn 3C HMn-NbTi	$T_Q = OQT$ and RT Partitioning at 450 °C for 5 minutes	To investigate the relationship between microstructure and corrosion.
6	3C HMn 3C HMn-NbTi	$T_Q = OQT$ Partitioning at 450 °C for 5 minutes	To investigate the impact of microalloying elements on corrosion performance.

## References

- [1] C.F. Jateczak, J.A. Larson, S.W. Shin, SAE apecial publication 453 retained austenite and its measurements by X-ray Diffraction, 1980.
- [2] Q.L. Huang, C. Schröder, H. Biermann, O. Volkova, J. Mola, Influence of martensite fraction on tensile properties of quenched and partitioned (Q&P) martensitic stainless steels. *Steel Res Int* 2016; 87: 1082–1094. <https://doi.org/10.1002/srin.201500472>
- [3] T. Tsuchiyama, J. Tobata, T. Tao, N. Nakada, S. Takaki, Quenching and partitioning treatment of a low-carbon martensitic stainless steel. *Materials Science and Engineering: A*, 532(2012) 585–592. <https://doi.org/10.1016/j.msea.2011.10.125>
- [4] S.Y. Lu, K.F. Yao, Y.B. Chen, M.H. Wang, N. Chen, X.Y. Ge, Effect of quenching and partitioning on the microstructure evolution and electrochemical properties of a martensitic stainless steel. *Corrosion Science*, 103(2016) 95–104. <https://doi.org/10.1016/j.corsci.2015.11.010>
- [5] J. Tobata, K. Ngo-Huynh, N. Nakada, T. Tsuchiyama, S. Takaki, Role of silicon in quenching and partitioning treatment of low-carbon martensitic stainless steel. *ISIJ International*, 52(2012) 1377–1382. <https://doi.org/10.2355/isijinternational.52.1377>
- [6] J. Mola, B.C. De Cooman, Quenching and partitioning (Q&P) processing of martensitic stainless steels. *Metallurgical and Materials Transactions A*, 44(2013) 946–967. <https://doi.org/10.1007/s11661-012-1420-1>
- [7] Q.L. Huang, O. Volkova, H. Biermann, J. Mola, Dilatometry analysis of dissolution of Cr-rich carbides in martensitic stainless steels. *Metallurgical and Materials Transactions A*, 48(2017) 5771–5777. <https://doi.org/10.1007/s11661-017-4377-2>
- [8] J. Speer, D.K. Matlock, B.C. De Cooman, J.G. Schroth, Carbon partitioning into austenite after martensite transformation. *Acta Materialia*. 51(2003) 2611–2622. [https://doi.org/10.1016/S1359-6454\(03\)00059-4](https://doi.org/10.1016/S1359-6454(03)00059-4)
- [9] M. J. Santofimia, L. Zhao, and J. Sietsma, Model for the interaction between interface migration and carbon diffusion during annealing of martensite–austenite microstructures in steels. *Scripta Materialia*, 59(2008) 159–162. <https://doi.org/10.1016/j.scriptamat.2008.02.045>
- [10] M.J. Santofimia, J.G. Speer, A.J. Clarke, L. Zhao and J. Sietsma, Influence of interface mobility on the evolution of austenite-martensite grain assemblies during annealing. *Acta Materialia*, 57(2009) 4548–4557. <https://doi.org/10.1016/j.actamat.2009.06.024>
- [11] L. Yuan, D. Ponge, J. Wittig, P. Choi, J. A. Jimenez and D. Raabe, Nanoscale austenite reversion through partitioning, segregation and kinetic freezing: Example of a ductile 2GPa Fe-Cr-C steel. *Acta Materialia*. 60(2012) 2790–804. <https://doi.org/10.1016/j.actamat.2012.01.045>

- [12] S. Dieck, P. Rosemann, A. Kromm and T. Halle, Reversed austenite for enhancing ductility of martensitic stainless steel. *IOP Conference Series: Materials Science and Engineering*, 181(2017) 0102354. <http://dx.doi.org/10.1088/1757-899X/181/1/012034>



## 3

## Microstructure Development of Q&P Processed Martensitic Stainless Steels with Different Manganese Content

3

This chapter is based on:

Li G, Kwakernaak C, Smith A, Muratori M, Gonzalez-Garcia Y, Santofimia MJ. Microstructure development of quenching and partitioning-processed martensitic stainless steels with different manganese content. *Materials Science and Technology*. 2024; 40(6):449-465.



### 3.1 Introduction

The Quenching and Partitioning (Q&P) process is a heat treatment introduced for creating advanced high-strength steels (AHSSs) with microstructures containing retained austenite (RA) in a martensitic matrix, leading to good combinations of strength and ductility [1-3]. The Q&P process consists of four steps: (1) the austenitisation step, during which the steel is fully or partially austenitised, and the characteristics of the parent austenite like grain size, composition homogeneity, and morphology can be controlled via appropriate heat treatment parameters; (2) the quenching step, during which the austenitised microstructure is quenched to a temperature between the martensite start ( $M_s$ ) temperature and the martensite finish ( $M_f$ ) temperature, aiming to obtain a controlled combination of austenite and martensite in the microstructure; (3) the partitioning step, in which the material is kept at a constant temperature (same or higher than the quenching temperature) to promote the redistribution of carbon from martensite to austenite [4-6]; and (4) the final quenching step, during which the partitioned microstructure is cooled down to room temperature, and fresh martensite may form. The formation of fresh martensite, which typically reduces the ductility of steels [5-7], can be prevented by an appropriate design of the heat treatment schedule. This approach ensures high fractions of retained austenite while avoiding fresh martensite in the final microstructure [7].

The process of carbon partitioning from martensite into austenite is essential for austenite stabilisation, of which the thermodynamics was initially described by the constrained carbon equilibrium (CCE) model proposed by Speer [2], as already detailed in **Chapter 1**. The CCE model can be also applied to predict the quenching temperature leading to a maximum in the volume fraction of retained austenite, for which the three aforementioned conditions are coupled with equations describing martensite transformation kinetics [8]. However, studies found that the CCE model is unlikely to be satisfied during actual Q&P processing because carbide precipitation and other competing reactions may take place [9-11]. Competing reactions consume carbon that otherwise should be available for partitioning into the austenite. These observations led to adaptations of the CCE model taking into account competing processes [12-16].

The application of the CCE model to describe the carbon partitioning process during the application of Q&P heat treatments to stainless steels has been less investigated than in carbon steels. Several authors have found that the CCE model is not directly applicable to stainless steels due to the presence of competing reactions. For example, the carbon content present in retained austenite has been found to deviate with respect to the expected according to the CCE assumptions due to the occurrence of carbide precipitation [17-20]. Austenite reversion may also take place, affecting the fraction of phase constituents [17]. Martensite/austenite interface migration, driven by the difference in the chemical potential of the metal atoms (Fe–Cr), was also revealed [20]. In contrast to those previous observations,

the nearly ideal CCE condition was realised with the appropriate addition of Si [21], indicating that the applicability of the CCE model also relates to special elements that could inhibit the competing reactions.

Different alloying elements are considered in the design of Q&P steels, with carbon being the main element, while Mn, Si, Al and Cr are added for their important roles in suppressing the formation of cementite and stabilising retained austenite [22,23]. Among these alloying elements, Mn is added to promote austenitic microstructures by lowering the free energy of austenite, stabilising the phase [24]. However, Mn segregation is frequent in most Mn-alloyed steels [25-30]. For the case of carbon steels processed by the Q&P process, several studies indicate the presence of Mn segregation. In particular, Mn segregation produces banded microstructures during the Q&P process since it affects the local Ms temperature [26-28], which can cause large hardness gradients and trigger different fracture mechanisms [29,30]. Microstructural bands and inhomogeneity in these cases can be minimised by applying lower quenching temperatures to decrease the difference between the fraction of primary martensite among the bands [27,31].

Cr is an essential alloying element to provide corrosion resistance in stainless steels. Cr addition inhibits bainite formation, which simplifies microstructure control during the application of the Q&P process in stainless steels with respect to carbon steels [19]. Theoretically, Cr was assumed to replace the role of Si in retarding the formation of carbides [19,21] because Cr reduces carbon diffusivity in austenite by decreasing carbon thermodynamic activity. In earlier studies focused on stainless steels, researchers noted the presence of  $M_{23}C_6$ -type Cr-carbides in ferritic stainless steels after undergoing the Q&P treatment [34,35]. However, a key question remains unanswered: whether these carbides formed during the initial quenching [27] or during the subsequent partitioning step. In contrast, when examining Q&P treated martensitic stainless steels in prior research [17-21,36], investigators consistently detected  $M_3C$  and  $M_7C_3$  carbides within the martensitic structure, but there was no evidence of  $M_{23}C_6$  carbides in any of the studies conducted. The high content of Cr in stainless steels raised concerns regarding elemental segregation due to its low diffusion in steels [32,33], and Cr segregation has been observed in one Cr-containing Q&P treated medium carbon steel [31]. Cr segregation may have an effect on the microstructure homogeneity and the local presence of Cr-carbides.

Based on this analysis, carbide precipitation may not be completely prevented, leading to competition with the "pure partitioning" process, consequently influencing microstructure evolution. This observation raises two intriguing questions that remain unexplored with regard to the suitability of the Q&P process for martensitic stainless steels. The first aspect is determining which are the most relevant processes competing for the carbon available for carbon partitioning in this type of steel and how they affect the applicability of the CCE model. The second aspect is to elucidate the influence of chromium/manganese band segregation, present in stainless steels, on the microstructure development.

In order to answer these questions, this work investigates the microstructure development under different Q&P conditions in two martensitic stainless steels with different Mn content. Particularly, the presence of reactions competing for the carbon and the influence of manganese/chromium bands are experimentally studied. Results are discussed in the context of the applicability of the CCE model to stainless steels.

### 3.2 Materials and Experimental Methods

The chemical compositions of the two medium-carbon stainless steels investigated in this work are given in **Table 3.1**. The two alloys 3C LMn and 3C HMn designed in **Chapter 2** are designated as LMn and HMn in this chapter for simplicity. Alloy LMn contains 0.31 wt.% C and 0.77 wt.% Mn and alloy HMn contains 0.32 wt.% C and 3.00 wt.% Mn, in which the concentration of all other alloying elements remains the same. The fabrication process can be found in **Chapter 2**.

**Table 3.1. Chemical composition of the steels, in wt.%.**

Alloy	C	Mn	Si	Cr	Ni	Al	N	Fe
LMn	0.31	0.77	0.3	13.1	0.20	0.005	0.03	balance
HMn	0.32	3.00	0.3	13.1	0.20	0.002	0.03	balance

Cylindrical specimens with 10 mm in length and 4 mm in diameter are machined by electron discharge machining (EDM) from the slabs with the long axis parallel to the rolling direction. Heat treatments are applied with a DIL805 D Bähr/TA dilatometer to obtain different Q&P microstructures. The temperature is controlled using an S-type thermocouple that is spot-welded onto the middle of the cylindrical specimens. Two quartz rods are used for clamping. During the heating and isothermal holding segments, a vacuum of approximately  $10^{-4}$  mbar is maintained in the chamber. Helium is used during the cooling process to control the cooling rate. **Figure 3.1** shows a scheme of the heat treatments applied to the cylindrical specimens in the dilatometer. Selected heat treatments are applied ending at temperatures below room temperature for a better observation of martensite kinetics and possible determination of the  $M_s$  temperature corresponding to fresh martensite ( $M_2$ ) in the last quench. The heat treatments that are considered for this additional investigation will be mentioned in section “3.4.1 Results” as they are needed in the argumentation. These “sub-zero” heat treatments are also applied in the same dilatometer.

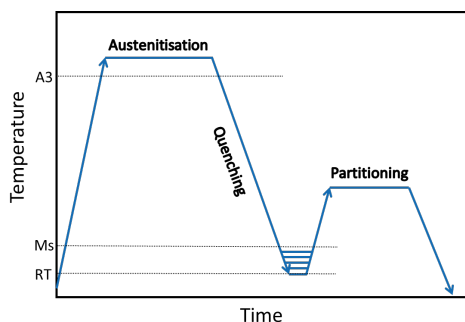


**Figure 3.1. Scheme of the Q&P heat treatments applied to LMn and HMn alloys.**

3

After heat treatment, the specimens are cut in half, and the surfaces are prepared for metallographic analysis. Firstly, they are ground using P800, P1000, P1200 and P2000 abrasive papers. Next, they are polished with 3  $\mu\text{m}$  and 1  $\mu\text{m}$  diamond paste. Finally, samples are polished with an OPS suspension for 15 minutes and then washed with soap to remove the OPS stains and ultrasonically cleaned in isopropanol for 10 minutes. To reveal the microstructure, a Vilella reagent consisting of 1 g picric acid, 5 ml HCl and 100 ml ethanol is applied. All samples are metallographically prepared using the same procedure, with an identical etching time of 15 seconds. This solution outlines the carbides and etches the martensite. The etched microstructures are analysed by Light Optical Microscopy (LOM) and with a Field Emission Gun Scanning Electron Microscope (FEG-SEM, JEOL JSM-6500F) operating at 15 kV and 10 mm working distance.

To assess the degree of carbon partitioning, the volume fraction and carbon concentration of austenite after Q&P treatment are evaluated by X-ray diffraction (XRD) experiments in a Bruker D8-Advance diffractometer, in which the phase constituents and the austenite lattice parameter at room temperature are measured. Diffraction angles in the range of  $45^\circ < 2\theta < 130^\circ$  are measured with Co K $\alpha$  radiation, using a step size of  $0.035^\circ$   $2\theta$  with a counting per step of 4 s. This  $2\theta$  range covers the (110), (200), (211), (220) martensite peaks and the (111), (200), (220), (311) austenite peaks. The carbon concentration within the retained austenite is calculated from its lattice parameter  $a$ . Since there is no specific empirical formula developed for Q&P processed stainless steels, we chose two commonly used empirical formulas given by **Equation (3-1)** [36] and **Equation (3-2)** [37] for comparison.

$$a(\text{nm}) = 0.3578 + 0.0033 \text{ wt. \%C} + 0.000095 \text{ wt. \%Mn} - 0.00002 \text{ wt. \%Ni} + 0.00006 \text{ wt. \%Cr} + 0.00056 \text{ wt. \%Al} + 0.00031 \text{ wt. \%Mo} + 0.00018 \text{ wt. \%V} \quad (3-1)$$

$$a(\text{nm}) = 0.3556 + 0.00453 \text{ wt. \%C} + 0.000095 \text{ wt. \%Mn} - 0.00002 \text{ wt. \%Ni} + 0.00006 \text{ wt. \%Cr} + 0.00056 \text{ wt. \%Al} + 0.00031 \text{ wt. \%Mo} + 0.00018 \text{ wt. \%V} \quad (3-2)$$

Electron probe microanalysis (EPMA) is performed with a JEOL JXA 8900R microscope to quantify elemental segregation using an electron beam with an energy of 10 keV and beam current of

100 nA employing Wavelength Dispersive Spectrometry (WDS). The composition at each analysis location of the sample is determined using the X-ray intensities of the constituent elements after background correction relative to the corresponding intensities of reference materials. The obtained intensity ratios are processed with a matrix correction program CITZAF [38].

### 3.3 Heat Treatments

#### 3.3.1 Austenitisation Conditions and Cooling Rate

According to thermodynamic calculations and experiments performed in **Chapter 2**, austenitisation conditions of 1100 °C for 15 minutes are employed in the present work.

The dependence of the martensite start temperature on the cooling rate is investigated for both LMn and HMn alloys. Specimens are subjected to austenitisation at 1100 °C for 15 minutes, followed by cooling at rates of 5 °C/s, 10 °C/s, 20 °C/s and quench. The dilatometry curves do not show any difference in Ms temperature, as also detailed in **Chapter 2**. For clarity, only one curve corresponding to cooling at 5 °C/s is shown in **Figure 3.2**.

For better visualisation of the martensite formation kinetics, differential curves around the Ms temperature in the cooling section are included as dashed lines. The initiation of the martensite transformation during cooling is indicated by a drop in the differential curve. In **Figure 3.2 (a)**, for alloy LMn, the measured Ms temperature is 230 °C, while the most rapid transformation kinetics are observed at 200 °C. In **Figure 3.2 (b)**, for alloy HMn, the Ms is at 150 °C, and the quickest transformation kinetics occur at 100 °C. It is noteworthy that, in both alloys, prior to reaching the Ms temperature during cooling, there are slight fluctuations on the differential curves. These fluctuations manifest as gradual changes in the dilatometry curves, suggesting the possibility of a minor presence of previously transformed martensite with a higher Ms temperature, potentially due to microstructural or chemical heterogeneities. The transformation is not completed in any of the alloys at room temperature.

Considering these observations, a cooling rate of 5 °C/s is selected for all experiments. This cooling rate allows better control of the microstructure development and a reliable Ms temperature measurement.

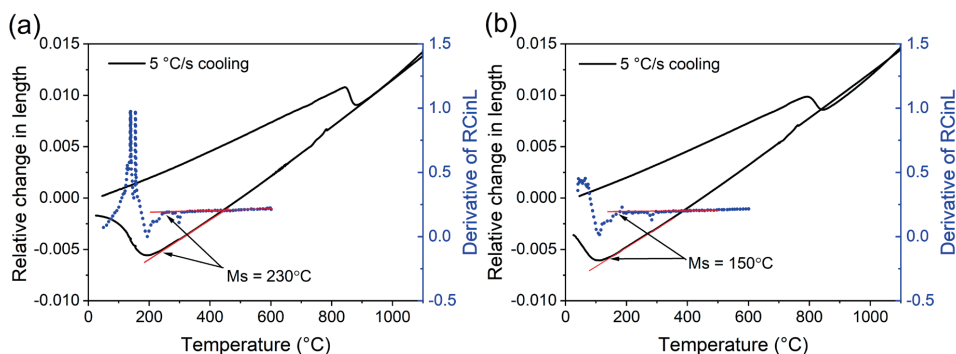


**Figure 3.2.** Dilatometry curves of relative change in length (RCinL) versus temperature (continuous line) and corresponding change in slope (blue dotted line) during Q&P treatment for (a) alloy LMn and (b) alloy HMn. The arrows point to the drop in the differential curves, indicating the start temperatures of the martensitic transformation.

### 3.3.2 Characterisation of Martensite Formation and Selection of Quenching Temperatures

In order to obtain appropriate quenching temperatures for the formation of controlled fractions of martensite, it is necessary to carefully determine the martensite transformation kinetics. This is achieved by relating dilatometry curves showing martensite formation with kinetic curves showing martensite fraction. For this purpose, the thermal expansion coefficient (CTE) of austenite and martensite and the fraction of martensite present at room temperature must be known.

We employ the same method and procedure detailed in **Chapter 2**, specifically in section 2.3.3 (*Optimum Quenching Temperature*), to determine the CTE for both austenite and martensite. The XRD measurements determined the volume fractions of martensite present at room temperature, resulting in values of 0.89 for alloy LMn and 0.68 for alloy HMn. These fractions are subsequently employed in the lever rule calculations.

The experimental results obtained above are plotted together in **Figure 3.3** (a) and (b) for alloys LMn and HMn, respectively, with the CTE obtained of martensite (bcc) and austenite (fcc) presented. From these curves, the martensite fraction formed at a given temperature during continuous cooling to room temperature can be estimated based on the lever rule, leading to the curves presented in **Figure 3.3** (c) and (d).

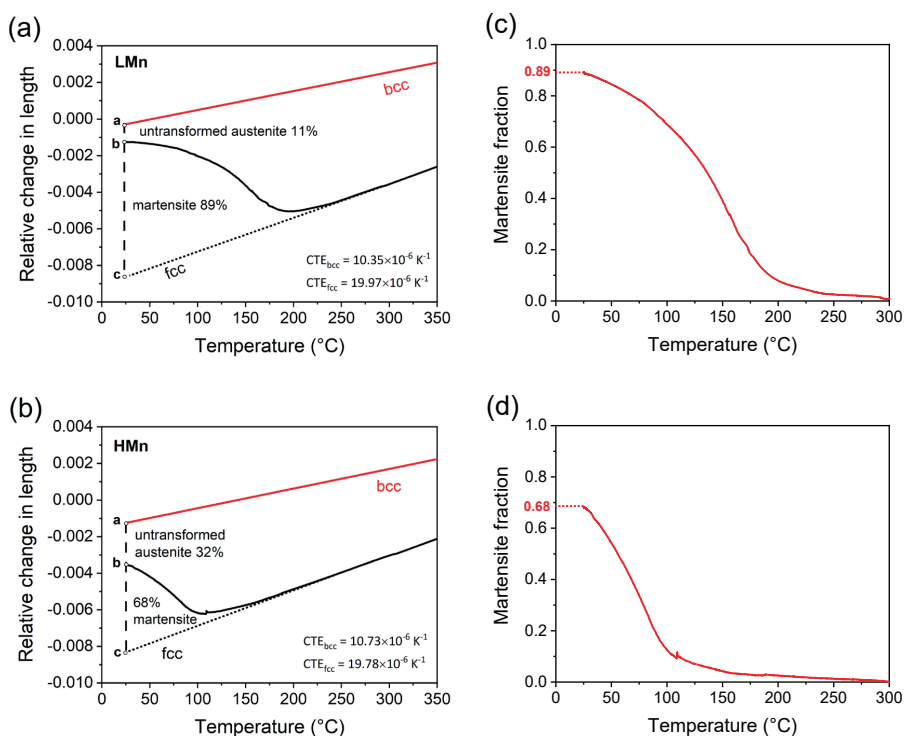


**Figure 3.3. Relative Change in length versus temperature during cooling and reheating and experimental volume fraction of martensite calculated applying lever rule for alloy LMn (a)(c) and alloy HMn (b)(d), respectively.**

Five quenching temperatures, ranging from room temperature (RT) with 25 °C – 30 °C increments up to close to the  $M_s$ , are selected for precise investigation for each alloy. These selected quenching temperatures and corresponding martensite fractions are shown in **Figure 3.4**. Materials are held at the quenching temperature for 20 s, which is sufficiently long to stabilise the temperature in the specimen without any phase transformation.

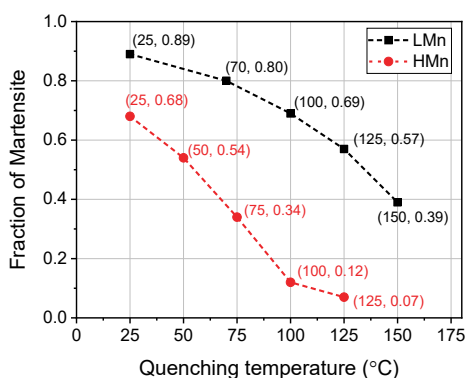


**Figure 3.4.** Selected quenching temperatures for Q&P heat treatments and corresponding fraction of primary martensite as determined by the lever rule.

### 3.3.3 Selection of the Partitioning Conditions

Previous investigations by Mola et al. [36] on the Q&P processing of martensitic stainless steels have shown that after quenching to conditions leading to a fraction of martensite of 0.65, partitioning at 450 °C for 3 min is sufficient for full stabilisation of the remaining austenite without fresh martensite formed in the final microstructure. Additionally, the works of [19] and [21] showed that partitioning conditions of 450 °C for 10 min leading to a fraction of martensite of 0.80 also allowed significant retention of austenite at room temperature, although precipitation of  $M_3C$  and  $M_7C_3$  types of carbides occurred at the retained austenite/martensite interfaces. Based on the simulations and experimental tests conducted in **Chapter 2** (section 2.3.4, *Partitioning Conditions*), we selected partitioning conditions of 450 °C for 5 minutes in the present investigation. This choice aims to maximise carbon partitioning while minimising the precipitation of carbides.

The heating rate from the quenching temperature to the partitioning temperature is 10 °C/s. Additionally, the cooling rate after partitioning is selected to remain consistent with the initial cooling rate, 5 °C/s. Since the present work involves different quenching temperatures, it is expected that the competition between carbon partitioning and carbide precipitation will be affected by the fraction of austenite present at the partitioning step.

## 3.4 Results

### 3.4.1 Analysis of Dilatometry Curves

**Figure 3.5** (a) shows relative length changes versus temperature measured during the application of Q&P treatments to LMn specimens. Only a section of the curve is displayed to better visualize the martensite transformation and  $M_s$  temperature. Some of the presented heat treatments ended at sub-zero

temperatures. Martensite starts forming at 230 °C (Ms1), leading to different fractions of martensite ranging from 0.89 to 0.39 as a function of the quenching temperatures, as explained in section 3.3. Specimens are then reheated to the partitioning temperature of 450 °C, where the material is held for 5 minutes. After the partitioning stage, specimens are cooled to room temperature forming fresh martensite at a temperature Ms2 in specimens initially quenched to 125 °C (Ms2 = 70 °C) and 150 °C (Ms2 = 125 °C). When the final quench is down to -120 °C, the formation of fresh martensite is observed at a temperature Ms2 in the dilatometry curves of specimens initially quenched to 25 °C (Ms2 = -50 °C), 70 °C (Ms2 = -10 °C), and 100 °C (Ms2 = 10 °C).

**Figure 3.5(b)** shows the relative change in length versus time during the quenching and reheating stages for alloy LMn. The 20 s holding at  $T_Q$  does not show any sign of phase transformation. The changes in the thermal expansion coefficient displayed in the reheating stage for different specimens correspond to the differences in phase fractions, i.e., the lower the fraction of martensite formed in the first quench (M1), the higher the expansion coefficient. The change in length observed during the partitioning step depends on the quenching conditions, as shown in **Figure 3.5(c)**. In the case of quenching to 25 °C, a continuous expansion is observed. For specimens quenched to 70 °C, 100 °C, and 125 °C, a stable length is registered during the first 10 s before expansion. In the case of quenching to 150 °C, a slight contraction during the first 20 s is observed before expansion.

In the case of alloy HMn, martensite starts forming at 150 °C (Ms1), leading to different fractions of martensite ranging from 0.68 to 0.07 as a function of the quenching temperatures. Fresh martensite formed during the last quenching step in specimens quenched to 75 °C (Ms2 = 30 °C), 100 °C (Ms2 = 68 °C), and 125 °C (Ms2 = 100 °C), as shown in **Figure 3.5(d)**. When the final quench is down to -120 °C, the fresh martensite is also observed after quenching to 25 °C and 50 °C, and the Ms2 is -60 °C and -12 °C, respectively. As displayed in **Figure 3.5(e)**, similar to LMn alloy, no phase transformation is observed during the reheating stage. All specimens exhibit continuous expansion during the partitioning process, as shown in **Figure 3.5(f)**. The expansion is in all cases of an extent of less than 0.03%, which can be associated to the homogenisation of thermal gradients and the process of carbon partitioning. This expansion has been reported in some publications [4,9,11,29,32] in which similar graphs are shown.

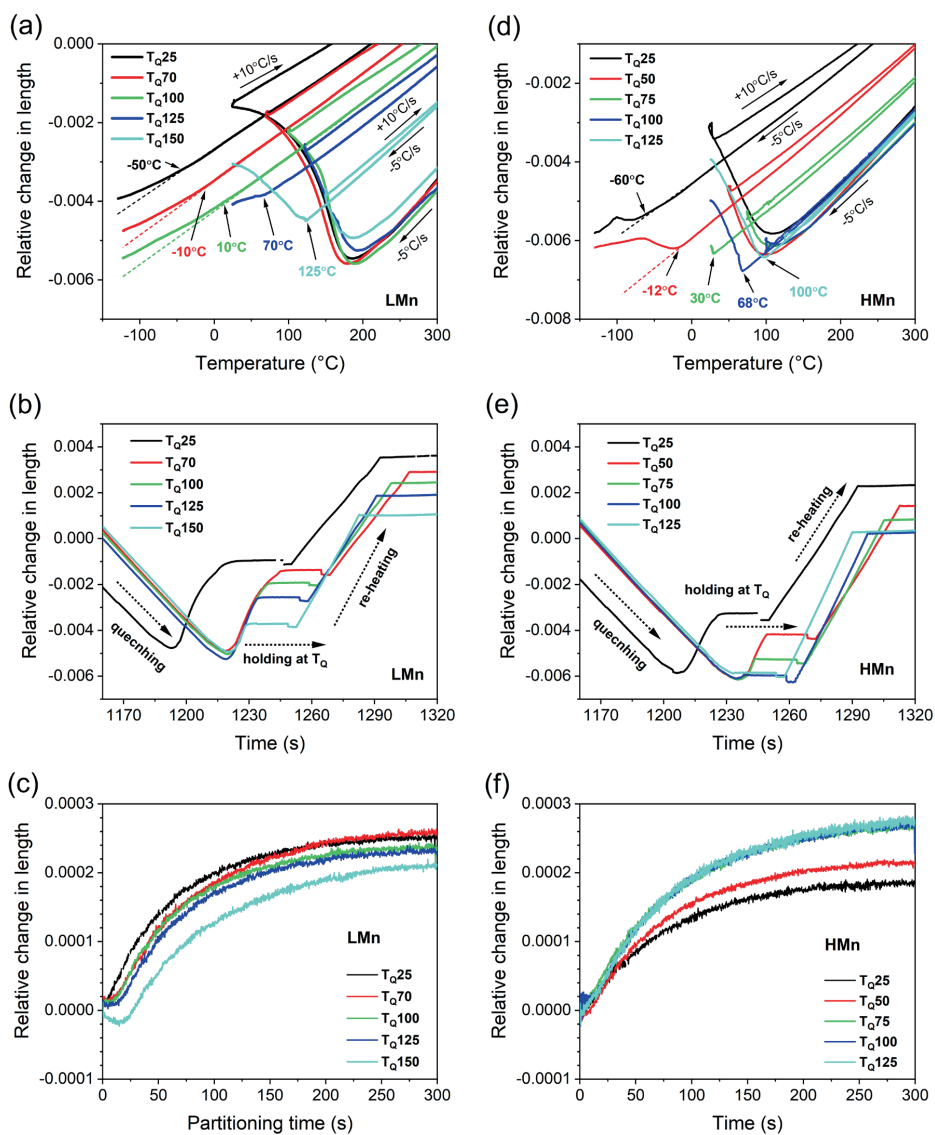


**Figure 3.5.** Relative change in length versus temperature during Q&P experiments, versus time during the quenching step followed by reheating, and versus partitioning time during the partitioning step for alloys (a-c) LMn and (d-f) HMn.

### 3.4.2 Phase Fractions

**Figure 3.6** (a) and (b) shows the phase fraction after each Q&P treatment for both alloys. The volume fraction of retained austenite is measured by XRD as shown in (c) and (d), while the fraction of martensite formed during the quenching step (in the following, M1) is obtained by the lever rule (see

**Figure 3.3).** The fraction of fresh martensite formed during the last quenching step (in the following, M2) is calculated by phase balance, assuming no transformation of M1. As we can see, some M2 (typically a fraction below 0.08) is obtained by phase balance in specimens in which no expansion is observed during the last quench (to room temperature). Considering the measurement limitation of  $\pm 0.02$  error for both primary martensite and retained austenite fractions, the fresh martensite will have  $\pm 0.04$  error bar to the calculated values. In the dilatometer, such a small amount of fresh martensite cannot be obtained with sufficient accuracy.

As shown in **Figure 3.6 (c)**, the XRD spectrum for LMn alloy only shows martensite (peaks marked by red index) and austenite (peaks marked by blue index) for all treated specimens. With increasing quenching temperature, martensite peaks gradually become less symmetric and tend to move to low angles, indicating an increasing presence of fresh martensite (M2). This is further visible in the insert of **Figure 3.6 (c)**, which shows the evolution of the {002} peak of martensite with increasing quenching temperature. Peak splitting occurs when the carbon content of steel is higher than the threshold of about 0.2 wt.%, often quoted as the minimum carbon level required for a detectable martensite tetragonality [36]. HMn specimens, **Figure 3.6 (d)**, displays the same martensite and austenite peaks as LMn alloy. Peak splitting is also observed in martensite in this material for quenching temperatures equal to 75 °C and higher.

As shown in **Figure 3.6 (a)**, in alloy LMn, the fraction of retained austenite increases from 0.11 after quenching to room temperature to 0.29 after quenching to 125 °C when fractions of fresh martensite higher than 0.14 are observed. At higher quenching temperatures, the fraction of retained austenite does not increase further, although more fresh martensite is formed. A similar trend is observed in alloy HMn as shown in **Figure 3.6 (b)**, but higher fractions of retained austenite are stabilised. The fraction of retained austenite remains approximately constant (0.35 - 0.38) within measurement error for quenching temperatures between 50 °C and 100 °C, while the fractions of primary and fresh martensite clearly change in the same range. The fraction of retained austenite is reduced to 0.32 and 0.22 at room temperature and 125 °C, respectively.

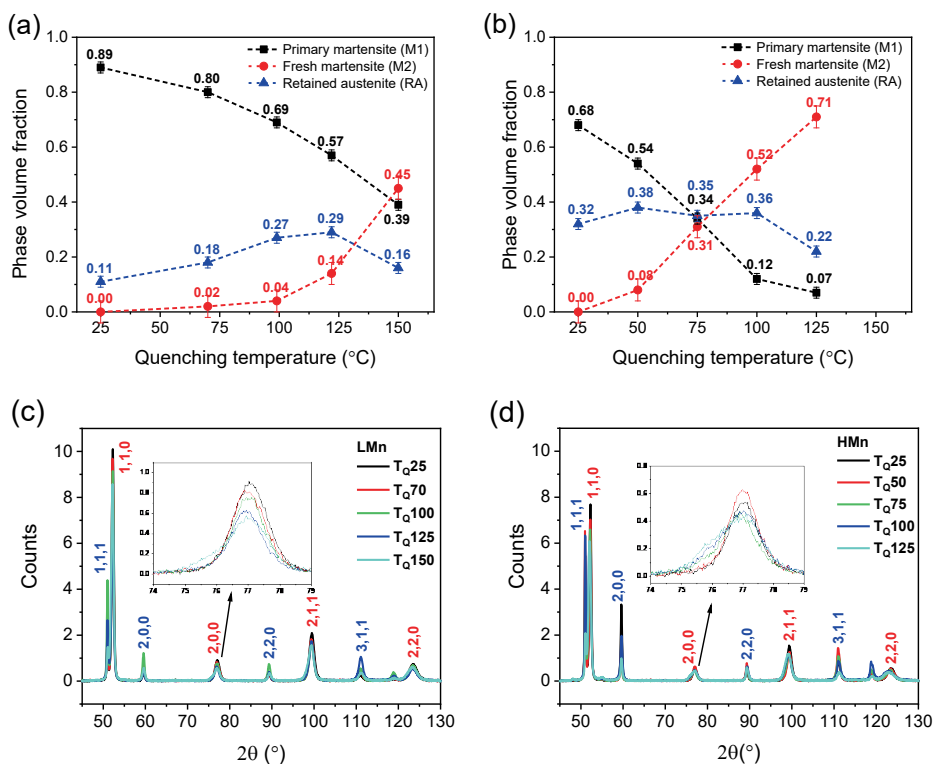


Figure 3.6. Phase volume fraction (a)(b) and XRD patterns (c)(d) in Q&P specimens of LMn alloy and HMn alloy, respectively.

### 3.4.3 Microstructure Characterisation

#### • LMn alloy

Figure 3.7 shows optical micrographs of alloy LMn specimens after different Q&P treatments. Specimens show heterogeneous microstructures, probably due to chemical segregation. The etching surface shows two distinct regions, an alternation between the less-etched bright bands and dark etched bands. According to the working mechanism of Vilella etchant, the dark features should correspond to the carbon-depleted martensite, while the bright bands contain retained austenite, probably adjacent to carbon-rich martensite.

The etched microstructural bands show a stronger contrast for lower fractions of primary martensite. This can be seen by comparing Figure 3.7 (a) for the specimen quenched to 70 °C with  $f_{M1} = 0.80$ , Figure 3.7 (b) for the specimen quenched to 125 °C with  $f_{M1} = 0.57$  and Figure 3.7 (c) for the specimen quenched to 150 °C with  $f_{M1} = 0.39$ , which also corresponds with an increased carbon depletion of the

primary martensite. Unfortunately, LOM images do not allow for a distinction between RA and fresh martensite (M2). This is mainly due to two reasons: (a) the higher carbon content in M2 enhances its etching resistance, leading to similar etching features as RA, and (b) etching features are further shaded by the strong contrast of M1 when M1 is volume dominant in the microstructures.

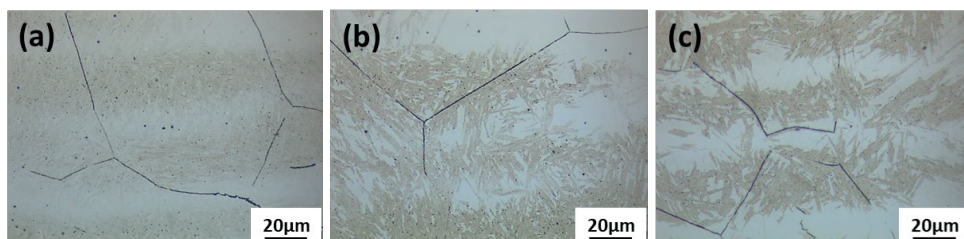


**Figure 3.7.** LOM images of LMn Q&P specimens with decreasing volume fraction of M1: (a) Specimen quenched to 70 °C, (b) Specimen quenched to 125 °C, (c) Specimen quenched to 150 °C.

**Figure 3.8** shows SEM micrographs of the same specimens displayed in **Figure 3.7**. The carbon-depleted M1 bands now have a brighter contrast under the SEM. **Figure 3.8** (a) shows selective dissolution (etching) on localised regions in the specimen quenched to 70 °C. The M1-rich bands show more of this localised etching uniformly distributed on the surface. Some discontinuous precipitates are observed at prior austenite grain boundaries. **Figure 3.8** (b) presents the microstructure of the specimen quenched to 125 °C, showing that depletion of M1 leads to more etched M1-rich bands and smoother RA-rich bands. In the specimen quenched to 150 °C in **Figure 3.8**(c), more precipitates are observed inside the carbon-depleted M1, which suffered a heavier attack by the etchant.

Two types of precipitates can be observed at the etched locations: a) small particles located inside M1, probably carbides, and b) lamellar precipitates at prior austenite grain boundaries. The visibility of small particles depends on the Q&P specimens (more frequent in specimens with a higher fraction of M1), while the grain boundary precipitates do not show any specific relationship with the specimen or location.

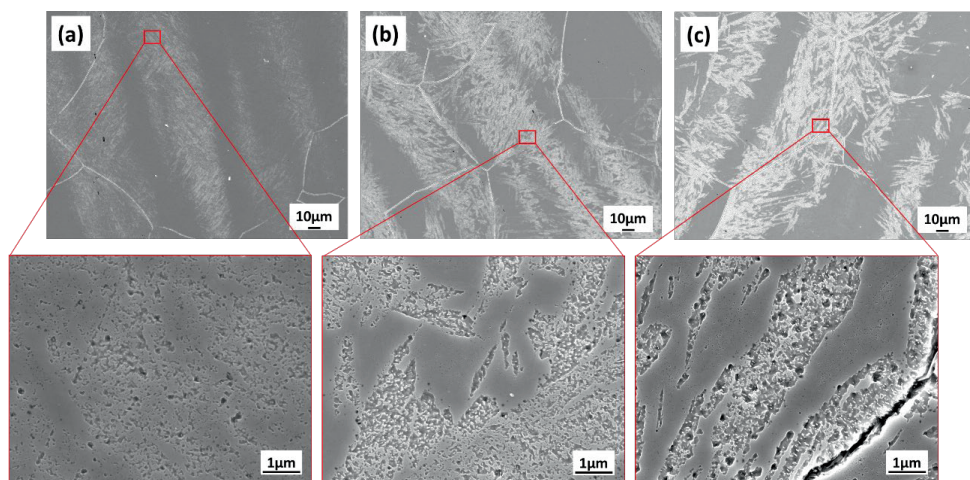


**Figure 3.8. SEM micrographs of LMn Q&P specimens with decreasing volume fraction of M1: (a) Specimen quenched to 70 °C, (b) Specimen quenched to 125 °C, (c) Specimen quenched to 150 °C.**

- **HMn alloy**

The light optical micrographs of alloy HMn also exhibit banded microstructures, as shown in **Figure 3.9**. In this case, there are three kinds of etching features: bright bands (corresponding to locations of higher carbon concentration), dark bands (corresponding to locations with carbon depletion), and bands with an intermediate contrast, such as the ones shown in **Figure 3.9** (c). In light of the phase fraction measurements conducted in the preceding sections, it can be inferred that the bands exhibiting intermediate contrast are likely indicating the presence of fresh martensite, characterised by a higher carbon concentration than primary martensite.

For quenching temperatures in which the final microstructures contain only dark and bright etching features, as shown in **Figure 3.9** (a) for the specimen quenched to 75 °C, LOM reveals a banded morphology similar to the one observed in the LMn specimen quenched to 125 °C, but with higher contrast. Within the dark M1 band, some white blocky MA islands remain unetched.

The specimen quenched to 100 °C led to a low fraction of M1 (0.12), which is only observed along prior austenite grain boundaries. As can be seen from **Figure 3.9** (b), RA is a major phase, which is confirmed with XRD measurements. Fresh martensite (M2) appeared as grey traces, tending to form bands. **Figure 3.9** (c) shows the microstructure of the specimen quenched to 125 °C. The increased fraction of fresh martensite is shown as significantly thicker grey bands. With a fraction of M1 close to zero, the dark etching features are only observed along prior austenite grain boundaries.

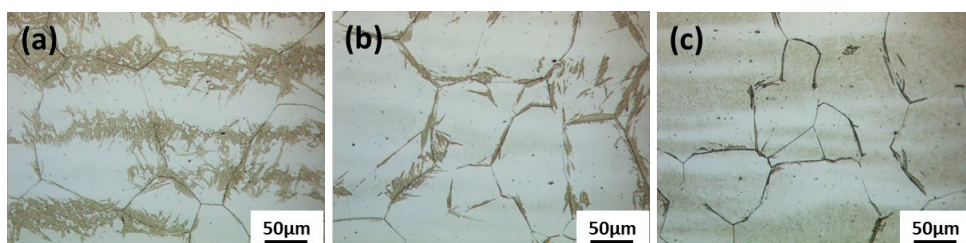


**Figure 3.9.** LOM images of HMn Q&P specimen with increasing volume fraction of M2: (a) Specimen quenched to 75 °C, (b) Specimen quenched to 100 °C, (c) Specimen quenched to 125 °C.

SEM micrographs in **Figure 3.10** further exhibit the different etching features of M1 and M2 and also reveal the different morphologies of small particles and grain boundary precipitates observed in LMn. M1 bands are deeply etched and full of small particles (probably carbides). M2 is shown as a slightly etched coarse surface, which cannot be clearly separated from RA.

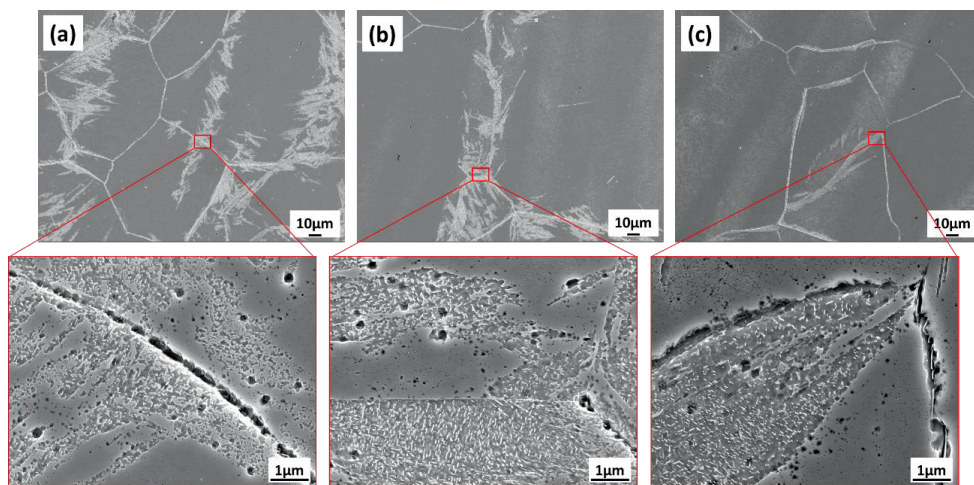


**Figure 3.10.** SEM images of HMn Q&P specimens with decreasing volume fraction of M1: (a) Specimen quenched to 75 °C, (b) Specimen quenched to 100 °C, (c) Specimen quenched to 125 °C.

#### 3.4.4 Grain Boundary Microstructure

As observed in previous LOM and SEM microstructures, there are precipitates located at the prior austenite grain boundaries and small particles in M1-rich bands (**Figure 3.8** and **Figure 3.10**). To understand the precipitation behaviour, the quenched microstructures before partitioning are displayed in **Figure 3.11**. The prior austenite grain boundaries contain some precipitates. But no small particles are observed inside the grains, suggesting that small particles inside grains distributed on M1-rich bands (**Figure 3.8** and **Figure 3.10**) are formed in the partitioning stage. The grain boundary precipitates exhibit a similar morphology to  $M_{23}C_6$ -type chromium carbides commonly found in stainless steels, as

reported in the literature (see [39] for example). Thus, the precipitates at prior austenite grain boundaries are most probably  $\text{Cr}_{23}\text{C}_6$  formed before partitioning.

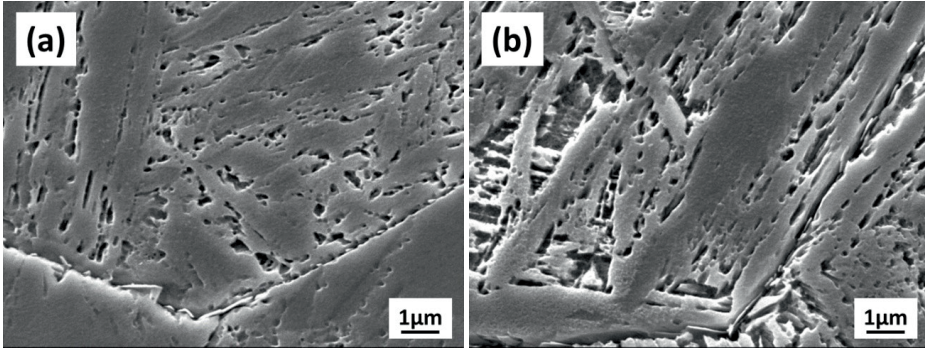


**Figure 3.11. Microstructures observed with SEM of (a) LMn and (b) HMn alloys quenched to room temperature without partitioning processing.**

### 3.5 Discussion

#### 3.5.1 Microstructural Evolution During Q&P Treatments

To better understand the microstructural evolution during the application of the Q&P treatments, experimental results are compared with theoretical outcomes from the CCE model. Assuming that the partitioning process leads to full carbon partitioning from primary martensite into austenite, in the absence of interface migration or competing processes such as carbide precipitation, the balance of carbon at the end of the partitioning process and before the final quench is [3]:

$$f_A \cdot X_C^{A(CCE)} + f_{M1} \cdot X_C^{M1(CCE)} = X_C^{alloy} \quad (3-3)$$

Where  $f_A$ ,  $f_{M1}$ ,  $X_C^{A(CCE)}$ ,  $X_C^{M1(CCE)}$  are the volume fractions and carbon contents of austenite and primary martensite, respectively, at the end of the partitioning step and  $X_C^{alloy}$  is the nominal carbon content of the alloy. Particularly,  $X_C^{A(CCE)}$  refers to the carbon in austenite at the end of the partitioning step and assuming full carbon partitioning. For every quenching temperature investigated, the volume fraction of martensite  $f_{M1}$  (i.e. the fraction of primary martensite) at the partitioning stage has been determined through dilatometry, while the fraction of austenite at the partitioning stage is thereby  $(1 - f_{M1})$ . The  $f_{M1}$  fractions are shown in **Figure 3.6**.

It follows that the theoretical carbon concentration in austenite  $X_C^{A(CCE)}$  at the end of the partitioning step, assuming full carbon partitioning and in the absence of competing reactions, can be obtained from **Equation (3-3)** as:

$$X_C^{A(CCE)} = X_C^{alloy} / (1 - f_{M1}) \quad (3-4)$$

The carbon content of austenite at the end of the partitioning step is related to the stability of this phase upon further quench. Therefore, if austenite is sufficiently enriched in carbon, it remains retained at room temperature. However, if carbon enrichment is not sufficiently high, part (or all) of this austenite will transform into fresh martensite (M2). The observation of an additional Ms on quenching after the partitioning step can be associated to the carbon content of the austenite at the end of the partitioning step. The carbon concentration in the austenite at the end of the partitioning step can be calculated from the experimental Ms2 temperatures shown in **Figure 3.5** using **Equation (3-5)** (equation 2-1 in **Chapter 2**) developed based on experimental data from references [18-21, 32, 36]. Note that **Equation (3-5)** does not account for the influence of prior austenite grain size (PAGS), austenite grain size or austenite grain morphology on the Ms temperature. Our PAGS measurements, conducted using LOM images, on both alloys showed results within a similar range of  $103 \pm 43 \mu\text{m}$ . Consequently, we anticipate that there will not be significant error attributable to PAGS when estimating the Ms temperature.

$$M_{s2} = 553.7 - 530.8X_C^Y - 9.7X_{Si}^Y - 12.1X_{Cr}^Y - 30.4X_{Mn}^Y \quad (3-5)$$

where  $M_{s2}$  is the fresh martensite transformation start temperature and  $X_i^Y$  indicates the concentration of element “i” in the austenite, in wt.%.

**Figure 3.12** compares the carbon concentration of retained austenite experimentally obtained with that calculated with **Equation (3-5)** for both alloys. The agreement between the carbon content in austenite calculated assuming CCE conditions ( $X_C^{A(CCE)}$ ) and experimentally estimated from Ms2 ( $X_C^{RA}$ ) is significant, although there is a consistent overestimation of the CCE-based values. This overestimation indicates the presence of carbides precipitation during the application of the Q&P process that is not considered in the CCE model.

For the case of alloy LMn (**Figure 3.12(a)**), the CCE-based values of carbon content in austenite at the end of the partitioning step are higher than the estimated from Ms2 for the investigated conditions, which indicates the presence of competing reactions consuming carbon that does not reach the austenite during partitioning. This indicates that the precipitation of carbides in the primary martensite through tempering play a strong role as a reaction competing for the carbon available for partitioning. Indeed, carbides are clearly observed in microstructures quenched to  $125^\circ\text{C}$  ( $f_{M1} = 0.57$ ) (**Figure 3.8**), corresponding to an increasing fraction of M1.

For the case of alloy HMn, shown in **Figure 3.12(b)**, the CCE model meets well the experimental results when the martensite volume fraction is less than 0.54, i.e. quenching temperature equals to or

higher than 50 °C. When the quenching temperature is lower, the gap between experimental and calculated carbon in austenite is higher for the maximum fraction of M1 studied, which is 0.68 (quenching temperature of 25 °C). Interestingly, in alloy LMn for a similar fraction of M1 (0.69), the gap between experimental and CCE-based carbon in retained austenite remains of the same order as in alloy HMn.

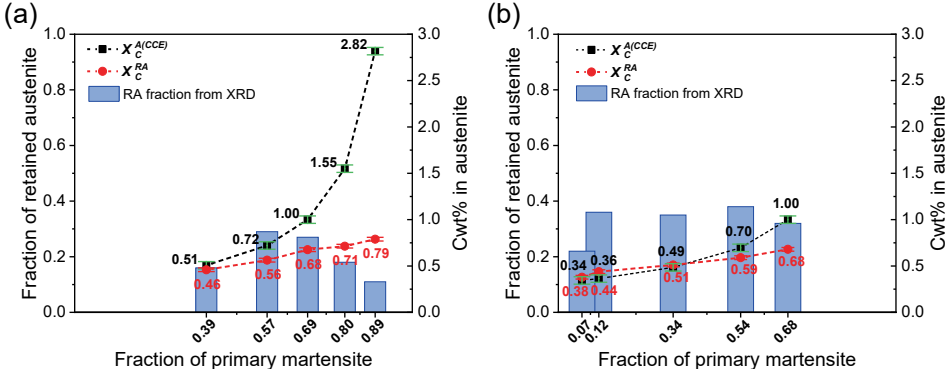


**Figure 3.12. Volume fraction and carbon content of retained austenite versus volume fraction of M1 for (a) LMn alloy, (b) HMn alloy (carbon content from Ms2 with error bar  $\pm 0.02$  wt.%, carbon content from CCE, with error bar  $\pm 0.04$  wt.%).**

In the following, the carbon content associated to the gap between the carbon in austenite based on CCE and the carbon estimated from Ms2 temperatures is evaluated. The missing carbon associated to competing reactions is now assumed to be in the form of carbides or segregated within M1. Now, **Equation (3-6)** takes into account the carbon balance in the material at room temperature (and not at the partitioning step, as it is the case in **Equation (3-3)**):

$$f_A \cdot X_C^{A(CCE)} - f_A \cdot X_C^{RA} = f_{M1} \cdot X_C^{M1} \quad (3-6)$$

Where  $f_{M1} \cdot X_C^{M1}$  represents the total carbon that does not participate in the process of carbon partitioning to austenite, and it is assumed to remain in the primary martensite. This approach ignores the possibility of carbide precipitation in the retained austenite. In this case,  $X_C^{RA}$  refers to the experimentally measured carbon content in retained austenite (from Ms2), which is seen as equal to  $X_C^{M2}$ . Applying **Equation (3-6)**,  $f_{M1} \cdot X_C^{M1}$  can be calculated. Results are displayed in **Figure 3.13** for both alloys.

**Figure 3.13 (a)** shows the total carbon content in primary martensite (product  $f_{M1} \cdot X_C^{M1}$ ) versus the volume fraction of primary martensite. In all the investigated cases, the carbon content in M1 is lower than the alloy's carbon concentration and also lower than that in retained austenite shown in

**Figure 3.12.** With the primary martensite fraction increasing from 0.34, the carbon trapped in martensite also increased, indicating increased carbide precipitation.

The carbon concentration in primary martensite (in **Figure 3.13(b)**) also increases with the increasing fraction of M1 in both alloys. In the LMn alloy, the carbon concentration increases from 0.08 wt.% to 0.25 wt.% compared with the 0.31 wt.% in the alloy. For the case of HMn alloy, carbon increased from 0 wt.% to 0.15 wt.%, compared to 0.32 wt.% in the alloy. It seems that, the higher the fraction of M1, the higher the density of carbides, which may be associated to a net reduction of martensite/austenite interfaces [17].

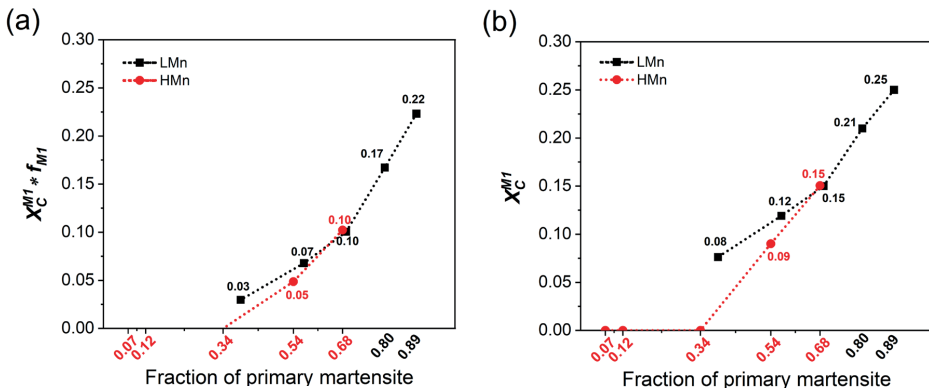


**Figure 3.13. (a) Total carbon content in primary martensite and (b) Carbon concentration in primary martensite versus primary martensite fraction of both alloys.**

The carbon concentration converted from Ms2 temperature is then compared to the XRD results calculated using two empirical formulas (3-1)[36] and (3-2)[37]. It can be seen from **Figure 3.14**, that the carbon concentration converted from Ms2 temperature falls in the range between the outcomes of **Equation (3-1)** and **Equation (3-2)**. **Equation (3-2)** predicts much higher carbon content than **Equation (3-1)** for both alloys. In most cases, when the primary martensite fraction is less than 0.70, **Equation (3-2)** predicts higher carbon concentration than expected according to the CCE model, implying a carbon content higher than the carbon present in the alloy. On the contrary, **Equation (3-1)** predicts concentrations of carbon lower than the ones estimated from the Ms2 temperature in several of the investigated conditions, which implies that retained austenite has lower carbon than fresh martensite. Therefore, both equations led to invalid results in the investigated materials.

De Cooman et al. [36] have compared both equations and declared that **Equation (3-1)** is more reasonable for Q&P stainless steels as it does not exceed the CCE model. Although this is also applicable for our case, **Equation (3-1)** provides unrealistically low values. The problems associated to

**Equations (3-1) and (3-2)** may be associated to the range of applicability of these equations when they are proposed and further investigation is needed.

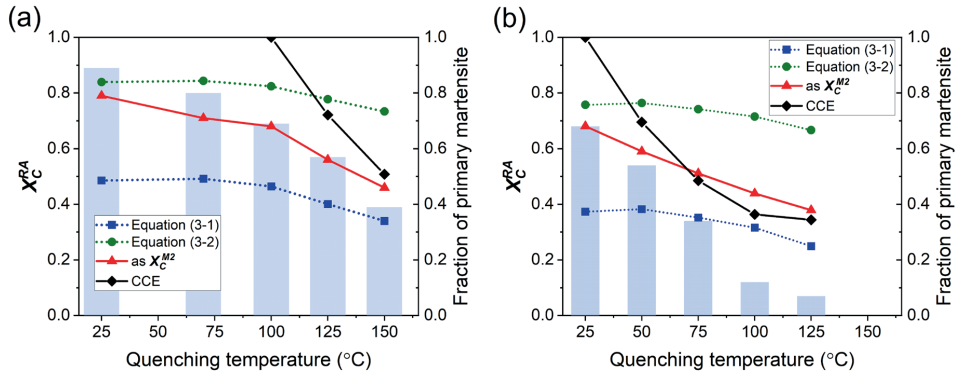


**Figure 3.14.** Comparison of carbon concentration in RA obtained by calculations and experiments in both LMn and HMn alloys. (carbon content from Ms2 with error bar  $\pm 0.02$  wt.%, carbon content from CCE, with error bar  $\pm 0.04$  wt.%).

As discussed, the presence of carbide precipitation in M1 has been deduced from the carbon balances. SEM images in **Figure 3.8** and **Figure 3.10** showed carbides with two different morphologies, intragranular carbides and grain boundary precipitates.  $M_{23}C_6$  precipitates at room temperature are suspected in **Figure 3.11**, the quenched microstructure before partitioning. Similar research results are obtained in Q&P treated ferritic stainless steels [40].

The presence of Cr-carbides at prior austenite grain boundaries leads to carbon depletion in their surroundings, which implies a local increase in the Ms temperature at these sites. This explains the formation of martensite only at prior austenite grains shown in **Figure 3.9** for the specimen HMn quenched to 125 °C, where only 0.07 volume fraction of M1 transformed, all at grain boundaries.

### 3.5.2 Martensitic Transformation Kinetics

The Koistinen-Marburger equation [8] (in the following, K-M equation) is a general equation describing the progress of transformation from austenite to martensite in steels. During cooling, the austenite-to-martensite transformation begins at a certain temperature designated as the Ms temperature and proceeds only upon continuous cooling below this temperature. The K-M equation describes the formation of martensite as a function of the undercooling as follows:

$$f_{M1} = 1 - \exp [-\alpha_m \cdot (T_{KM} - T)] \quad (3-7)$$

Where  $T_{KM}$  is the K-M martensite start temperature, which is, in general, reportedly lower than the experimentally measured Ms temperatures (see, for example, ref [41, 42]).  $T$  represents any temperature

below the  $T_{KM}$  at which martensite forms and  $\alpha_m$  is a rate parameter that can be calculated based on the chemical composition using the empirical **Equation (3-8)** proposed by van Bohemen [43]:

$$\alpha_m = 0.0224 - 0.0107w_C - 0.0007w_{Mn} - 0.00005w_{Ni} - 0.00012w_{Cr} - 0.0001w_{Mo} \quad (3-8)$$

The application of the K-M equation to the present steels leads to the results plotted in **Figure 3.15**, represented together with experimental results from the application of the Lever rule in **Figure 3.3**. The experimental Ms temperatures have been employed as “ $T_{KM}$ ” temperatures, which in general, are considered to be a good first approach. As can be seen, the theoretically deduced martensite kinetics does not fit the experimental results. Not only is the  $T_{KM}$  overestimated by using the Ms temperature (as expected), but also the transformation rate  $\alpha_m$  is overestimated by **Equation (3-8)**.

To understand the reasons for these deviations, the  $T_{KM}$  and  $\alpha_m$  parameters are fitted based on the experimental results, as shown in **Figure 3.15**. Now, the K-M model fits experimental results well in most parts. However, the early stages of martensite transformation cannot be adequately predicted. The deviation between the experimental kinetics and the K-M fit measured as Ms -  $T_{KM}$  is of 43 °C in LMn alloy and 47 °C in HMn alloy. This reveals that the formation of the martensite fraction corresponding to  $T_{KM}$  temperature (approximately 0.10 for both alloys) takes place at a larger temperature interval on cooling than predicted by the K-M model [44]. This effect is known as the “slow-start” phenomenon, and it is attributed to the dispersion of Ms temperatures arising from local chemical inhomogeneities [45]. This means that also, in the present steels, chemical segregation is playing a role in the development of the microstructures during the quenching step, with effects on the partitioning step, as is evaluated in the following section.

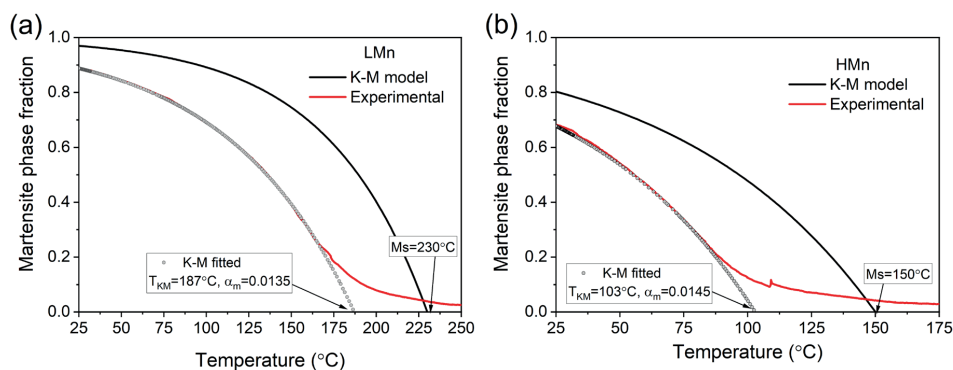


**Figure 3.15.** Martensite transformation kinetics built from the K-M model and lever rule for both alloys.

### 3.5.3 Influence of Elemental Segregation on Microstructures

The application of the K-M model to the martensite kinetics has shown that elemental segregation is affecting the microstructure development in the present steels. That is expected from optical

microscopy in **Figures 3.7** and **3.9**. Chemical segregation originates from casting and solidification process and can only be eliminated through very long annealing treatments that are often not industrially feasible [29].

To further understand the effect of chemical segregation on the microstructure development, local EPMA line measurements perpendicular to the observed bands are performed on alloys LMn and HMn at the quenched state. Results are shown in **Figure 3.16** and **Table 3.2**. **Figure 3.16** (a) and (b) show the elemental profile of alloys quenched to room temperature ( $T_Q = 25$ ) before partitioning. Here only the segregating elements are displayed. Particularly, LMn alloy is displayed together with an etched optical microstructure to assist in understanding the correspondence between etching morphology and segregations.

As marked in **Figure 3.16** (a), dark bands correspond to an area with lower C, Cr and Mn content, while the brighter bands correspond to higher C, Cr and Mn content; this explains why we observed different bands in optical microscopy. For both alloys, the amplitude of the segregation varies per alloying element. The average chemical composition measured by EPMA is summarised in **Table 3.2**, together with the segregation peaks in concentration converted to a percentage for both alloys. Compared with the alloy's composition in **Table 3.1**, the measurement of carbon shows the highest deviations. The average content of Cr and Mn is also higher than the general composition, and the segregation (as indicated in **Figure 3.16** (c) and (d)) is more significant in HMn than that in LMn.

In **Equation (3-5)** and **Figure 3.14**, Cr and Mn are regarded as global concentrations without considering segregation. **Table 3.2** reveals that it is important to account for the influence of chemical segregation of Cr and Mn. The assessment conducted in this context reveals a maximum carbon content difference of 0.05 wt.% (with an error bar of  $\pm 0.025$  wt.%) between the alloy-rich and alloy-poor bands. Note that such a small margin of error does not have a significant impact on the conclusions drawn in the previous section.

**Table 3.2. Chemical segregation and Ms temperature in alloying- rich and -poor bands (% is relative percentage).**

Segregation	C		Cr		Mn		Ms (°C)	
LMn	0.30 wt.%	+ 13.3% - 6.7%	13.5 wt.%	+ 5.9% - 3.7%	0.8 wt.%	+ 12.5% - 12.5%	205	- 35 + 15
HMn	0.45 wt.%	+ 13.3% - 20.0%	14.0 wt.%	+ 1.4% - 3.6%	3.3 wt.%	+ 3.0% - 6.0%	42	- 30 + 60

**Figures 3.16 (c) and (d)** are local Ms temperatures that calculated using **Equation (3-5)** according to the composition shown in **Figures 3.16 (a) and (b)**, respectively. The dash lines in both local Ms graphs represent the Ms temperature of the averaged local compositions. The Ms corresponding to the highest and lowest segregation compositions in each graph are also summarised in **Table 3.2**.

**Figure 3.16 (c)** shows the effect of the changes in composition on the local Ms temperatures across the different bands in alloy LMn. Results indicate significant variations in the local Ms temperatures. Particularly, variations in carbon content seem to be the most relevant in the determination of local Ms temperatures, as can also be seen from **Equation (3-5)**. Compared to the Ms calculated based on averaged local composition, the local Ms varies from -35 °C to + 15°C from the alloy-rich locations to the alloy-poor locations. These variations further influence the martensite transformation, leading to a higher presence of primary martensite in alloy-poor bands than in alloy-rich bands.

For the case of alloy HMn, as shown in **Figure 3.16 (d)**, the segregating elements contribute to a 30 °C lower Ms in the alloying-rich band and 60 °C higher Ms in alloying-poor bands with respect to the average Ms corresponding to that local measurement.

Carbon is therefore the most influential element, followed by Mn and Cr. The equation used to calculate Ms (**Equation (3-5)**) quantifies the effect of these elements on the scatter of Ms.

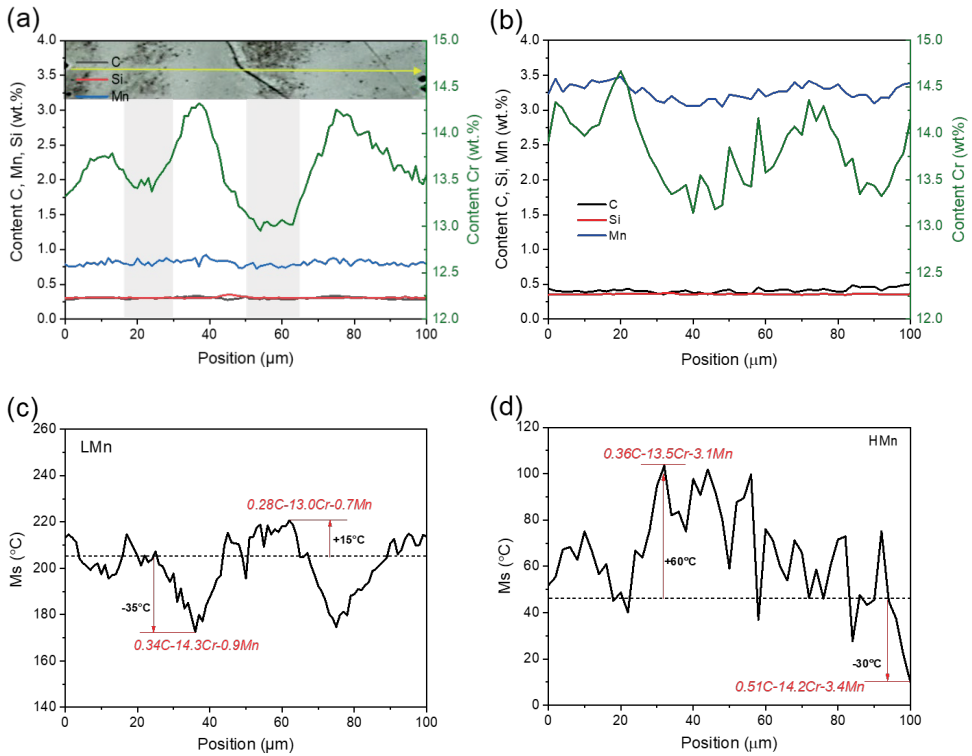


**Figure 3.16.** (a-b) Elemental profiles in two regions of both alloys after quenching to room temperature ( $T_Q = 25$ ) and before partitioning, and (c-d) local Ms temperatures calculated based on the local elemental profiles (a)(c) LMn alloy and (b)(d) HMn alloy.

As discussed above, chemical segregation leads to alloying-rich and alloying-poor bands characterised by different Ms temperatures. Therefore, martensite formation kinetics is different among bands. To assess the differences in the martensite formation kinetics in different bands and its influence on the experimentally measured martensite formation kinetics, the K-M model is used as follows. The scatter data of Ms temperature in **Table 3.2** is considered as scatter for  $T_{KM}$  at different bands, leading to  $\pm 25^\circ\text{C}$  for alloy LMn and  $\pm 45^\circ\text{C}$  for alloy HMn. The  $\alpha_m$  parameter fluctuates with local compositions in the range of  $\pm 0.0005$  among bands, which leads to a minor effect on the calculations. Thus, for the  $\alpha_m$  parameter at different bands, we use the same value that is fitted from **Figure 3.15**, that is, 0.0135 for alloy LMn and 0.0145 for alloy HMn. The kinetics of martensite formation is then calculated at different bands leading to the results shown in **Figure 3.17**.

During cooling below the Ms temperature, the formation of martensite starts in alloy-poor bands in alloy LMn. When alloy-rich bands start forming martensite, there is already more than 40% martensite on alloy-poor bands. For alloy HMn, martensite starts forming on the alloy-poor band as

well. But the phase transformation will differ significantly in alloy-rich bands due to a 90 °C lower martensite transformation temperature. For example, alloy-rich bands will contain 0.60 (volume fraction) less martensite than alloy-poor bands when quenched to 68 °C. The  $T_{KM}$  temperatures of the alloy-poor band are closer or identical to the experimental measured Ms temperatures in both alloys.

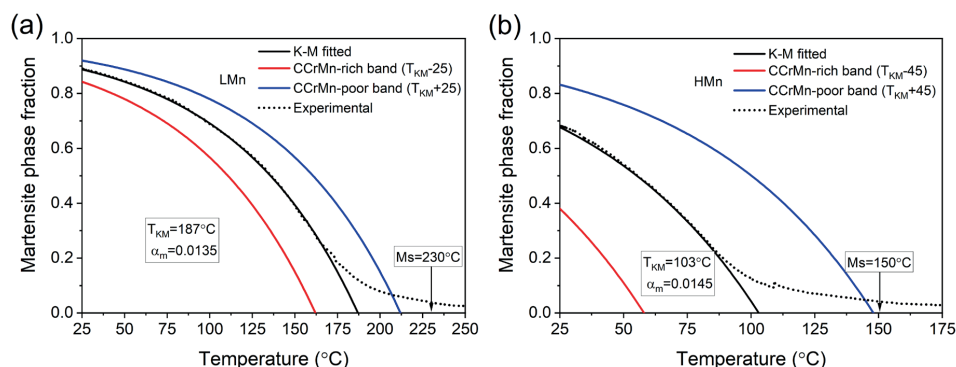


**Figure 3.17. Martensite transformation kinetics at segregation bands of (a) LMn alloy, (b) HMn alloy.**

EPMA measurements are local; therefore, over the entire surface, there might be locations with a bit higher or a bit lower alloy content than measured. Nevertheless, the local martensite transformation kinetics can be established by fitting the K-M model with local elemental composition and Ms temperatures.

Different phase transformations in different bands lead to primary martensite-rich structures in alloy-poor bands and primary martensite-poor structures in alloy-rich bands. After partitioning, the primary martensite-rich band will contain more carbides precipitation, showing as dark etching bands, as revealed by **Figures 3.7 – 3.10**. While the primary martensite-poor band will stabilise less retained austenite, causing fresh martensite transformation, showing as grey etching bands, as revealed in **Figure 3.9**.

### 3.6 Conclusions

We investigated the microstructure evolution of Q&P treated martensitic stainless steels, with special attention to the applicability of the CCE model and martensitic transformation kinetics with the existence of heterogeneous microstructure. The main conclusions are summarised as follows.

- Phase fractions of primary martensite, retained austenite and fresh martensite are evaluated based on dilatometry and X-ray diffraction measurement, leading to consistent dependencies with Q&P heat treatment parameters. The carbon content in austenite at the partitioning temperature is best estimated based on the experimental measurement of the martensite start

temperature corresponding to fresh martensite, which can be determined using sub-zero quench treatments in the dilatometer. Calculations of carbon in retained austenite based on measurements of the lattice parameter using two different equations often used in the literature lead to invalid results in the present alloys.

- The carbon concentration in austenite after the partitioning step calculated assuming full carbon partitioning from martensite to austenite overestimates the actual carbon enrichment observed in austenite. This is due to the precipitation of carbides, including precipitates at prior austenite grain boundaries that formed during the first quenching and small particles inside tempered martensite grains that formed during partitioning. These precipitates consume carbon that is no longer available to partition into austenite.
- The general Koistinen-Marburger parameters is fitted according to the experimental results of martensite kinetics, assisted by local EPMA analysis. It is found that martensite transformation kinetics at alloy-poor and alloy-rich bands differ. The “slow-start” phenomenon is confirmed and explained based on chemical segregation.
- The increasing addition of Mn and its chemical segregation leads to a larger heterogeneity of carbon in alloy HMn. This further leads to a larger Ms temperature scatter between bands in the microstructure of alloy HMn (scatter of 90 °C) compared to alloy LMn (scatter of 50 °C).

## References

- [1] J.G. Speer, A.M. Streicher, D.K. Matlock, F. Rizzo, G. Krauss, Quenching and partitioning: a fundamentally new process to create high strength trip sheet microstructures. *The Iron & Steel Society*, (2003) 505–522.
- [2] J.G. Speer, D.K. Matlock, B.C. De Cooman, J.G. Schroth, Carbon partitioning into austenite after martensite transformation. *Acta Materialia*, 51 (2003) 2611–2622. [http://dx.doi.org/10.1016/S1359-6454\(03\)00059-4](http://dx.doi.org/10.1016/S1359-6454(03)00059-4)
- [3] J.G. Speer, F. Rizzo, D.K. Matlock, D.V. Edmonds, The “quenching and partitioning” process: background and recent progress. *Materials Research*, 8 (2005) 417–423. <http://dx.doi.org/10.1590/S1516-14392005000400010>
- [4] S. Ayenampudi, C. Celada-Casero, J. Sietsma, M.J. Santofimia, Microstructure evolution during high-temperature partitioning of a medium-Mn quenching and partitioning Steel. *Materialia*. 8 (2019) 100492. <https://doi.org/10.1016/j.mtla.2019.100492>
- [5] A.S. Nishikawa, M.J. Santofimia, J. Sietsma, H. Goldensteina, Influence of bainite reaction on the kinetics of carbon redistribution during the quenching and partitioning process. *Acta Materialia*, 142 (2018) 142–151. <https://doi.org/10.1016/j.actamat.2017.09.048>
- [6] A.S. Nishikawa, G. Miyamoto, T. Furuhashi, A.P. Tschiptschin, H. Goldenstein, Phase transformation mechanisms during quenching and partitioning of a ductile cast iron. *Acta Materialia*. 159 (2019) 1–16. <https://doi.org/10.1016/j.actamat.2019.08.001>
- [7] D. De Knijf, R. Petrov, C. Föjer, L.A.I. Kestens, Effect of fresh martensite on the stability of retained austenite in quenching and partitioning steel. *Materials Science and Engineering: A*, 615 (2014) 107–115. <https://doi.org/10.1016/j.msea.2014.07.054>
- [8] D.P. Koistinen, R.E. Marburger, A general equation prescribing the extent of the austenite-martensite transformation in pure iron-carbon alloys and plain carbon steels. *Acta Metallurgica*, 7 (1959) 59–60. [https://doi.org/10.1016/0001-6160\(59\)90170-1](https://doi.org/10.1016/0001-6160(59)90170-1)
- [9] S. Kumar, S. BratSingh, Evolution of microstructure during the "quenching and partitioning (Q&P)" treatment. *Materialia*, 18 (2021) 101135. <https://doi.org/10.1016/j.mtla.2021.101135>
- [10] J.Z. Zhang, Z.B. Dai, L.Y. Zeng, X. Zuo, J.F. Wan, Y.H. Rong, N.L. Chen, J. Lu, H. Chen, Revealing carbide precipitation effects and their mechanisms during quenching-partitioning-tempering of a high carbon steel: Experiments and Modeling. *Acta Materialia*, 217 (2021) 117176. <https://doi.org/10.1016/j.actamat.2021.117176>
- [11] S. Ebner, C. Suppan, A. Stark, R. Schnitzer, C. Hofer, Austenite decomposition and carbon partitioning during quenching and partitioning heat treatments studied via in-situ X-ray diffraction. *Materials & Design*, 178 (2019) 107862. <https://doi.org/10.1016/j.matdes.2019.107862>

- [12] P.F. Gao, J.H. Liang, W.J. Chen, F. Li, Z.Z. Zhao, Prediction and evaluation of optimum quenching temperature and microstructure in a 1300 MPa ultra-high-strength Q&P steel. *Journal of Iron and Steel Research International*, 29 (2022) 307–315. <http://dx.doi.org/10.1007/s42243-020-00535-5>
- [13] J.Y. Li, Y.B. Xu, B. Lu, Y.M. Yu, Y. Jing, W.H. Sun, Improvement of strength-ductility combination in ultra-high-strength medium-Mn Q&P steel by tailoring the characteristics of martensite/retained austenite constituents. *Journal of Materials Research and Technology*, 18 (2022) 352–369. <https://doi.org/10.1016/j.jmrt.2022.02.088>
- [14] F.M. Castro Cerda, E.I. Hernández, T. Ros-Yanez, R.H. Petrov, Isothermal phase transformations in a low carbon steel during single and two-step partitioning. *Metallurgical and Materials Transactions A*, 51 (2020) 1506–1518. <https://doi.org/10.1007/s11661-020-05643-1>
- [15] Y. Li, S. Chen, C.C. Wang, D.S. Martín, W. Xu, Modeling retained austenite in Q&P steels accounting for the bainitic transformation and correction of its mismatch on optimal conditions. *Acta Materialia*, 188 (2020) 528–538. <https://doi.org/10.1016/j.actamat.2020.02.033>
- [16] Z.B. Dai, R. Ding, Z.G. Yang, C. Zhang, H. Chen, Elucidating the effect of Mn partitioning on interface migration and carbon partitioning during Quenching and Partitioning of the Fe-C-Mn-Si steels: Modeling and experiment. *Acta Materialia*, 144 (2018) 666–678. <https://doi.org/10.1016/j.actamat.2017.11.025>
- [17] L. Yuan, D. Ponge, J. Wittig, P. Choi, J.A. Jiménez, D. Raabe, Nanoscale austenite reversion through partitioning, segregation and kinetic freezing: Example of a ductile 2 GPa Fe–Cr–C steel. *Acta Materialia*, 60 (2012) 2790–2804. <https://doi.org/10.1016/j.actamat.2012.01.045>
- [18] Q.L. Huang, C. Schröder, H. Biermann, O. Volkova, J. Mola, Influence of martensite fraction on tensile properties of Quenched and Partitioned (Q&P) martensitic stainless steels. *Steel Research International*, 87 (2016) 1082–1094. <https://doi.org/10.1002/srin.201500472>
- [19] T. Tsuchiyama, J. Tobata, T. Tao, N. Nakada, S. Takaki, Quenching and partitioning treatment of a low-carbon martensitic stainless Steel. *Materials Science and Engineering: A*, 532 (2012) 585–592. <https://doi.org/10.1016/j.msea.2011.10.125>
- [20] S.Y. Lu, K.F. Yao, Y.B. Chen, M.H. Wang, N. Chen, X.Y. Ge, Effect of quenching and partitioning on the microstructure evolution and electrochemical properties of a martensitic stainless steel. *Corrosion Science*, 103 (2016) 95–104. <https://doi.org/10.1016/j.corsci.2015.11.010>
- [21] J. Tobata, K.L. Ngo-Huynh, N. Nakada, T. Tsuchiyama, S. Takaki, Role of silicon in quenching and partitioning treatment of low-carbon martensitic stainless Steel. *ISIJ International*, 52 (2012) 1377–1382. <https://doi.org/10.2355/isijinternational.52.1377>
- [22] Z.B. Dai, H. Chen, R. Ding, Q. Lu, C. Zhang, Z.G. Yang, S. van der Zwaag, Fundamentals and application of solid-state phase transformations for advanced high strength steels containing metastable retained austenite. *Materials Science and Engineering: R: Reports*, 143 (2021) 100590. <https://doi.org/10.1016/j.mser.2020.100590>

- [23] B. Kim, J. Sietsma, M.J. Santofimia, The role of silicon in carbon partitioning processes in martensite/austenite microstructures. *Materials & Design*, 127 (2017) 336–345. <https://doi.org/10.1016/j.matdes.2017.04.080>
- [24] H. Bhadeshia, R. Honeycombe, *Steels: Microstructure and Properties*. Butterworth-Heinemann, 2017.
- [25] G. Krauss, Solidification, segregation, and banding in carbon and alloy steels. *Metallurgical and Materials Transactions B*, 34 (2003) 781–792. <https://doi.org/10.1007/s11663-003-0084-z>
- [26] F. HajyAkbari, J. Sietsma, G. Miyamoto, T. Furuhashi, M.J. Santofimia, Interaction of carbon partitioning, carbide precipitation and bainite formation during the Q&P process in a low C steel. *Acta Materialia*, 104 (2016) 72–83. <https://doi.org/10.1016/j.actamat.2015.11.032>
- [27] F. HajyAkbari, J. Sietsma, R.H. Petrov, G. Miyamoto, T. Furuhashi, M.J. Santofimia, A quantitative investigation of the effect of Mn segregation on microstructural properties of quenching and partitioning steels. *Scripta Materialia*, 137 (2017) 27–30. <https://doi.org/10.1016/j.scriptamat.2017.04.040>
- [28] A. Arlazarov, M. Gouné, O. Bouaziz, A. Hazotte, G. Petitgand, P. Barges, Evolution of microstructure and mechanical properties of medium Mn steels during double annealing. *Materials Science and Engineering: A*, 542 (2012) 31–39. <https://doi.org/10.1016/j.msea.2012.02.024>
- [29] J. Hidalgo, C. Celada-Casero, M.J. Santofimia, Fracture mechanisms and microstructure in a medium Mn quenching and partitioning steel exhibiting macrosegregation. *Materials Science and Engineering: A*, 754 (2019) 766–777. <https://doi.org/10.1016/j.msea.2019.03.055>
- [30] R.J. Zhang, C.L. Zheng, B. Lv, P.J. Zhang, G.H. Gao, Y.Q. Yang, F.C. Zhang, Effect of non-uniform microstructure on rolling contact fatigue performance of bainitic rail steel. *International Journal of Fatigue*, 159 (2022) 106795. <https://doi.org/10.1016/j.ijfatigue.2022.106795>
- [31] F. Forouzan, L. Borasi, E. Vuorinen, F. Mücklich, Optimization of quenching temperature to minimise the micro segregation induced banding phenomena in quenching and partitioning (Q&P) steels. *Steel Research International*, 90 (2019) 1800281. <https://doi.org/10.1002/srin.201800281>
- [32] Q.L. Huang, O. Volkova, H. Biermann, J. Mola, Dilatometry analysis of dissolution of Cr-rich carbides in martensitic stainless steels. *Metallurgical and Materials Transactions A*, 48 (2017) 5771–5777. <https://doi.org/10.1007/s11661-017-4377-2>
- [33] J.R. Yang, T.H. Yu, C.H. Wang, Martensitic transformations in AISI 440C stainless steel. *Materials Science and Engineering: A*, 438 – 440 (2006) 276–280. <https://doi.org/10.1016/j.msea.2006.02.098>
- [34] L.X. Meng, H.H. Lu, W.Q. Li, H.K. Guo, J. Tian, W. Liang, High strength and plasticity of AISI 430 ferritic stainless steel achieved by a recrystallisation annealing before quenching and partitioning process. *Materials Science and Engineering: A*, 814 (2021) 141191. <https://doi.org/10.1016/j.msea.2021.141191>

- [35] G. Luo, H.Y. Li, Y.G. Li, J.Q. Mo, Microstructures and properties of a low-carbon-chromium ferritic stainless steel treated by a quenching and partitioning process. *Materials*, 12 (2019) 1704. <https://doi.org/10.3390/ma12101704>
- [36] J. Mola, B.C. De Cooman, Quenching and partitioning (Q&P) processing of martensitic stainless steels. *Metallurgical and Materials Transactions A*, 44 (2013) 946–967. <https://doi.org/10.1007/s11661-012-1420-1>
- [37] E.J. Seo, L. Cho, B.C. De Cooman, Application of quenching and partitioning processing to medium Mn Steel. *Metallurgical and Materials Transactions A*, 46 (2015) 27–31. <https://doi.org/10.1007/s11661-014-2657-7>
- [38] J.T. Armstrong, Quantitative elemental analysis of individual microparticles with electron beam instruments. in: K.F.J. Heinrich, D.E. Newbury (Eds.), *Electron Probe Quantitation*, Springer US, Boston, MA, 1991; 261–315.
- [39] S. Hu, Y.Z. Mao, X.B. Liu, E.H. Han, H. Hänninen, Intergranular corrosion behavior of low-chromium ferritic stainless steel without Cr-carbide precipitation after aging. *Corrosion Science*, 166 (2020) 108420. <https://doi.org/10.1016/j.corsci.2019.108420>
- [40] L. Raami, P. Peura, Influence of initial quenching on the microstructure and mechanical properties of quenched and partitioned ferritic stainless steels. *Materials Science and Engineering: A*, 847 (2022) 143339. <https://doi.org/10.1016/j.msea.2022.143339>
- [41] S.J. Lee, C.J. Van Tyne, A kinetics model for martensite transformation in plain carbon and low-alloyed steels. *Metallurgical and Materials Transactions A*, 43 (2012) 422–427. <https://doi.org/10.1007/s11661-011-0872-z>
- [42] E.J. Seo, L. Cho, B.C. De Cooman, Modified methodology for the quench temperature selection in quenching and partitioning (Q&P) processing of steels. *Metallurgical and Materials Transactions A*, 47 (2016) 3797–3802. <http://dx.doi.org/10.1007/s11661-016-3579-3>
- [43] S.M.C. Van Bohemen, J. Sietsma, Martensite formation in partially and fully austenitic plain carbon steels. *Metallurgical and Materials Transactions A*, 40 (2009) 1059–1068. <https://doi.org/10.1007/s11661-009-9796-2>
- [44] C. Celada-Casero, J. Sietsma, M.J. Santofimia, The role of the austenite grain size in the martensitic transformation in low carbon steels. *Materials & Design*, 167 (2019) 107625. <https://doi.org/10.1016/j.matdes.2019.107625>
- [45] S.R. Babu, D. Ivanov, D. Porter, Influence of microsegregation on the onset of the martensitic transformation. *ISIJ International*, 59 (2019) 169–175. <https://doi.org/10.2355/isijinternational.ISIJINT-2018-424>

## 4

## Investigation of the Microstructure Development during Partitioning after Room Temperature Quenching

This chapter is based on:

Gaojie Li, Konstantina Traka, Kees Kwarkernaak, Yaiza Gonzalez-Garcia, Maria Santofimia. Modelling the evolution of microstructural bands in a martensite/austenite Q&P processed stainless steel. Scripta Materialia. 2025; 257:116457.



## 4.1 Introduction

Quenching and Partitioning (Q&P) has been proposed [1-4] and developed over the last decades as a promising method to produce advanced high strength steels, including stainless steels, exhibiting good combination of strength and ductility. The Q&P treatment involves a quenching step in which a controlled fraction of martensite is formed, followed by an isothermal treatment aiming to the partitioning of carbon from the martensite into the untransformed austenite [4,5]. The resulting microstructure is formed by carbon-depleted martensite and carbon-enriched retained austenite. The thermodynamics of the partitioning step are essential for the theoretical understanding of the process. Speer et al. [4] described the endpoint of carbon partitioning based on the so-called constrained carbon equilibrium (CCE) [6,8] conditions, which assume that the carbon partitioning from martensite to austenite ends when the chemical potential of carbon is equal in both phases. These assumptions are considered in the absence of carbide formation and interface mobility.

Building upon the work of Speer et al. [4], numerous research works have experimentally shown and theoretically demonstrated the possible interference of the martensite/austenite interface movement with the process of carbon partitioning from martensite to austenite [9,10]. Particularly, the movement of the martensite-austenite interface during the partitioning step of the Q&P process has been detected in the literature through several different experimental techniques. For example, the interface motion has been revealed by simple observation of microstructures before and after partitioning with electron backscatter diffraction (EBSD) and through the application of in-situ heat treatments at the transmission electron microscope (TEM) [11,12]. The theoretical explanation of these interface phenomena, comes down to the chemical potential of the substitutional lattice being different between the two phases, thus leading to a driving force exerted at the phase boundaries. This mechanism leads to two different phenomena. The first and obvious expected process is the inevitable motion of the interface toward the global equilibrium phase fractions of martensite (body-centred cubic, BCC) and austenite (face-centred cubic, FCC). It should be clarified that global equilibrium is meant in the context of partitioning (i.e. no secondary phases, but phase equilibrium between BCC and FCC), specifically the regime at which iron and carbon in FCC are in equilibrium with carbon, and iron, respectively, in BCC, just as explained by Santofimia et al. [9].

The second process is the interface motion occurring based on the local and / or time-dependent carbon concentration at the interface. Since the interphases and the associated driving force only realise the local carbon concentrations, these would then depend also in the local topology. For example, we would expect that applying a modelling approach similar to [9] in a heterogeneous distribution of austenite, would lead to different behaviours regarding the phase growth due to the variations of carbon concentration at the different interfaces.

For this reason, the present work investigates the dynamics of martensite-austenite interfaces during the partitioning step of a Q&P processed microstructure of high topological heterogeneities. The aim is to investigate the local and temporal phase redistribution explained above, when carbon redistribution due to partitioning is heterogeneous, i.e. takes place differently among the microstructure. Specifically, we investigate a stainless steel that displays compositional segregation in the form of bands. It will be shown that the presence of microstructural bands in the form of austenite-rich and austenite-poor martensite/austenite locations at the quenching temperature leads to a distinct evolution of phase fractions during the partitioning step that differs per location. Eventually, the microstructural banding is significantly reduced. This behaviour is modelled using a full field modelling approach of the concurring processes, i.e. carbon partitioning and interphase migration, showing that the main reason behind such a microstructural evolution is topological.

## 4.2 Approach

### 4.2.1 Experimental Procedure

The materials are the same alloys (HMn and LMn) investigated in **Chapter 3** and our previous work [13]. The chemical compositions are shown in **Table 3.1**. Cylindrical specimens with 10 mm in length (rolling direction) and 4 mm in diameter are machined from the forged billet, and are heat treated in a Bähr 805 DIL A/D dilatometer. A type S thermocouple spot-welded on the surface is used to monitor and control temperature. Q&P heat treatments are carried out to observe the changing microstructure during the partitioning stage for the two different chemistries. As shown in **Figure 4.1**, the specimens are first fully austenitised at 1100 °C for 15 minutes, and quenched to room temperature (as-quenched specimens are marked as LMn-Q and HMn-Q). Subsequently, the specimens are held at 400 °C for 2 minutes and 5 minutes (Q&P specimens designated as LMn-QP2m, LMn-QP5m, HMn-QP2m, and HMn-QP5m respectively), and finally quenched again to room temperature (and -130 °C). The cryogenic experiments are performed to better assess the martensite formation kinetics and to determine the Ms temperature corresponding to fresh martensite in the last quench. These “sub-zero” heat treatments are also applied in the same dilatometer. Applied heating and cooling rates are 10 °C/s and 5 °C/s respectively.

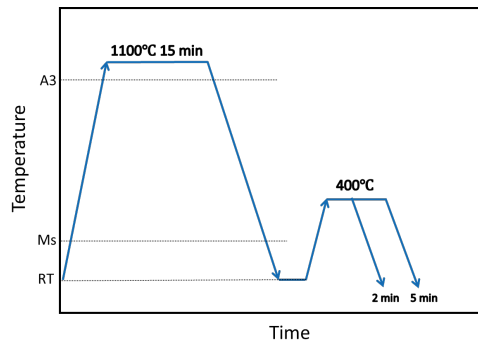


**Figure 4.1. Schematic of Q&P heat treatments. The quenching temperature is equal to room temperature (RT).**

Microstructural characterisation was conducted on the cross-sectional surface of the cylindrical specimen, oriented perpendicular to the rolling direction. The microstructure of each specimen is investigated by a LEICA optical microscope. Specimens for microstructure characterisation are prepared by grinding from P800 to P2000 on abrasive papers and polishing with 3  $\mu\text{m}$  and 1  $\mu\text{m}$  diamond paste. To reveal the microstructure, Vilella etchant is used by wiping with a cotton swab from 10 s to 50 s. Electron backscatter diffraction (EBSD) is performed using Helios G4 PFIB, with an acceleration voltage of 20 kV and working distance of 6 – 9 mm. With that aim, specimens are mechanically ground and polished, including a final polishing step with OPS suspension for 20 minutes. Data acquisition is performed with a step size of 200 nm in areas of 200  $\mu\text{m}$  x 200  $\mu\text{m}$ . Post-processing is done using TSL OIM Analysis software, where martensite is characterised as BCC and austenite as FCC.

Phase fractions are quantified in the specimens by X-ray Diffraction (XRD) using a Bruker D8 Discover diffractometer equipped with an Eiger-2500k 2D-detector and Co K $\alpha$  radiation. The diffractometer is operated with an acceleration voltage of 45 kV and a current of 35 mA. The scanning range of  $2\theta$  is 40° - 130° with a step size of 0.034°  $2\theta$  and a counting time of 2 s per step. The austenite volume fraction is calculated from the net integral intensities of the four austenite reflection peaks (111), (200), (220), and (311).

#### 4.2.2 Modelling

To understand the physical processes leading to these experimental findings, the microstructure development during the partitioning step is simulated using a model that couples carbon partitioning with phase redistribution. The model considers carbon redistribution due to interface partitioning [15] and mesoscale concentration gradients [16] as outlined in [17]. The interface migration is simulated based on the deterministic cellular automata approach [18] by using the short-range diffusion of the substitutional lattice description [19,20], driven by the local chemical potential difference, as explained

in [9]. Carbide precipitation during partitioning, as proposed by Toji et. al. [14] is not considered here because the aim of the study is to investigate whether the local topology is sufficient to explain the banding elimination, a phenomenon that is not expected to arise from carbide formation.

Regarding the modelling framework, the carbon redistribution occurs by the numerical description of concentration gradient-driven diffusion, with phase partitioning taking place as part of the numerical system, as explained in [17]. The local equilibrium of carbon at 400 °C is calculated for all possible local compositions, by setting equal the chemical potential of carbon in FCC and BCC, as calculated from Thermocalc using the TCFe13 database. The interface migration takes place based on the driving force arising from the chemical potential difference of iron between BCC and FCC for the given (simulated) local and temporal carbon concentrations, using the values obtained again from Thermocalc using the TCFe13 database. For a more detailed description of this model, the reader is referred to the **Appendix**.

## 4.3 Results

### 4.3.1 Analysis of Dilatometry Curves

**Figure 4.2** shows the dilatometry curves of the quenching and partitioning part of the heat treatment applied to the LMn and HMn. The martensite starts forming temperature is extracted and labelled as  $M_s$  in graphs, they are also provided in **Chapter 3**.

In **Figure 4.2(a)**, the LMn alloy displays the initiation of primary martensite formation at approximately 230 °C. The dilatometric curves display formation of fresh martensite ( $M_2$ ) at -40 °C (for a 2-minute partition) and -70 °C (for a 5-minute partition). For the HMn alloy, depicted in **Figure 4.2(b)**, the  $M_s$  temperature manifests around 150 °C. Fresh martensite start temperatures are 0 °C (for a 2-minute partition) and -45 °C (for a 5-minute partition), respectively.

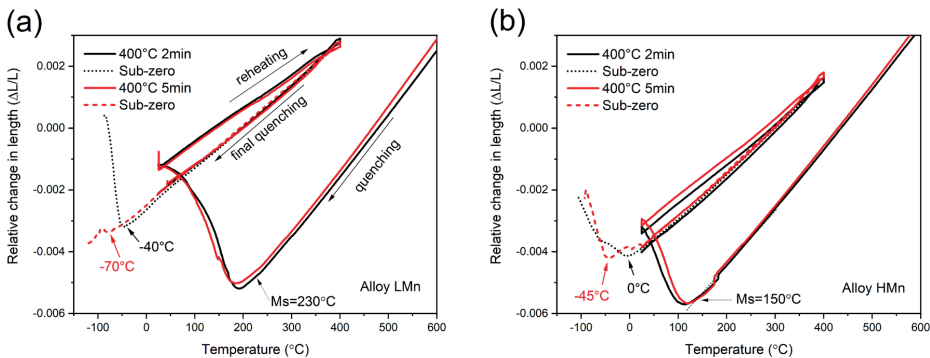


**Figure 4.2.** Dilatometry curves vs. temperature of the two different Q&P treatments of (a) alloy LMn and (b) alloy HMn.

### 4.3.2 Phase Fractions and Carbon Distribution before and after Partitioning

Austenite fractions prior to and following the partitioning process in both LMn and HMn alloys measured by XRD are presented in **Figure 4.3**. Note that in **Chapter 2**, we already indicated that the surface preparation process can introduce errors in XRD measurements. To mitigate this, the LMn-Q and HMn-Q specimens are both prepared (grinding and polishing) and tested again alongside the Q&P specimens in this work.

In the LMn alloy, the fraction of untransformed austenite before partitioning is 0.08 (in **Chapter 3** is  $0.11 \pm 0.02$ ). A 2-minute partitioning led to minimal alteration of the austenite fraction. Partitioning for 5 minutes led to a slight increase in retained austenite (RA) to around 0.13 is discerned.

The HMn alloy initially displayed a fraction of untransformed austenite of 0.27 (in **Chapter 3** is  $0.32 \pm 0.02$ ) prior to partitioning. Upon partitioning, both the QP2m and QP5m specimens led to a fraction of retained austenite of approximately 0.33. Taking into account a measurement uncertainty of  $\pm 0.02$ , the stabilisation of austenite can be regarded as fully realised.

As explained in **Chapter 3**, section 3.5.1 (**Figure 3.14**), there is no equation available that can accurately convert the lattice parameter of austenite into carbon concentration. Therefore, the carbon content in retained austenite is calculated using the  $M_s$  (and  $M_{s2}$ ) temperature obtained in **Figure 4.2** above. Applying the mentioned method, the carbon content of austenite in LMn alloy after partitioning is 0.77 wt.% and 0.83 wt.%, respectively, whereas in HMn alloy, it is 0.57 wt.% and 0.65 wt.%, respectively.

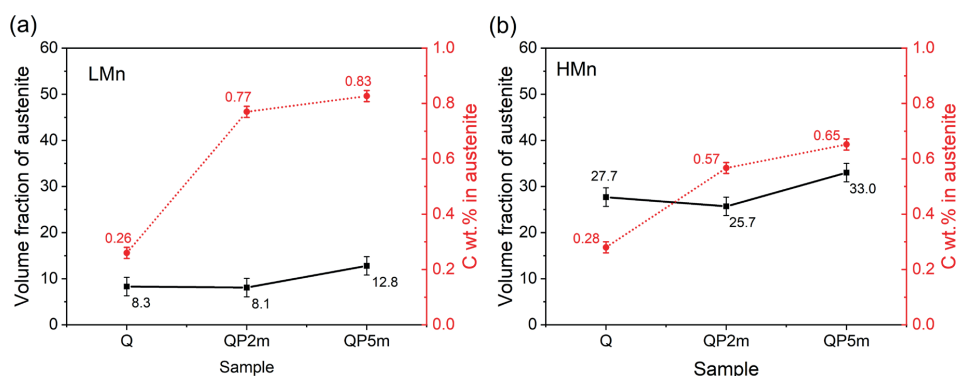


**Figure 4.3.** Fractions of retained austenite (from XRD) and corresponding carbon concentrations converted from  $M_{s2}$  temperatures of alloy (a) LMn and (b) HMn.

### 4.3.3 Microstructures by OM

**Figure 4.4** shows the microstructures of the LMn and HMn alloys after first quenching and after quenching and partitioning at 400 °C for 5 minutes, respectively. Microstructures formed by alternating

bands are observed in both quenched and Q&P processed specimens. For both alloys, the contrast between bands in the quenched specimen (**Figure 4.4** (a) and (c)) is more pronounced than in the Q&P treated specimen (**Figure 4.4** (b) and (d)). The chemical composition and forming kinetics of bands are detailed in **Chapter 3**.

Microstructural banding is a very common characteristic in steels. This phenomenon occurs due to the segregation of substitutional alloying elements during dendritic solidification. After processes such as hot rolling, areas with different segregation levels will align in the form of bands following the rolling direction. In this case, the high manganese content and its heterogeneous distribution explain the microstructures obtained. In our previous work [13], and as explained in **Chapter 3**, section 3.4.4 *Influence of elemental segregation on microstructures*, we conducted elemental analysis, revealing that the dark bands contain lower levels of Mn and Cr, whereas the light bands are rich in Mn and Cr. These variations in elemental content have a direct impact on the local Ms temperature, prior to the first quenching. As a result, the Mn and Cr-rich bands exhibit lower Ms temperatures, indicating a higher fraction of austenite, while the Mn and Cr-poor bands exhibit higher Ms temperatures, suggesting a lower fraction of austenite.

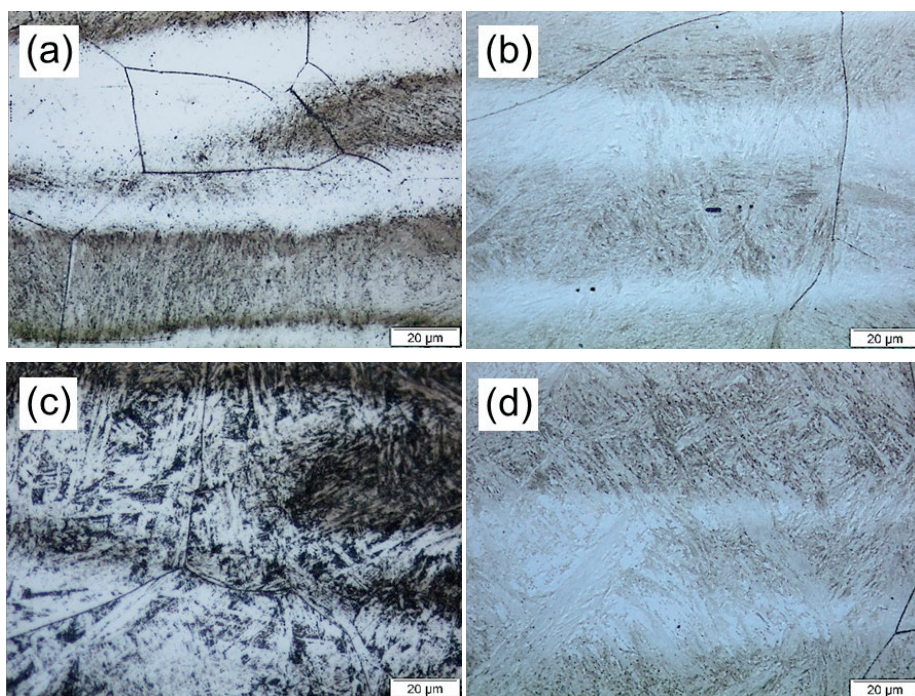


**Figure 4.4.** Microstructures after quenching and Q&P processing (partitioning at 400 °C for 5 minutes) of alloys LMn (a)(b) and HMn (c)(d), respectively.

#### 4.3.4 Microstructures before and after Partitioning with EBSD

**Figures 4.5** and **4.6** display the EBSD maps of LMn and HMn alloys after post-processing, in scanned areas of  $150 \times 150 \mu\text{m}^2$ . Austenite is color-coded with inverse pole figure (IPF). Martensite is plotted as color-coded with image quality (IQ) in the top row, and as black in the bottom row. Although the scanned areas are insufficient for reliable phase fraction quantifications due to the high heterogeneity caused by banding, the austenite fraction values obtained are quite consistent with the XRD measurements. Please note that since texture is not considered in this study, and the ND and TD directions cannot be determined from the circular cross-section. Therefore, the mentioned directions are used solely for comparing EBSD results with the model and validating the model's accuracy.

- LMn

The EBSD scan of the direct quenched specimen shows the austenite distributed following a band. The volume fraction of untransformed austenite measured with EBSD is 0.05. After partitioning for 2 minutes, the microstructure displays enhanced IQ. The distinct martensite laths are now clearly visible and the banding structure persists. The measured fraction of retained austenite from EBSD matches the XRD measurement, both being 0.08. Partitioning for 5 minutes leads to blocky-shaped retained austenite (RA) with large grain sizes together with small and homogeneously distributed RA grains. The fraction of retained austenite measured with EBSD is 0.12. The banding distribution is slightly less evident.

Note that the presented scanning areas are not intended for quantitative characterisation and the localised features may not fully represent the global structure due to the presence of heterogeneities. Nonetheless, it is still confirmed that elemental segregation contributes to the formation of microstructural bands, and regions rich in austenite are weakened but still persist after the partitioning process.

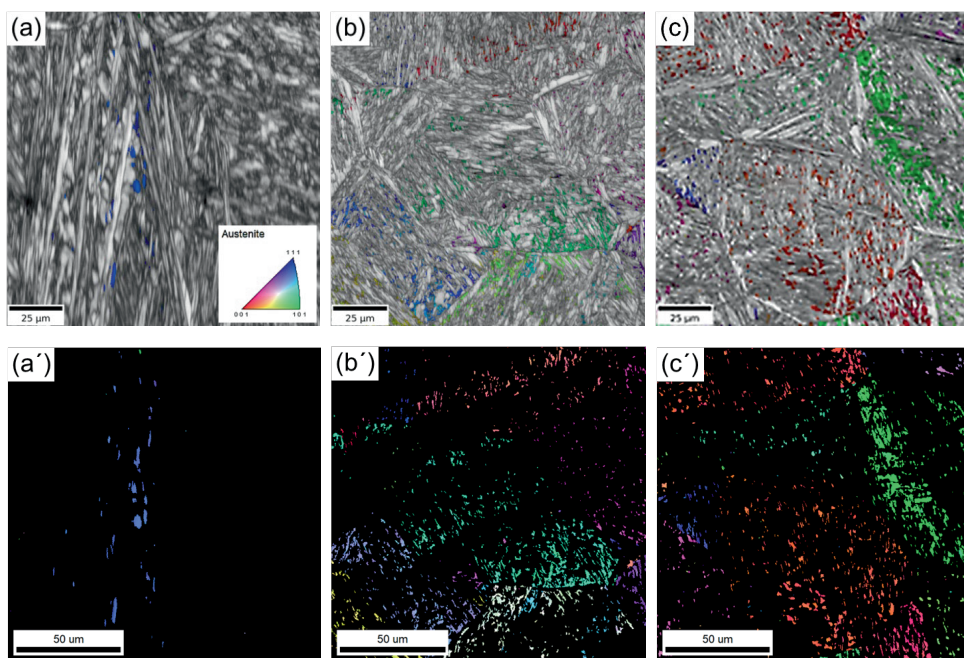


**Figure 4.5. EBSD maps at the three different Q&P stages of the LMn alloy (a)(a') as-quenched, (b)(b') QP2m and (c)(c') QP5m respectively. The images show the austenite crystal orientation color coded with inverse pole figure (IPF) along the normal direction (ND). IQ maps are added in the top row, while martensite is black in the bottom row.**

- HMn

The banding structure is evident in the EBSD image corresponding to the directly quenched specimen. Bands of untransformed austenite are fairly distributed along the boundaries of prior austenite grains, forming sizable blocks reaching dimensions of up to 50  $\mu\text{m}$ . The fraction of austenite displayed in this map is 0.25. After 2 minutes of partitioning, the microstructure shows a relatively even distribution of phases and improved image quality, with more distinct martensite laths. Retained austenite is observed in both blocks and films, with the fraction increased to 0.28. The previously observed banded structure is no longer visible, suggesting a transformation or realignment of the microstructural features. After partitioning for 5 minutes there is a consistent and uniform phase distribution. The majority of retained austenite appears as small blocks within the confines of prior austenite grains. The fraction increased to 0.31. The banded structure is no longer visible, indicating a redistribution of austenite.

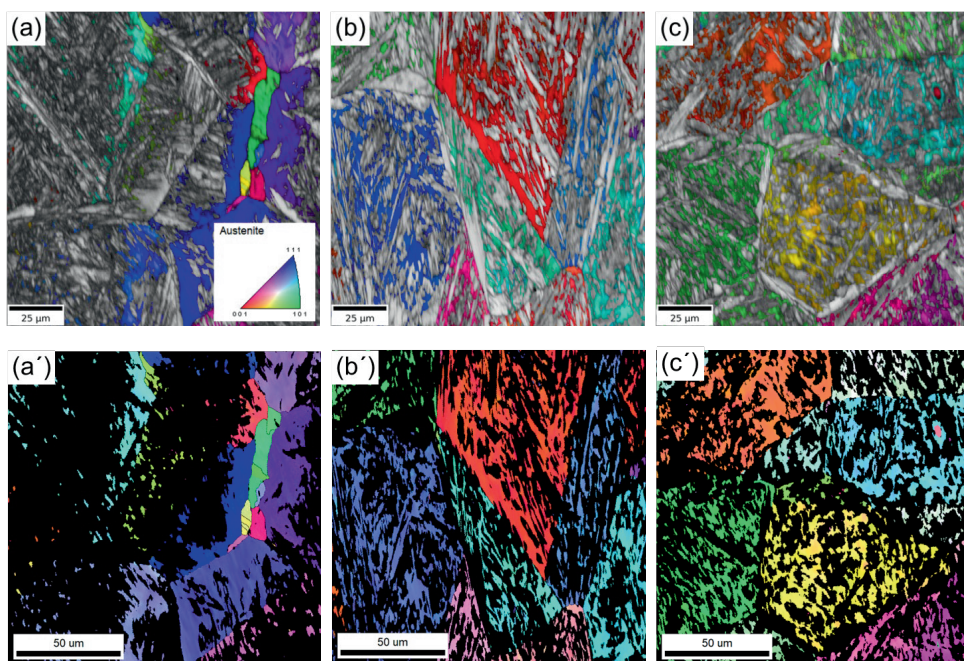


**Figure 4.6.** EBSD maps at the three different Q&P stages of the HMn alloy (a)(a') as-quenched, (b)(b') QP2m and (c)(c') QP5m respectively; The images show the austenite crystal orientation color coded with inverse pole figure (IPF) along the normal direction (ND). IQ maps are added in the top row, while martensite is black in the bottom row.

In summary, retained austenite bands are observable in the LMn alloy both before and after partitioning. These bands are not visible after partitioning in the HMn alloy. Further analysis is required to understand these alterations in the microstructure.

## 4.4 Discussion

We will focus on understanding the elimination of the band in HMn, and subsequently discuss the role of Mn in the fact that the band is not clearly eliminated in LMn. EBSD maps in **Figure 4.6** reveal distinct bands of austenite at the quenching state and a notable "redistribution" of austenite after the partitioning process. This redistribution involves the disappearance of austenite bands, possibly indicating the growth of austenite in austenite-poor area, as well as the transformation from austenite to martensite in austenite-rich regions.

### 4.4.1 Banding Elimination during Partitioning

The banded structure eliminates in HMn alloy during partitioning. This is presumably linked to the very high heterogeneity of local phase fractions and thus carbon redistribution. Nevertheless, we have

insufficient insight into LMn. This includes the quenched state and the likelihood that the expected small austenite regions may not be captured in the EBSD. Additionally, the complexity of the concurrent physical processes—interface migration, carbon redistribution, and the role of Mn—further complicates analysis. Therefore, only HMn is discussed.

The diffusivities of carbon in martensite and austenite used in the simulations, as well as the parameters associated with the mobility of the martensite-austenite interface, are displayed in **Table 4.2**. For a more detailed description of this model, as well as for its physical validation (i.e. grid sensitivity tests and global equilibrium) the reader is referred to the **Supplementary Material**. The model is implemented in OMicron (optimising microstructures numerically) [17,19], and in CASIPT (cellular automata model for phase transformations) [17,19,21,22]. In all simulations performed in this work, the starting microstructure obtained by EBSD is imported into the model by a one-to-one fashion, i.e. every simulation cell assumes the crystal orientation and phase equal to the ones measured for the pixel in the same spatial coordinates. The 2D microstructures are resolved by square cells of grid spacing equal to 0.2  $\mu\text{m}$ .

**Table 4.2. Parameters used in the simulations.**

Carbon diffusivity in martensite $D_{C,i}^{\alpha}$ [m <sup>2</sup> /s]	$1.06 \cdot 10^{-13}$	From Agren 1982, [26] at 400 °C
Carbon diffusivity in austenite $D_{C,i}^{\gamma}$ [m <sup>2</sup> /s]	$6.1 \cdot 10^{-13}$	Effective for $X_{C,i}^{\gamma} = 3.8$ wt.% (expected equilibrium) using Agren 1986, [27] at 400 °C
Pre-exponential factor for interface mobility $M_0^{\alpha\gamma}$ [mol · m/(J · s)]	0.4	Based on theoretical arguments in [28-30] and investigations in [19,20].
Activation energy for interface mobility $Q^{\alpha\gamma}$ [kJ/mol]	140	Hillert 2006 [31]

At first, we simulate carbon partitioning under the assumption of fixed interfaces, in order to demonstrate the associated local and temporal carbon concentration heterogeneity in absence of heterogeneous interface migrations. **Figure 4.7** shows the spatial evolution of the carbon concentration under the assumption of immobile interfaces. A significant heterogeneity in the carbon concentration near the austenite/martensite interfaces is observed. In regions containing small austenite units/fractions, such as the zoomed area on the left in **Figure 4.7**, austenite becomes richer in carbon than in regions containing large austenite grains and fractions, as the one zoomed on the right in **Figure 4.7**. That is because the local fraction of austenite is significantly higher than local fraction of martensite, and thus, carbon diffuses away from the interfaces to enrich the bulk austenite. These simulations indicate that

the heterogeneous distribution of austenite leads to significant variance of the local carbon concentrations during partitioning and, thus also, high topological scatter in the deviation of local carbon concentrations from the equilibrium state. Such differences from the local (and eventually also global) equilibrium carbon concentrations provide the driving force for the local phase growth, which will also be shown to be highly heterogeneous.

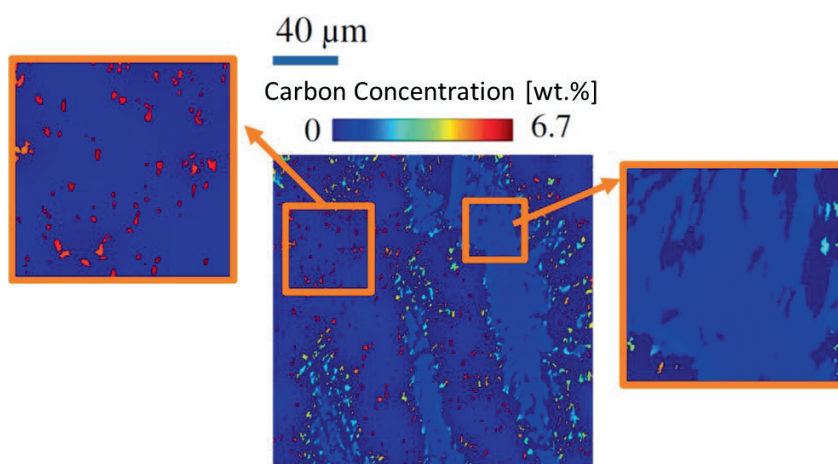


**Figure 4.7.** Simulated carbon concentration during partitioning, under the assumption of fixed interfaces, in the system after partitioning at 400 °C for 300 s.

**Figure 4.8** shows the simulated microstructure where carbon partitioning is coupled with interface migration. **Figure 4.8 (a)** shows the simulated carbon distribution maps after partitioning at 400 °C for 0 s, 60 s, 120 s, and 300 s, whereas **Figure 4.8 (b)** displays the corresponding austenite distribution (crystal direction // ND). At the beginning of partitioning, carbon distribution is homogeneous, and the concentration is equal to the alloy's carbon composition. After 60 s, carbon partitioning is evidenced by the higher carbon contents in small austenite phase particles (red areas) next to the martensite/austenite interfaces compared to those in the inner part (light blue) of the austenite long blocks. As the partitioning time increases, the austenite areas gradually grow, and the inner part of the austenite blocks starts being replaced by martensite areas. After 300 s, the red-colored austenite grains are distributed uniformly across the matrix. The banded austenite distribution is eventually almost replaced by uniformly distributed austenite phase particles. The simulation results correspond well to the trends revealed by the EBSD observations and explain the phenomenon of the banding elimination.

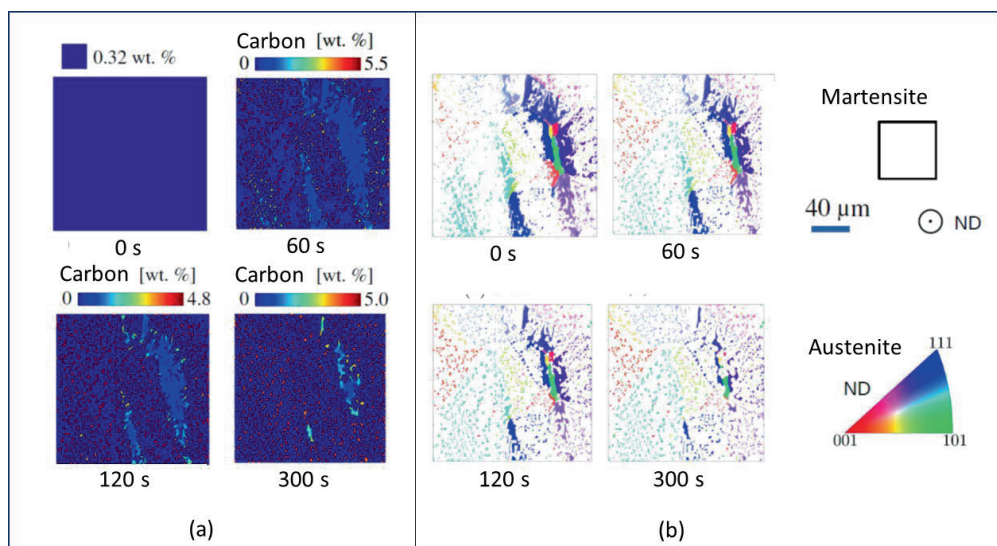


**Figure 4.8. Simulated evolution of the microstructure and carbon concentration in the system during partitioning at 400 °C assuming a mobile martensite-austenite interface. (a) Carbon concentration and (b) crystal direction parallel to ND (inverse pole figure).**

#### 4.4.2 The Influence of Mn during Partitioning

Up to now, the simulations explain the banding elimination, but the global phase fractions are much lower than the experimentally obtained ones. Particularly, the simulated austenite fraction is 0.08, in line with the expected global equilibrium based on the Fe-C chemical potential equilibrium, whereas the experimental austenite fraction is 0.33. A possible reason is the role of martensite defects. It is known that, although in partitioning simulations martensite is treated as a phase identical to strained-free ferrite, in martensite-austenite microstructures the experimental phase fractions and the carbon concentrations are typically different from the equilibrium values [24]. Therefore, even in Fe-C materials, it is expected that the defects in martensite affect the partitioning evolution. Specifically, the carbon chemical potentials are affected and may lead to high localised carbon concentration in martensite, just as explained by Traka et al. [17]. Such a case would potentially result in localised austenite formation, as also observed in [12]. But also the iron chemical potentials, from the strain energy barrier in the martensite growth, as explained analytically by Behera and Olson [25]. Either way, i.e. due to local aspects or global equilibrium, the theoretical global equilibrium inherent to the present simulations is already expected not to reach the accurate austenite fractions.

Nevertheless, in view of the high Mn content of the present material, we take this opportunity to discuss an additional reason for the phase fraction evolution during partitioning, especially since we

have two concurrent phenomena taking place, i.e. the banding elimination and the global phase fractions evolution. The banding elimination is not a result of the Mn content, but the evolution of global phase fractions is. Therefore, we can discuss the effects of Mn since now not only the bands be eliminated but also the austenite fractions should remain almost unchanged (i.e. like the experimental measurement). In the following, the effect of Mn on the carbon partitioning process is discussed. Particularly, the chemical potentials of carbon and substitutional lattice are considered in the simulations through three different systems and conditions at the martensite/austenite interface: iron-carbon, iron-carbon-manganese under para-equilibrium (PE) conditions and iron-carbon-manganese under local equilibrium-negligible partitioning (LENP) conditions. The LENP is incorporated by assuming that while the mesoscale Mn distribution is unaffected, the moving interfaces lead to the local partitioning of Mn in the austenite side of the austenite-martensite interface, i.e. every adjacent austenite-martensite cells have an average of 3.1 wt.% Mn during all simulated stages, whereas every interface separates infinitesimal areas of austenite with 6 wt.% Mn and martensite with 0 wt.% Mn. This means that the chemical potentials of carbon and substitutional lattice at the interface correspond to FCC with 6 wt.% Mn and BCC in the absence of Mn.

The corresponding simulation results are shown in **Figure 4.9** for the case of partitioning at 400 °C. In order to understand the outcomes of this figure, it is important to first mention that the expected equilibrium fractions of austenite under the three different evaluated conditions are different. Particularly, 0.09 for the F-C system, 0.11 for the Fe-C-Mn under PE and 0.20 for the Fe-C-Mn under LENP. This explains that after 300 s of partitioning at 400 °C, the simulations show that the fraction of austenite reached under the different conditions is 0.10 (Fe-C), 0.11 (Fe-C-Mn, PE) and 0.25 (Fe-C-Mn LENP), this last one evolving to a fraction of 0.22 after 900 s of partitioning at 400 °C. The close relation between the reached fraction of austenite and the expected from equilibrium under different conditions displays that the simulated band elimination together with the austenite fraction evolution is indeed insightful to understanding the role of Mn.

Particularly, the Fe-C case brings a fast elimination of the band, since martensite grows rapidly at the expense of the large austenite grains. However, the austenite phase fraction remains much lower than what is observed experimentally (0.31 in the EBSD scan of **Figure 4.6**). Considering the effect of Mn under PE conditions leads to a slower elimination of the bands. Altogether, it seems that the LENP conditions brings the most realistic outcome, where banding elimination, although slower, occurs, and at the same time the global fractions are closer to the experimentally observed. This becomes clearer in **Figure 4.9** (e), where the austenite fraction evolution is quantified in the two different areas indicated in **Figure 4.9** (a). Area 1 is initially austenite-poor and area 2 is initially austenite-rich. The only simulation where the austenite fraction evolution in both areas converges to the experimentally observed is the one performed under LENP conditions. In-situ investigations of the evolution of phase

fraction and composition during the partitioning step in these materials may contribute to clarify the thermodynamic conditions governing the described processes.

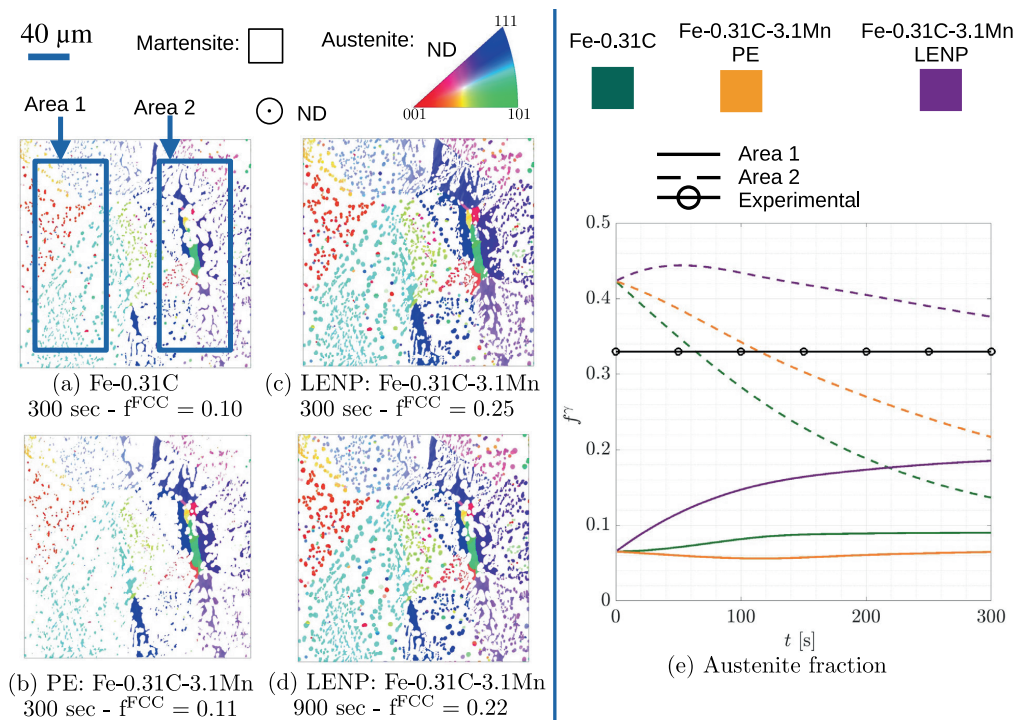


**Figure 4.9.** Effect of Mn in the temporal microstructure evolution during partitioning. (a)-(d) show the outcome in the absence of Mn, including Mn and PE, and including Mn and LENP (300 s and 900 s), respectively. (e) shows the evolution of the austenite fraction in two different locations of the microstructure under the different conditions.

## 4.5 Conclusions

In this work, the microstructural evolution of two stainless steels with different Mn content during the application of Q&P heat treatments is investigated. Particularly, the materials are subjected to a room temperature quenching step, which allowed the observations of microstructures before and after partitioning.

It is observed that the elemental segregation of Mn and Cr leads to a distribution of martensite start temperatures that leads to the presence of austenite bands at the quenching step. Although the elemental segregation bands persist during the partitioning step, in HMn alloy, there is a clear change in the banded distribution of austenite, where the microstructural bands have been eliminated and replaced by a relatively uniform microstructure. A partitioning model, considering carbon interphase partitioning,

carbon diffusion, and interface migration, explained the evolution mechanism of banding microstructure elimination, in terms of local carbon concentration and thus driving force for interface migration heterogeneity. In addition, in view of the contradicting phenomena observed, i.e. the phase growth toward banding elimination and the phase growth toward global equilibrium, we took the opportunity to investigate different thermodynamic equilibrium assumptions. In terms of the role of Mn, the simulations showed that LENP conditions best describe the observed microstructural evolution. The difference in banding microstructure elimination behaviour of LMn and HMn alloys is explained by a) the phase fraction of austenite, as nucleation/growth sites for austenite, is more in HMn alloy; and b) the C diffusion is barely affected by Mn content.

## References

- [1] D.K. Matlock, J.G. Speer, Third generation of AHSS: Microstructure design concepts, in microstructure and texture in steels, A. Haldar, S. Suwas, and D. Bhattacharjee, Eds., London: Springer London, (2009)185–205. [https://doi.org/10.1007/978-1-84882-454-6\\_11](https://doi.org/10.1007/978-1-84882-454-6_11)
- [2] X. Hu, Z. Feng, Advanced high-strength steel - basics and applications in the automotive industry, ORNL/TM-2021/2047, (2021) 1813170. <https://doi.org/10.2172/1813170>
- [3] J.G. Speer, A.M. Streicher, D. Matlock, F. Rizzo, G. Krauss, Quenching and partitioning: A fundamentally new process to create high strength trip sheet microstructures. Materials Science and Technology 2003 Meeting, (2003)505–522.
- [4] J.G. Speer, D.K. Matlock, B.C. De Cooman, J.G. Schroth, Carbon partitioning into austenite after martensite transformation. *Acta Materialia*, 51(9) (2003) 2611–2622. [https://doi.org/10.1016/S1359-6454\(03\)00059-4](https://doi.org/10.1016/S1359-6454(03)00059-4)
- [5] J.G. Speer, F.C.R. Assunção, D.K. Matlock, D.V. Edmonds, The ‘quenching and partitioning’ process: background and recent progress. *Materials Research*, 8(4) (2005) 417–423. <http://dx.doi.org/10.1590/S1516-14392005000400010>
- [6] M. Hillert, J. Ågren, On the definitions of paraequilibrium and orthoequilibrium. *Scripta Materialia*, 50(5) (2004) 697–699. <https://doi.org/10.1016/j.scriptamat.2003.11.020>
- [7] J.G. Speer, D.K. Matlock, B.C. DeCooman, J.G. Schroth, Comments on ‘On the definitions of paraequilibrium and orthoequilibrium’ by M. Hillert and J. Ågren, *Scripta Materialia*, 50, 697–9 (2004). *Scripta Materialia*, 52(1) (2005) 83–85. <https://doi.org/10.1016/j.scriptamat.2004.08.029>
- [8] M. Hillert, J. Ågren, Reply to comments on ‘On the definition of paraequilibrium and orthoequilibrium’. *Scripta Materialia*, 52(1)(2005) 87–88. <https://doi.org/10.1016/j.scriptamat.2004.08.026>
- [9] M.J. Santofimia, L. Zhao, J. Sietsma, Model for the interaction between interface migration and carbon diffusion during annealing of martensite–austenite microstructures in steels. *Scripta Materialia*, 59(2) (2008) 159–162. <https://doi.org/10.1016/j.scriptamat.2008.02.045>
- [10] M.J. Santofimia, J.G. Speer, A.J. Clarke, L. Zhao, J. Sietsma, Influence of interface mobility on the evolution of austenite–martensite grain assemblies during annealing. *Acta Materialia*, 57(15) (2009) 4548–4557. <https://doi.org/10.1016/j.actamat.2009.06.024>
- [11] S. Dieck, P. Rosemann, A. Kromm, T. Halle, Reversed austenite for enhancing ductility of martensitic stainless steel. *IOP Conf. Series: Materials Science and Engineering*, 181(2017) 012034. <http://dx.doi.org/10.1088/1757-899X/181/1/012034>
- [12] L. Yuan, D. Ponge, J. Wittig, P. Choi, J.A. Jiménez, D. Raabe, Nanoscale austenite reversion through partitioning, segregation and kinetic freezing: Example of a ductile 2GPa Fe-Cr-C steel. *Acta Materialia*, 2012. 60(6-7): 2790-2804. <https://doi.org/10.1016/j.actamat.2012.01.045>

- [13] G. Li, C. Kwakernaak, A. Smith, M. Muratori, Y. Gonzalez-Garcia, M. J. Santofimia, Microstructure development of quenching and partitioning-processed martensitic stainless steels with different manganese content. *Materials Science and Technology*, 40(6) (2024) 449-465. <https://doi.org/10.1177/02670836231215989>
- [14] Y. Toji, G. Miyamoto, D. Raabe, Carbon partitioning during quenching and partitioning heat treatment accompanied by carbide precipitation. *Acta Materialia*, 86(2015) 137-147. <https://doi.org/10.1016/j.actamat.2014.11.049>
- [15] S. Matas, R. F. Hehemann, Retained austenite and the tempering of martensite. *Nature*, 187(4738) (1960) 685–686. <https://doi.org/10.1038/187685a0>
- [16] A. Fick, Ueber diffusion, *Annual Review of Physical Chemistry*, 170(1)(1855) 59–86. <https://doi.org/10.1002/andp.18551700105>
- [17] K. Traka, J. Sietsma, M.J. Santofimia, Modeling the interaction of carbon segregation to defects and carbon partitioning in multiphase steels. *Acta Materialia*, 277(2024) 120204. <https://doi.org/10.1016/j.actamat.2024.120204>
- [18] J. G. Kemeny, Theory of Self-Reproducing Automata. John von Neumann. Edited by Arthur W. Burks. University of Illinois Press, Urbana, 1966. 408 pp., illus. \$10, Science, 157(3785) (1967) 180–180. <https://cba.mit.edu/events/03.11.ASE/docs/VonNeumann.pdf>
- [19] K. Traka, K. Sedighiani, C. Bos, J.G. López, K. Angenendt, D. Raabe, J. Sietsma, Topological aspects responsible for recrystallization evolution in an IF-steel sheet – Investigation with cellular-automaton simulations. *Computational Materials Science*, 198 (2021) 110643. <https://doi.org/10.1016/j.commatsci.2021.110643>
- [20] K. Traka, Investigations of the early stages of recrystallization in interstitial-free and low-carbon steel sheets. Ph.D. thesis, Delft University of Technology, (2022). <https://doi.org/10.4233/uuid:962f6655-a1b8-4c38-8467-0b2b651ab629>
- [21] C. Bos, M.G. Mecozzi, J. Sietsma, A microstructure model for recrystallisation and phase transformation during the dual-phase steel annealing cycle. *Computational Materials Science*, 48(3)(2010) 692–699. <https://doi.org/10.1016/j.commatsci.2010.03.010>
- [22] C. Bos, M.G. Mecozzi, D.N. Hanlon, M.P. Aarnts, J. Sietsma, Application of a three-dimensional microstructure evolution model to identify key process settings for the production of dual-phase steels. *Metallurgical and Materials Transactions A*, 42(12)(2011) 3602–3610. <https://doi.org/10.1007/s11661-011-0696-x>
- [23] A.S. Nishikawa, M.J. Santofimia, J. Sietsma, H. Goldenstein, Influence of bainite reaction on the kinetics of carbon redistribution during the Quenching and Partitioning process. *Acta Materialia*, 142 (2018) 142–151. <https://doi.org/10.1016/j.actamat.2017.09.048>

- [24] S. Kumar, Quenching and partitioning (Q&P) process: A critical review of the competing reactions. *Materials Science and Technology*, 38(11) (2022) 663–675. <https://doi.org/10.1080/02670836.2022.2062646>
- [25] A.K. Behera, G.B. Olson, Nonequilibrium thermodynamic modeling of carbon partitioning in quench and partition (Q&P) steel. *Scripta Materialia*, 147(2018) 6–10. <https://doi.org/10.1016/j.scriptamat.2017.12.027>
- [26] J. Ågren, Diffusion in phases with several components and sublattices. *Journal of Physics and Chemistry of Solids*, 43(1982) 421–430. [https://doi.org/10.1016/0022-3697\(82\)90152-4](https://doi.org/10.1016/0022-3697(82)90152-4)
- [27] J. Ågren, A revised expression for the diffusivity of carbon in binary Fe-C austenite. *Scripta Metallurgica*, 20(1986) 1507–1510. [https://doi.org/10.1016/0036-9748\(86\)90384-4](https://doi.org/10.1016/0036-9748(86)90384-4)
- [28] C.S. Smith, Grains, phases, and interphases: an interpretation of microstructure. *Transactions of the Metallurgical Society of AIME*, 175 (1948) 15–51.
- [29] C.S. Smith, Grain shapes and other metallurgical applications of topology. *Metallography, Microstructure, and Analysis*, 4(6) (2015) 543–567. <https://doi.org/10.1007/s13632-015-0241-1>
- [30] J.E. Burke, D. Turnbull, Recrystallization and grain growth. *Progress in Metal Physics*, 3(1952) 220–292. [https://doi.org/10.1016/0502-8205\(52\)90009-9](https://doi.org/10.1016/0502-8205(52)90009-9)
- [31] M. Hillert, L. Hoglund, Mobility of  $\alpha/\gamma$  phase interfaces in Fe alloys. *Scripta Materialia*, 54(7) (2006) 1259–1263. <https://doi.org/10.1016/j.scriptamat.2005.12.023>

## 5

## Pit Initiation in Quenching and Partitioning Processed Martensitic Stainless Steels

This chapter is based on:

Gaojie Li, Ziyu Li, Ehsan Rahimi, Marta Muratori, Ali Smith, Maria J. Santofimia Navarro, Yaiza Gonzalez-Garcia. Pit initiation in quenching and partitioning processed martensitic stainless steels. *Electrochimica Acta*. 2024; 498: 144646.



## 5.1 Introduction

In previous chapters we have introduced the quenching and partitioning (Q&P) process [1-10] and understood the microstructure development during the application of Q&P heat treatments on our designed martensitic stainless steels. In this chapter, we will focus on the correlation between microstructure and the corrosion performance of these stainless steels.

The Q&P process has been successfully applied to stainless steels, leading to high-strength martensitic stainless steels [11-16]. Investigations on Q&P processed martensitic stainless steels have mainly focused on the relationship between microstructure and mechanical properties [12,13,16,17] and have evidenced the precipitation of carbides in the microstructures [11-16]. The presence of carbides, and particularly Cr-carbides, brings concerns regarding the subsequent Cr depletion, which can affect the corrosion resistance of these steels.

Research on the corrosion performance of Q&P steels reports that both Q&P carbon steels [18,19] and stainless steels [14,16,20] exhibit better corrosion resistance than traditional quenching and tempering (Q&T) steels. In Q&T steels, retained austenite is absent or present in very low fractions (typically less than 0.01). Therefore, carbon is dissolved in the martensite [18,19]. In Q&P steels, the C-depleted martensite is electrochemically more active than the C-rich retained austenite. The total cathodic area (C-rich retained austenite) in the Q&P steels is smaller than in the Q&T steels (C-rich martensite). Thus, the corrosion rate for Q&P steels is lower than for Q&T steels [19]. Moreover, the long tempering treatments applied to Q&T-processed steels (of the order of hours) allow the precipitation of Cr-carbides, leading to Cr-depletion at the carbide-matrix interface region, which is susceptible to the initiation of pitting corrosion. In the case of Q&P steels, the isothermal treatments applied are shorter (typically minutes), reducing, but not eliminating, the chances of Cr-carbide precipitation. Consequently, Q&P processed steels might present better pitting corrosion resistance than conventional Q&T steels [14,16,20].

In industrial production, impurity elements induce inclusions that cannot be completely avoided. Manganese sulfides (MnS) in particular act as an active site for pitting initiation in a chloride environment [21-31]. It is generally agreed that the existence of MnS inclusions on steel surfaces leads to discontinuities in passive films, and the local dissolution at the MnS sites acts as an initiation of pitting corrosion, which makes the sample surface more easily attacked by chloride ions [25-27].

Incorporating microalloying elements, such as Ti and Nb, in steels is a common strategy [32-37] to improve impact toughness and strength by grain size refinement [33] and precipitation strengthening. This is due to the formation of nano-sized TiN and NbC particles. The combined effect of nano-sized precipitates and the transformation-induced plasticity (TRIP) of retained austenite leads to an

exceptional balance between strength and ductility [36]. However, several works have shown the detrimental effect of TiN precipitates in corrosion. These works have investigated localised corrosion initiation at TiN inclusions in Ni-based alloys [38,39], austenitic stainless steel [40], and interstitial-free (IF) steel [41]. Overall, these studies have consistently demonstrated a decrease in corrosion resistance and an increased susceptibility to localised corrosion attacks when TiN inclusions are present. Similar to MnS inclusions, TiN inclusion also serves as a preferential site for initiating corrosion [41,42].

Although corrosion mechanisms involving MnS and TiN inclusions have been investigated in the literature, the specific role of MnS and TiN inclusions in the corrosion resistance of Q&P steels is still not understood. Q&P steels are multiphase steels in which an additional influence of the C-enriched austenite and the C-depleted martensite is expected.

The objective of this study is to evaluate the effect of chemical composition and microstructure on the corrosion resistance of Q&P produced martensitic stainless steels and, particularly, the combined effect of C-enriched austenite, C-depleted martensite and inclusions on the corrosion mechanisms. With that aim, Q&P microstructures of three different alloys differing in C, Mn, and microalloying (Ti and Nb) content are characterised. Local surface potential differences are investigated by atomic force microscopy (AFM) and scanning Kelvin probe microscopy (SKPFM). The composition of the formed passive film on the sample surface is analysed using X-ray photoelectron spectroscopy (XPS). The electrochemical behaviour of the Q&P steels is investigated with open circuit potential (OCP) and potentiodynamic polarisation (PDP) at an aerated 3.5 wt.% NaCl solution. Moreover, the evolution of localised corrosion initiation is conducted by in-situ scanning electrochemical microscopy (SECM) experiments by operating in substrate generation/tip collection (SG/TC) mode.

## 5.2 Experimental Procedure

### 5.2.1 Materials

In this chapter, we investigate the designed alloys 2C LMn, 3C LMn, and 3C HMn-NbTi, as introduced in **Chapter 2**. Unlike the laboratory dilatometer-processed specimens examined in **Chapter 3** and **Chapter 4**, the Q&P steels in this study are processed at RINA-CSM (Italy). The dimensions of these steels are 250 mm in length (rolling direction), 200 mm in width, and 1.5 mm in thickness.

The chemical composition of the three stainless steel samples is given in **Table 5.1**. Alloys 2C LMn and 3C LMn have the same alloy content but different carbon content. Alloy 3C HMn-NbTi is similar to alloy 3C LMn but with increased Mn and microalloying additions. Specimens 20 mm in length and 15 mm in width are prepared by electrical discharge machining from the sheets with the long axis parallel to the rolling direction. The Q&P treatment (**Figure 5.1**), optimised in **Chapter 2**, also in research [43], consisted of austenitising at 1100 °C for 15 minutes, followed by quenching to 160 °C

for alloy 2C LMn, 99 °C for alloy 3C LMn and room temperature (25 °C) for alloy 3C HMn-NbTi. The materials are then subjected to partitioning at 450 °C for 5 minutes, followed by a final quenching to room temperature.

**Table 5.1. Chemical composition of the steels, in wt.%.**

Alloy	C	Mn	Si	Cr	Ni	Al	N	Nb	Ti	Fe
2C LMn	0.2	0.7	0.35	12.5	0.2	0.01	0.03	-	-	Bal.
3C LMn	0.3	0.7	0.35	13.0	0.2	0.01	0.03	-	-	Bal.
3C HMn-NbTi	0.3	3.0	0.35	13.0	0.2	0.01	0.03	0.05	0.05	Bal.

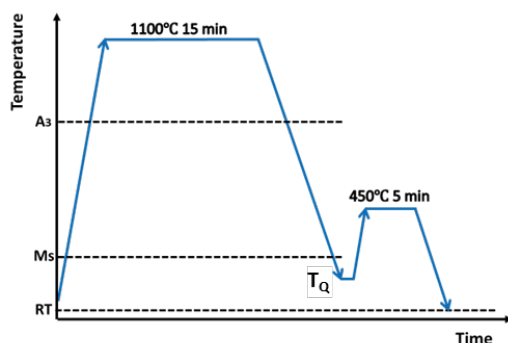


**Figure 5.1. A schematic presentation of the Q&P heat treatment, where  $A_3$  indicates the temperature above which only austenite is present in the microstructure.  $M_s$  is martensite start temperature.  $T_Q$  is quenching temperature. RT is room temperature.**

### 5.2.2 Microstructural and Compositional Analysis

The surface of the samples is prepared by standard metallographic procedures and finished by OPS (Oxide Polishing Suspensions) polishing for 15 minutes. Optical microscopy (Digital Keyence VHX-5000 and optical LEICA DMLM) is used to characterise the surface and identify the regions of interest for further study. A FEG-SEM CarlZeiss Crossbeam 550 scanning electron microscope (SEM) equipped with energy-dispersive X-ray spectroscopy (EDS) detector is used to characterise the microstructures and analyse the elemental composition of the samples (matrix and inclusions/particles). All SEM/EDS data are collected at a working distance of 8.5 mm and an accelerating voltage of 10 kV.

Phase fractions are quantified in the specimens by X-ray Diffraction (XRD) using a Bruker D8 Discover diffractometer equipped with an Eiger-2500k 2D-detector and Co  $K\alpha$  radiation. The diffractometer is operated with an acceleration voltage of 45 kV and a current of 35 mA. The scanning range of  $2\theta$  is  $40^\circ$  -  $130^\circ$  with a step size of  $0.034^\circ 2\theta$  and a counting time of 2 s per step. The austenite

volume fraction is calculated from the net integral intensities of the four austenite reflection peaks (111), (200), (220), and (311).

X-ray photoelectron spectroscopy (XPS) measurements are conducted to analyse the chemical composition and relative fractions of the formed (hydro)oxide layers. Before XPS measurements, the passive layer is formed by potentiostatic polarisation at 0.1 V (vs. Eoc) for two hours in 3.5 wt.% NaCl solution. Subsequently, the pre-passivated samples are rinsed with ethanol and dried with compressed air. The XPS analysis is conducted using a PHI-Versaprobe III spectrometer equipped with an Al-source (1486.71 eV photon energy) and automatic neutraliser. The irradiation power of the X-ray beam is set to 23.8 W, and a take-off angle of 46° is applied. All the specimens are measured at two different locations on the surface (100 µm in diameter) to verify the homogeneity of the layer composition. The elemental composition is determined by XPS survey (high-sensitivity) spectra, combined with high-energy resolution spectra of O 1s, C 1s, N 1s, Fe 2p, and Cr 2p atomic concentrations. The Shirley method is used for background subtraction, and peak deconvolution is performed using the PHI Multipack software (V9.0). Binding energies are corrected for possible charging effects by referencing the C 1s (284.8 eV) peak.

### 5.2.3 Electrochemical Analysis

Conventional electrochemical experiments using potentiodynamic polarisation (PDP) are performed. Before the measurements, samples are embedded in an epoxy resin. Part of the sample surface is masked off by lacquer or covered by tape to control the exposing area and prevent possible crevice corrosion during the measurements. The exposed area is measured using images taken with a digital optical microscope (Keyence VHX-5000). All electrochemical experiments are performed using a Biologic VSP-300 potentiostat supported by EC-Lab V11.36 software. The experimental setup is a three-electrode cell, using an Ag/AgCl/KCl (sat.) electrode as a reference electrode (RE), a platinum mesh as a counter electrode (CE), and the sample as the working electrode (WE). Prior to PDP measurement, the open circuit potential (OCP) is measured for 1.5 hours, at which steady-state is achieved. The potential scan rate is 0.167 mV/s from -200 mV vs. OCP until the breakdown potential. An aerated 3.5 wt% NaCl aqueous solution is used as the electrolyte, and measurements are carried out at room temperature (~20 °C). At least four repetitions are carried out to confirm the reproducibility of the experiments.

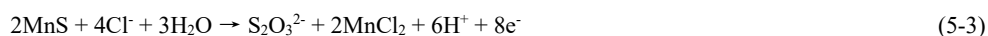
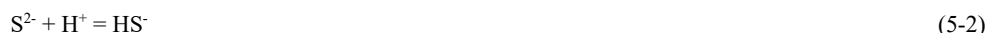
### 5.2.4 Ex-situ and In-situ Probe Microscopy Experiments

The SKPFM measurements are performed in the tapping mode using a Bruker Dimension Edge™ instrument with Nanoscope v8.05 software. A rectangular conductive cantilever (silicon pyramid single-crystal tip coated with PtIr5, SCM-Pit probe) is employed. Utilising the tapping mode, the surface topography signal is recorded in the first (or forward) scan. Then, the tip is lifted to 100 nm and the

Volta potential signal is recorded in the second (or backward) scan by following the topography contour in the first scan. All AFM/SKPFM measurements are performed at a scanning area of  $50 \times 50 \mu\text{m}^2$  with a scan rate of 0.3 Hz and a pixel resolution of  $512 \times 512$ . The raw data is analysed using Gwyddion 2.60 software.

The SECM measurements are carried out with the Scanning Electrochemical Workstation SCV370 model (Princeton Applied Research, AMETEK Inc.). The tip for measurements is glass-insulated, disk-shaped platinum microelectrode which is fabricated from  $10 \mu\text{m}$  diameter Pt wires (Sensolytics Inc.). An Ag/AgCl/KCl (sat.) is used as the reference electrode (RE), and a platinum wire as the counter electrode (CE). All the potentials in the experiments are referred to the RE. The SECM operating in Sample Generation/Tip Collection (SG/TC) mode is used. The experiments are carried out in a solution containing 10 mM KI as a mediator and 0.1M NaCl. The probe is polarised at 0.6 V to initiate the reaction of the mediator ( $\text{I}^-/\text{I}_3^-$ ). Maps are obtained at a scan rate of  $10 \mu\text{m/s}$  and a tip-sample distance of approximately  $5 \mu\text{m}$ . In the SECM measurement, the  $\text{I}^-/\text{I}_3^-$  redox mediator is used to detect the electroactivity over S-rich inclusions. The chemical/electrochemical reactions are summarised in the following equations [28-31].

#### *MnS Dissolution / Reduction*



#### *SECM Tip oxidation*



At the inclusion, MnS undergoes chemical or electrochemical dissolution to produce either hydrosulfide, as presented in reactions (5-1) and (5-2), or thiosulfate in reaction (5-3). To detect  $\text{HS}^-$  or  $\text{S}_2\text{O}_3^{2-}$ ,  $\text{I}_3^-$  generated at the SECM tip is reduced to  $\text{I}^-$  by either  $\text{HS}^-$  or  $\text{S}_2\text{O}_3^{2-}$ . Thus, the current at the SECM microelectrode is amplified in the presence of the dissolved sulfur species due to an increase of  $\text{I}^-$  at the microelectrode tip.

## 5.3 Results

### 5.3.1 Microstructure Characterisation

**Figure 5.2** shows the SEM microstructure after OPS polishing of the three alloys after Q&P treatment, respectively. XRD measurements show that there is a volume fraction of 0.11 retained austenite in alloy 2C LMn, and 0.22 in alloys 3C LMn and 3C HMn-NbTi. Retained austenite cannot

be distinguished in these SEM images. In alloys 2C LMn and 3C LMn, small black particles identified as MnS inclusions with sizes less than  $1\ \mu\text{m}$  embedded in the matrix are observed, as indicated in **Figures 5.2** (a) and (b) with red arrows. In alloy 3C HMn-NbTi, the microstructure contains MnS inclusions, NbC inclusions (white particles with sizes less than  $1\ \mu\text{m}$  in **Figure 5.2** (c)), and TiN inclusions (large rectangle and/or triangle with size up to  $10\ \mu\text{m}$  in **Figure 5.2** (d)). Ten random OM micrographs ( $173\ \mu\text{m} \times 130\ \mu\text{m}$ ) are taken from each sample to quantify the prior austenite grain size (PAGS) and the density of the above-mentioned small MnS inclusion. The PAGS of alloy 3C HMn-NbTi ( $21.7 \pm 4.1\ \mu\text{m}$ ) is smaller than that of alloys 2C LMn and 3C LMn ( $37.7 \pm 9.7\ \mu\text{m}$  and  $36 \pm 17\ \mu\text{m}$ , respectively), due to the grain refinement role of the precipitates formed from micro-alloying elements [17].

A semi-quantitative analysis of the density distribution of small MnS ( $< 1\ \mu\text{m}$ ) particles shows that the number of particles per  $\text{mm}^2$  is  $23 \pm 6$  in alloy 2C LMn,  $16 \pm 10$  in alloy 3C LMn, and  $2 \pm 1$  in alloy 3C HMn-NbTi. The NbC particles are out of the OM view, therefore the NbC is not quantified. Therefore, the inclusion (small MnS and NbC) density of alloy 3C HMn-NbTi should be higher than the statistical results above. In addition, elongated MnS inclusions with a length of  $10\ \mu\text{m}$  to  $100\ \mu\text{m}$  are also observed in all three alloys and are unevenly distributed, so they are not quantified either.

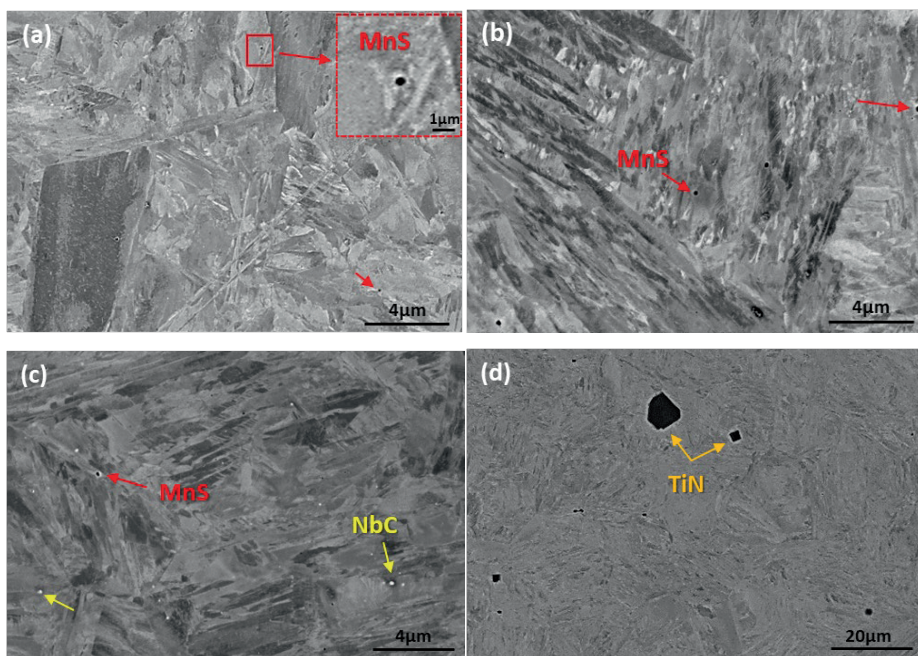


**Figure 5.2.** SEM images of three studied alloys (a) alloy 2C LMn, (b) alloy 3C LMn, (c) & (d) alloy 3C HMn-NbTi.

EDS analysis is performed on those particles, and representative EDS spectra are presented in the supplementary information (**Appendix**). The average chemical composition of similar particles in each sample is summarised in **Table 5.2**. For all three alloys, the ratio of Mn to S in the MnS inclusions is of approximately 1:1. The big particles with a characteristic square or triangle shape are identified as TiNb(N) particles. With negligible Nb content, the TiNb(N) particle represents TiN inclusion (**Appendix**).

**Table 5.2. Chemical composition of inclusions obtained from EDS in three alloys (at. %).**

Sample		Mn	S	Ti	Nb	N
Alloy 2C LMn	MnS	$16.3 \pm 5.9$	$15.5 \pm 4.9$	-	-	-
Alloy 3C LMn	MnS	$2.5 \pm 1.4$	$2.3 \pm 2.1$	-	-	-
Alloy 3C HMn-NbTi	MnS	$36.7 \pm 2.5$	$28.4 \pm 1.7$	-	-	-
	TiN	-	-	$51.4 \pm 0.4$	$0.8 \pm 0$	$46.3 \pm 1.6$

### 5.3.2 Chemical Composition of the Oxide Film by XPS Analysis

XPS analysis is conducted to obtain the chemical composition of the formed oxide layer on the pre-passivated samples. The XPS high-resolution survey scan showed that the passive film consists of the main elements Fe and Cr (**Figure 5.3**). The XPS high-resolution scans show intense signals of Fe2p<sub>3</sub> and Cr2p<sub>3</sub> peaks, which are the main elements constituting the passive film [44-47]. The XPS spectra of individual elements are deconvoluted into an optimum number of peaks based on their binding energies. The deconvoluted fitting results of Fe2p<sub>3</sub> and Cr2p<sub>3</sub> spectrums in all three alloys are displayed in **Figure 5.3**.

For all three samples, the Fe2p<sub>3</sub> spectra are composed of oxide peaks (FeO at ~ 709 eV and Fe<sub>2</sub>O<sub>3</sub> at ~ 711 eV) and a metal peak (Fe(0) at ~ 707 eV), coupled with a Fe-hydroxide peak FeOOH at ~ 713 eV [44,47,48]. Additionally, an extra satellite peak at ~ 715 eV is also present, which has been previously reported in the literature [49,50]. The Cr2p<sub>3</sub> spectra are composed of broad oxide peaks (Cr<sub>2</sub>O<sub>3</sub> at 576.5 eV, and CrO<sub>2</sub> at 575.4 eV) and metal peak (Cr at 573.6 eV), coupled with a small hydroxide peak (Cr(OH)<sub>3</sub> at 577.7 eV). The effect of MnS inclusion on the passive film of the sample surface has not been identified [51,52].

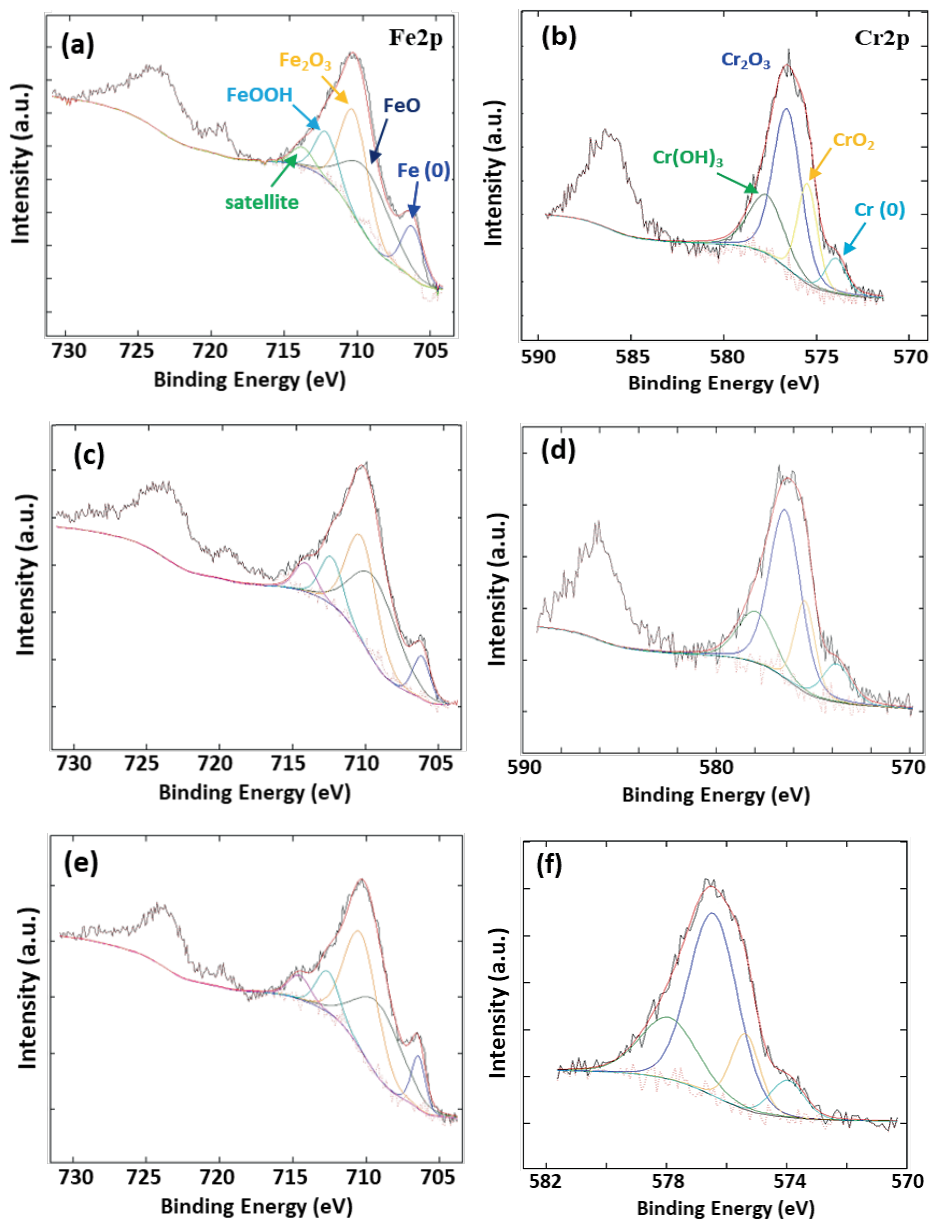


**Figure 5.3.** Deconvolution results of Fe2p and Cr2p spectra in alloy 2C LMn(a)(b), alloy 3C LMn(c)(d), and alloy 3C HMn-NbTi (e)(f), respectively.

The quantitative XPS analysis combines Fe/Cr ratio with a fraction of deconvoluted components (shown in **Figure 5.4**). Generally, the passive layer showed a high fraction of  $\text{Fe}_2\text{O}_3$  without significant differences between alloys for all three alloys. Alloys 2C LMn and 3C LMn have an almost identical

passive layer. Alloy 3C HMn-NbTi contains 10% less  $\text{Fe}_2\text{O}_3$  and 6% more Cr oxide. This might be caused by the grain size refinement (high tangled dislocation density) in alloy 3C HMn-NbTi, which provides fast diffusion channels for Cr, thereby a relatively homogeneous distribution of Cr, and consequently, more Cr oxide can be formed. Although the particle density of MnS inclusions in alloy 3C HMn-NbTi is lower than that of alloys 2C LMn and 3C LMn, there is no certain correlation between the component and particle density in the passive film of these three alloys.

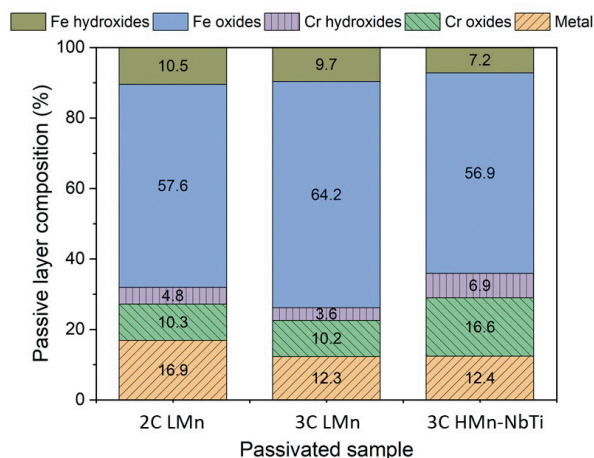


**Figure 5.4. Quantitative analysis of the composition of the oxide layer formed on the three alloys (2C LMn, 3C LMn, 3C HMn-NbTi) from the XPS fitting analysis.**

### 5.3.3 Electrochemical Characterisation

To assess the electrochemical behaviour of the samples, OCP and potentiodynamic polarisation experiments are performed in an aerated 3.5 wt.% NaCl solution. Representative results are presented in **Figures 5.5** (a) and (b), respectively. The OCP values are measured for 1.5 hours to ensure a stable value. From the curves in **Figure 5.5** (a), all samples have a potential that steadily increases with time, suggesting the formation of the passive film on the sample surface. Curves shown in **Figure 5.5** (a) are representative among the five repetitions for each sample.

Potentiodynamic polarisation gives insight into the kinetics of the corrosion process and the pitting resistance of the samples. From the curves in **Figure 5.5** (b), all samples exhibit the immediate formation of the passive region followed by a breakdown at higher potential. The current density increases drastically, indicating that the passive film has failed and pitting is detected on the sample surface. For alloys 2C LMn and 3C LMn, the passive region shows a stable current density. Alloy 3C HMn-NbTi shows transients in the current density, indicating the presence of metastable pitting during

polarisation. Furthermore, alloy 3C HMn-NbTi exhibits an earlier breakdown of the passive region compared to alloys 2C LMn and 3C LMn.

For a quantitative comparison of the corrosion performance of the three alloys, the corrosion current density ( $i_{\text{corr}}$ ), pitting potential ( $E_{\text{pit}}$ ), and potential range of the passive region ( $E_{\text{pit}} - E_{\text{corr}}$ ) are extracted and plotted in **Figures 5.5** (c) and (d). The corrosion current density values, shown in **Figure 5.5** (c), did not exhibit a significant difference between the samples considering the average value and scatter. No relation can be concluded between the different compositions or microstructure (phase fraction or inclusions). Overall, the three alloys showed very low current density (order  $10^{-8}$  A/cm<sup>2</sup>) which is expected for these types of stainless steels [14]. **Figure 5.5** (d) shows the passive region and the pitting potential for each alloy. Alloys 2C LMn and 3C LMn show wider range of passivity compared to alloy 3C HMn-NbTi.

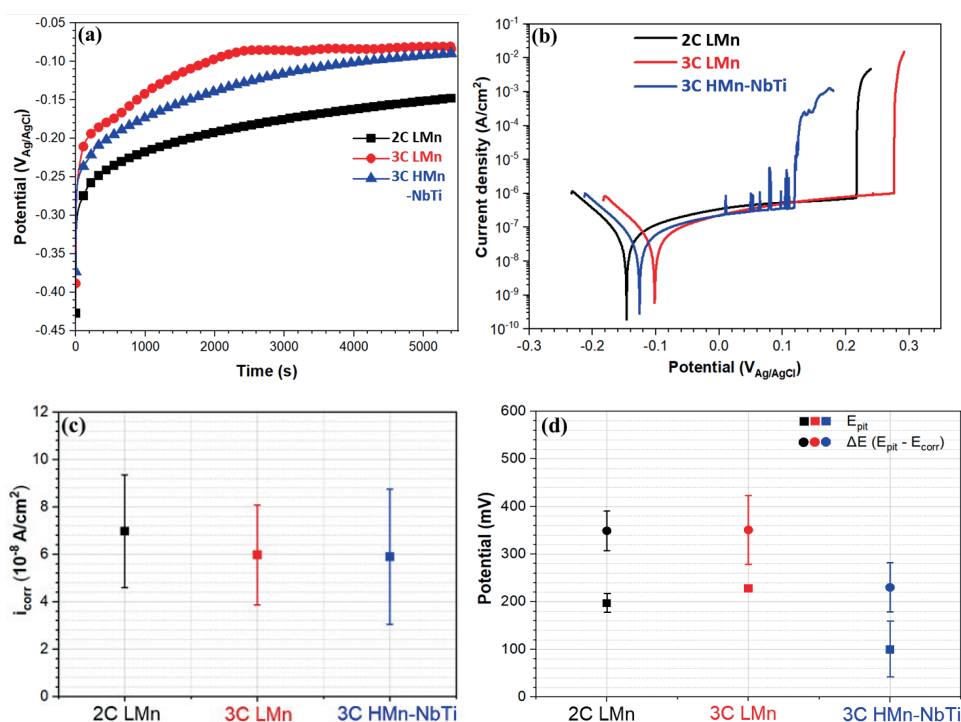


**Figure 5.5.** Representative (a) OCP and (b) potentiodynamic polarisation curves of the three different alloys. The average values of (c) corrosion current density obtained by Tafel extrapolation and (d) pitting potential ( $E_{\text{pit}}$ ) and passive region ( $\Delta E$ ). Experiments are repeated at least four times to confirm reproducibility.

### 5.3.4 Surface Potential Characterisation by SKPFM

The topography and surface potential maps of the matrix for the three alloys are obtained by AFM/SKPFM measurements. The resulting maps are shown in **Figure 5.6**. The dashed line in the maps highlights some selected martensite laths, which are visible in the topography maps (**Figures 5.6** (a), (d), and (g)). Samples are polished with OPS, which led the hard martensite phase (laths) to stand out from the surface, showing a higher height and brighter colour on the topography map than the austenite. In contrast, the retained austenite phase is relatively softer, showing dark colour on the topography map. The Volta potential maps are displayed in **Figures 5.6** (b), (e), and (h). Selected line scans corresponding to both topography and Volta potential are displayed in **Figures 5.6** (c), (f), and (i). Volta potential maps are plotted using the same potential scale for better comparison between the samples and to enhance the differentiation between martensite and austenite.

The potential maps reveal that martensite laths of all three alloys show lower potential compared to the austenite (darker). The line scan obtained from the marked martensite laths clearly shows topography peaks coinciding with potential drops. Among the entire scanning region, alloy 2C LMn has Volta potential ranges from 8 mV to 20 mV; in alloy 3C LMn, the potential range is similar to alloy 2C LMn, ranging from 8 mV to 16 mV. In alloy 3C HMn-NbTi, the Volta potential ranges from 10 mV to 25 mV. The maximum potential difference between phases of the matrix is 15 mV. Generally, regions exhibiting lower surface potential values (directly linked to work function energy) are more prone to preferential dissolution or corrosion susceptibility than the matrix [53]. Therefore, the martensite in these three alloys may have all the preferential dissolution points when exposed to the corrosive environment.

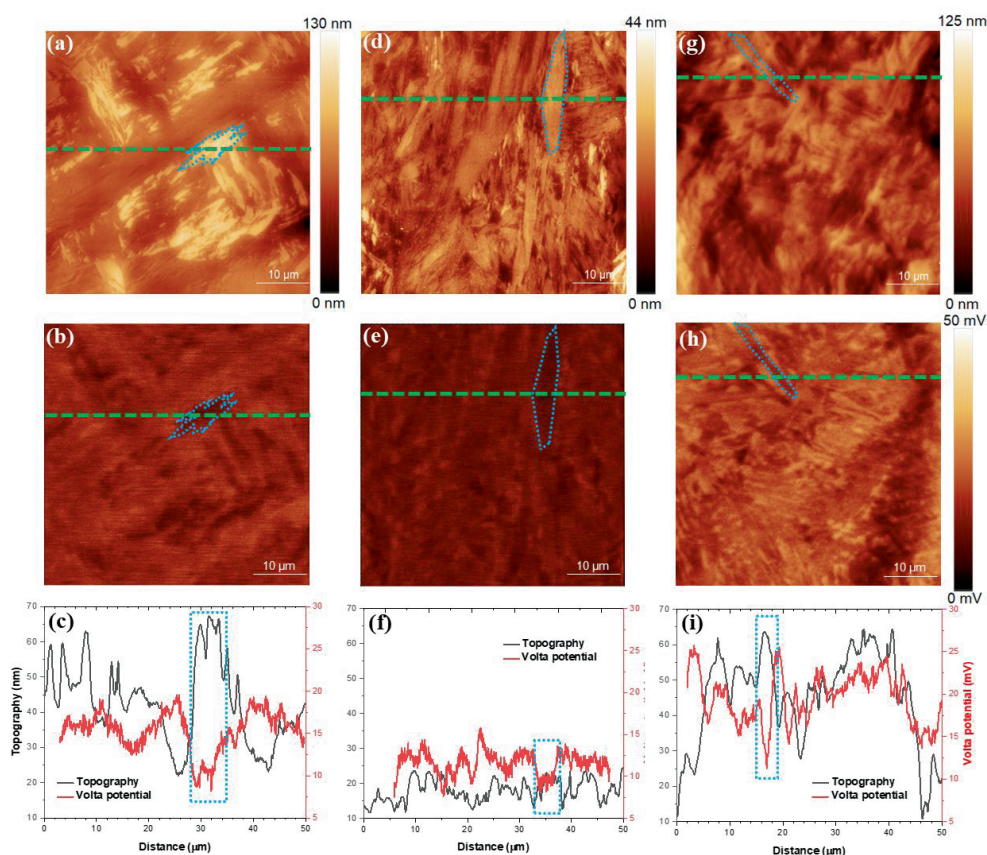


**Figure 5.6.** Topography map, Volta-potential map, and extracted line profiles of the matrix without inclusions for (a)-(c) alloy 2C LMn, (d)-(f) alloy 3C LMn, and (g)-(i) alloy 3C HMn-NbTi, respectively.

Instead of the ideal Q&P microstructures containing retained austenite and martensite only, inclusions are also observed in the investigated heat-treated microstructures, especially MnS and TiN inclusions. SKPFM maps of the MnS inclusions in the three specimens are shown in **Figure 5.7**. **Figures 5.7** (a), (e), and (i) display the SEM image of elongated MnS inclusion on the sample surface of each alloy, while the topography maps in **Figures 5.7** (b), (f), and (j) show corresponding size and morphology. **Figures 5.7** (c), (g), and (k) display the Volta potentials maps of the three alloys. MnS inclusions show a lower Volta potential than the matrix. Line scans over the MnS inclusions are shown in **Figures 5.7** (d), (h), and (l), displaying potential differences of up to 35 mV are measured across MnS in alloy 2C LMn, 40 mV in alloy 3C LMn, and 30 mV in alloy 3C HMn-NbTi. The potential difference measured over the MnS inclusion is greater than the difference observed between phases (maximum 15 mV in **Figure 5.6**). This indicates that the effect of inclusion is more dominant than phase fractions. Moreover, the Volta potential maps show local differences in the particles.

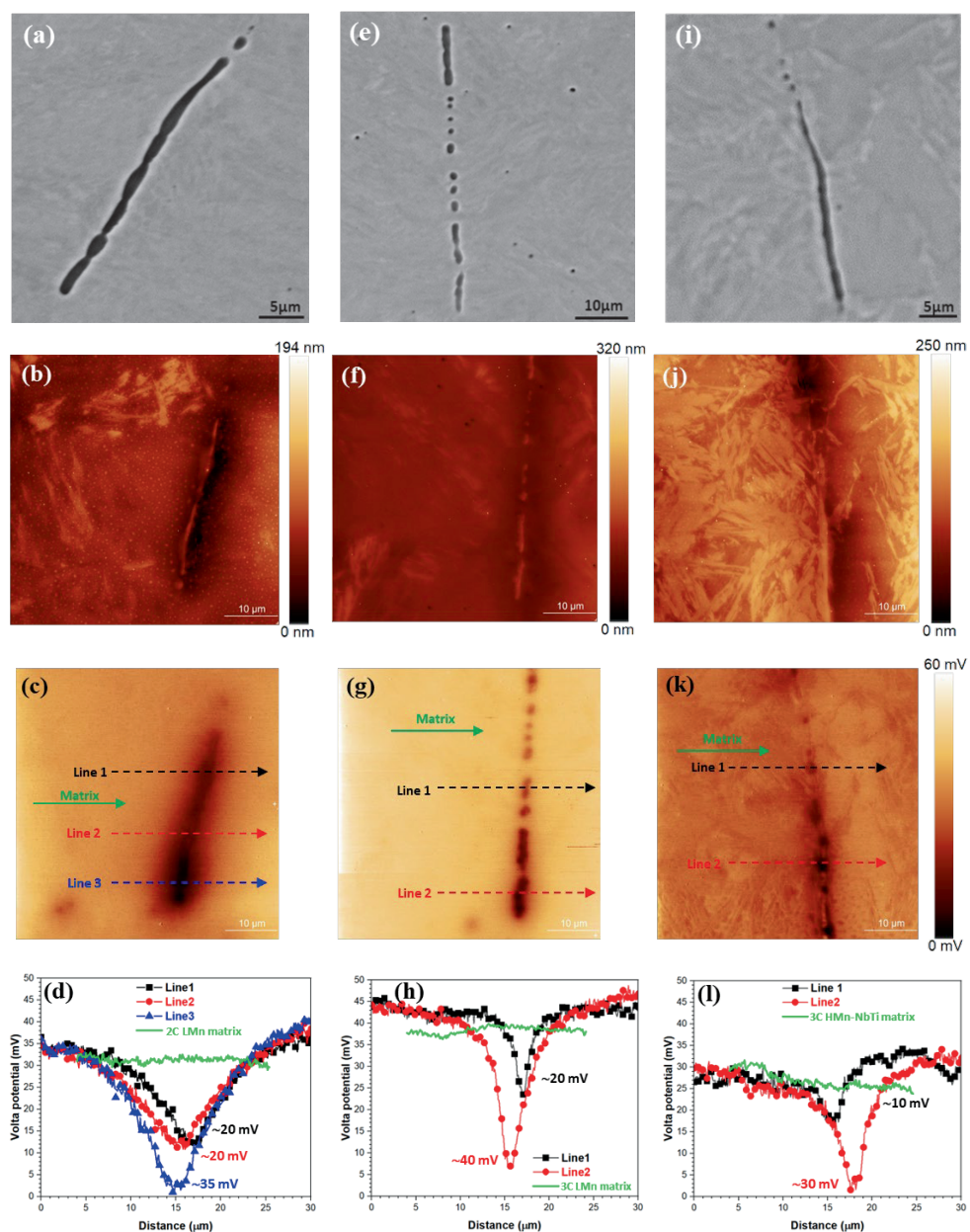


**Figure 5.7.** SEM images, topography and Volta-potential maps, and corresponding surface potential line profiles of elongated MnS inclusions in (a-d) alloy 2C LMn, (e-h) alloy 3C LMn, and (i-l) alloy 3C HMn-NbTi.

**Figure 5.8** presents the SEM/EDS and SKPFM maps of micro-alloying TiN inclusion on the surface of alloy 3C HMn-NbTi. Contrary to the MnS inclusions, TiN inclusion has a much greater Volta

potential value than the matrix, a difference of above 40 mV. This surface potential value implies a lower electrochemical activity of TiN than the matrix during exposure to electrolytes. Previous studies on interstitial-free steels, which have a ferritic matrix with a body-centered cubic (BCC) crystal structure and a low carbon content, have reported that TiN inclusions exhibit cathodic behaviour [41,42,54], and the potential difference is the driving force for galvanic corrosion to occur at the surrounding matrix.

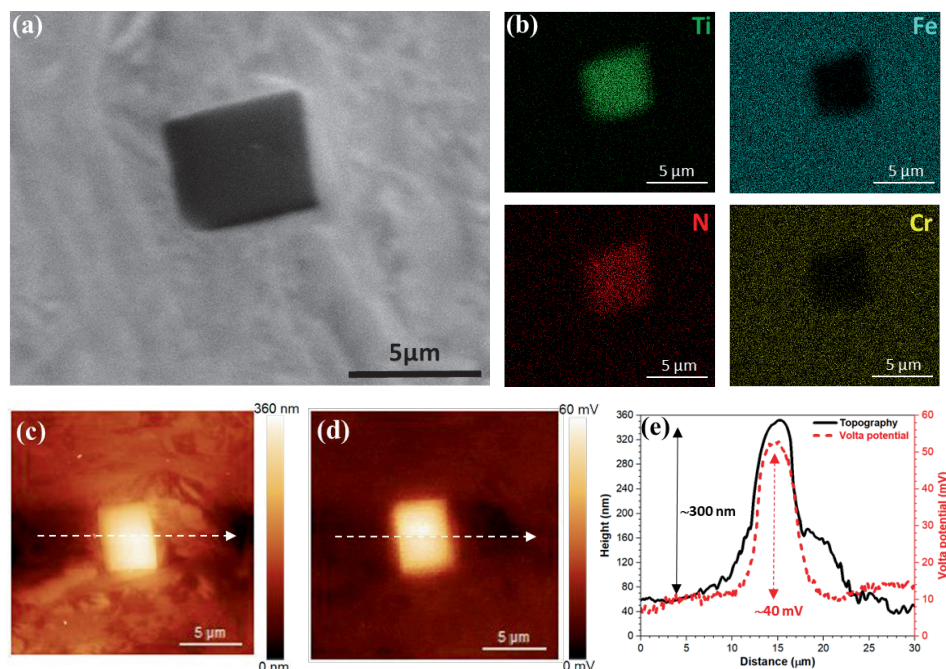


**Figure 5.8.** (a) SEM, (b) EDS, (c) topography, (d) Volta potential maps, and (e) corresponding surface potential line profiles of NbTi-riched inclusion in alloy 3C HMn-NbTi.

Round particle inclusions of MnS and NbC with dimensions less than 1  $\mu\text{m}$ , such as the ones shown in **Figure 5.2**, are not detected by topography or Volta potential maps. Due to the existence of large ( $> 10 \mu\text{m}$ ) MnS and TiN inclusions, the round particle inclusions in such a small size do not cause a detectable effect.

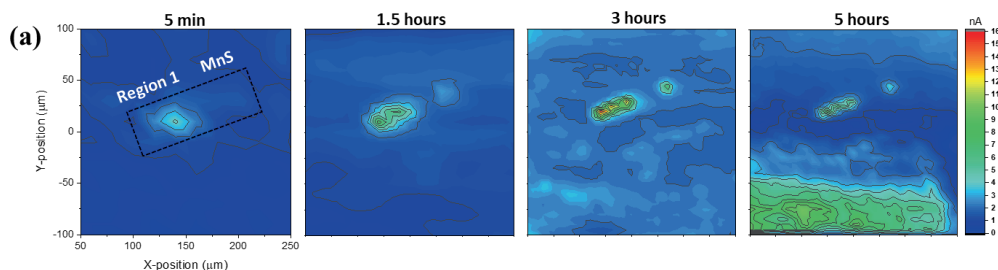
### 5.3.5 In situ Electrochemical Measurements by SECM

Both SKPFM and PDP analyses indicated that MnS and TiN inclusions may decline the corrosion performance of these alloys due to localised corrosion attacks. However, there is still a lack of direct evidence. Therefore, SECM measurements are performed to monitor the local electrochemical activity of inclusions. A large MnS inclusion is marked by indents (hardness tester indentation pit as positioning

point) in alloy 2C LMn, and a MnS inclusion with a nearby TiN inclusion is marked in alloy 3C HMn-NbTi. **Figure 5.9** shows SECM mappings operating in SG/TC mode on the surface of alloys 2C LMn and 3C HMn-NbTi during immersion in 0.1 M NaCl.

The SECM maps clearly shows the variation of the current peak with the increase of the immersion times. For alloy 2C LMn (region 1), **Figure 5.9** (a), the immersion time is of only 5 minutes. The current pointed by the black arrow corresponding to the MnS inclusion of  $\sim 4$  nA indicates that the dissolution of the MnS inclusion starts immediately. After 1.5 hours, the peak current is  $\sim 8$  nA. After 3 hours of immersion, the peak current is measured of  $\sim 15.5$  nA, indicating the fastest dissolution rate of the MnS inclusion. The higher current indicates deletion of  $S^-$  in solution. After immersion for 5 hours, the peak current starts decreasing to  $\sim 7$  nA, when the dissolution process slows down. The indents marked area includes a long MnS inclusion of about  $100 \mu\text{m}$  (region 2) and three TiN particles (region 3). For alloy 3C HMn-NbTi, **Figure 5.9** (b), in 5 minutes, the SECM peak current of the big MnS inclusion reached  $\sim 4$  nA. After immersion for 1 hour, the peak current increased to  $\sim 6$  nA, and after immersion for 2 hours, the peak current increased to  $\sim 21$  nA. Then, it dropped to  $\sim 5$  nA after immersion for 4 hours and remained constant until the end of the measurement (6 hours). After 6 hours, **Figure 5.9** (b) showed a strong signal around hardness indents. The dissolution rate in alloy 3C HMn-NbTi (two hours from 4 to 21 nA) is faster than in alloy 2C LMn (three hours from 4 nA to 16 nA). This explains the earlier pitting initiation, i.e. the lower pitting potential in alloy 3C HMn-NbTi that is observed in PDP curves.

**Figures 5.9** (c) and (d) present the OM images of both alloys after the SECM measurements. In both samples, the MnS inclusion is still present. Post-SECM EDS analysis confirmed the presence of S at the MnS sites, as shown in the OM images of **Figures 5.9** (c) and (d). From region 3, the OM image shows clearly the remaining TiN inclusion, and one side of its surrounding matrix is corroded. This is in agreement with the surface potential results. NbC particles precipitate and epitaxially grow on the pre-existing TiN particles, forming a so-called "core-shell" configuration [18,33], becoming preferable sites for dissolution.



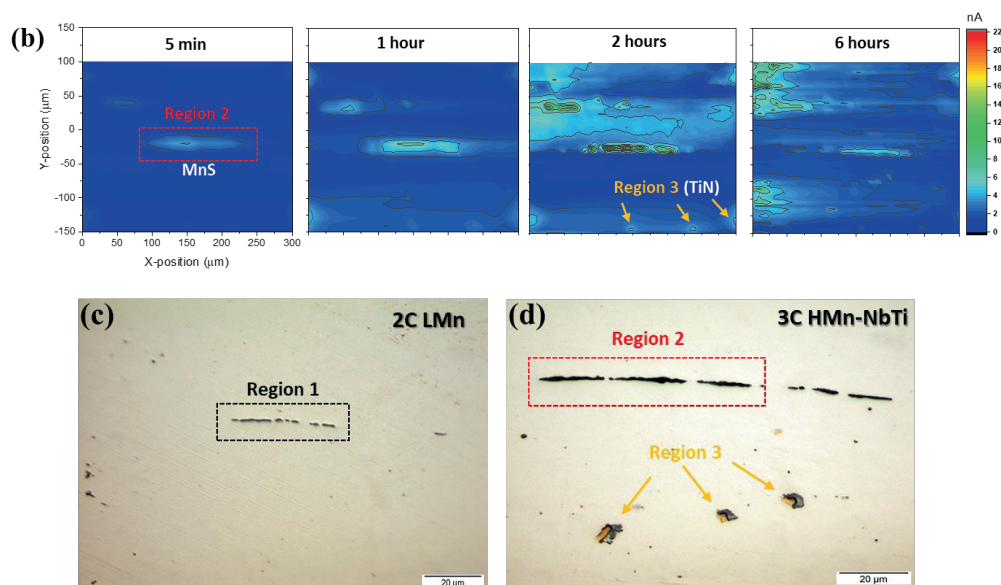


**Figure 5.9.** Electrochemical current maps with an immersion time of alloys 2C LMn (a) and 3C HMn-NbTi (b), and OM images after SECM measurements of alloy 2C LMn (c) and alloy 3C HMn-NbTi (d), respectively. In alloys 2C LMn and 3C HMn-NbTi, the scanning areas are  $200 \times 200 \mu\text{m}^2$  and  $300 \times 250 \mu\text{m}^2$ , respectively.

## 5.4 Discussion

The comparison between the corrosion performance of alloys 2C LMn and 3C LMn provides information regarding the effect of carbon content. The difference in chemical composition and quenching temperature leads to the difference in phase fractions with higher retained austenite in alloy 3C LMn. Despite this, the SEM observation and XPS analysis indicated that these two alloys have similar microstructural characteristics (**Figure 5.2**) and passive layer constituents (**Figures 5.3** and **5.4**). As a result, the corrosion properties based on pitting potentials do not explicitly show a difference (**Figure 5.5**). Alloys 3C LMn and 3C HMn-NbTi have the same carbon content and equal phase fractions of retained austenite. However, alloy 3C HMn-NbTi exhibits the lowest  $E_{\text{pit}}$  value and the lowest passive region (in **Figure 5.5** (d)). **Figures 5.5** (b) and (d) show that the addition of Mn, Nb and Ti makes the alloy more susceptible to pitting corrosion, which can be attributed to the existence of MnS and/or TiN inclusions, as observed in **Figure 5.2**. As discussed in the literature [14,18,20], the presence of inclusions significantly influences the properties of the native or electrochemically formed passive layer. Not only will they influence the formation and stability of the oxide (e.g. composition, electrochemical properties, semi-conductor properties), but they also can play a crucial role in the initiation of localised corrosion such as pitting corrosion [55]. The Volta potential maps in **Figures 5.6** – **5.8** confirmed that the potential difference between inclusion and matrix is more pronounced than

between martensite and retained austenite, which confirms that the inclusions play a dominant influencing role even in multiphase Q&P steels.

MnS round particles are observed with sizes less than 1  $\mu\text{m}$  in diameter in the three alloys. Alloy 3C HMn-NbTi also contains NbC particles of the same size. They are fairly distributed in the microstructures, as shown in **Figure 5.2**, and no difference in electrochemical behaviour among these micro-scale MnS particles is observed. Some of the MnS particles are present in elongated shapes with sizes of up to 100  $\mu\text{m}$ . It is found that these long MnS inclusions can lead to the defection of passive film, which has been barely reported [48,51,52].

The elongated MnS inclusions are present in all three alloys, but only alloy 3C HMn-NbTi showed transients of current density in potentiodynamic polarisations (**Figure 5.5** (b)), indicating that the metastable pitting and the earlier breakdown in alloy 3C HMn-NbTi are related to its unique TiN inclusion [58-60]. **Figures 5.7** and **5.8** show that the MnS inclusions have lower surface potential than the matrix, while the TiN site has much higher surface potential than the matrix. Therefore, these differences in surface potential values drive a selective dissolution of the matrix (in the case of TiN) or dissolution of MnS.

**Figure 5.10** illustrates schematically the pit initiation mechanism at inclusions in alloys 2C LMn and 3C LMn (**Figure 5.10** (a)) and alloy 3C HMn-NbTi (**Figure 5.10** (b)).

- **Pit initiation in presence of MnS inclusion (alloys 2C LMn and 3C LMn).** The initial microstructure (stage 1) displays the matrix with one MnS inclusion on the sample surface. The existence of inclusion makes the passive film discontinuous because of the different constituents (**Figure 5.4**). Stage 2 involves the exposition to a corrosive environment, in which the passive film and the MnS inclusion start dissolving and release sulphur species, which is detected by the SECM (**Figure 5.9**). This is driven by its 35 mV lower surface potential with respect to the matrix (**Figure 5.7**). The dissolution process of MnS (stage 3) produces sulphur (S) that decomposes on the sample surface, which is detected after the SECM test. The decrease in current may be related to the S decomposition on the sample surface.
- **Pit initiation in presence of both MnS and TiN inclusions (alloy 3C HMn-NbTi).** The initial microstructure (stage 1) illustrates more discontinuity and less heterogeneity of passive film. The MnS inclusion displays the same behaviour as that in alloys 2C LMn and 3C LMn. The well-known MnS inclusion triggered localised corrosion in austenitic stainless steels [21-31] still applies in Q&P processed multiphase steels. Dissolution of MnS inclusion and trenching of the TiN/matrix interface occurs, as shown in stage 2; this is driven by the 40 mV surface potential difference. When the trench grows deeper (stage 3), a stable pit forms and this explains the lower pitting potential in alloy 3C HMn-NbTi. Dissolution of MnS, and the trenching

around the TiN may lead to pitting or repassivation - in overall all of this makes alloy 3C HMn-NbTi more susceptible to localised attack.

The effect of TiN inclusions on corrosion performance has been widely investigated [41,42,57,58]. In austenitic stainless steels with an FCC structure and high C, Cr, and Ni content, TiN inclusions (often co-present with TiN-Ca complex inclusions) are found to have no effect on pitting performance [57,58]. However, in ferritic steels with a BCC structure, the TiN inclusion-induced pitting corrosion mechanism is well explained [41,42]. Step-like corrosion pits induced by TiN inclusions are observed using in situ techniques. These observations reveal that pitting corrosion initiates at the interface between the inclusion and the matrix [41,42], progressing through initiation, transition, and propagation stages, as summarised in previous studies [41]. The SECM measurement and microstructure observation in **Figure 5.9** (b) and (d) confirmed that the TiN inclusion-induced corrosion mechanism can be extended to the multiphase Q&P processed martensitic stainless steels.

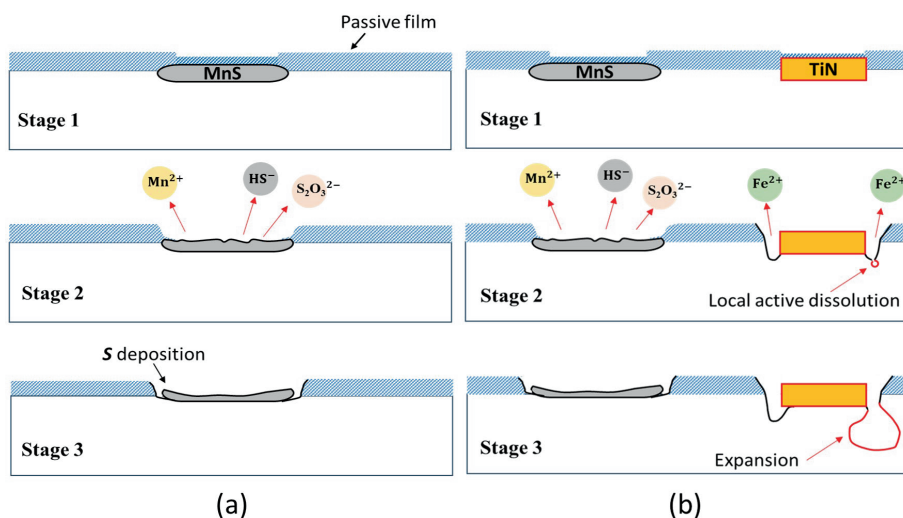


**Figure 5.10.** Schematic illustration of the pit initiation mechanism at MnS and TiN inclusions in alloys 2C LMn and 3C LMn (a), and alloy 3C HMn-NbTi (b), respectively.

In addition, microalloying elements refined the prior austenite grain size in alloy 3C HMn-NbTi, which further decreased its corrosion resistance because grain boundaries act as active sites promoting the metal dissolution and decreasing the stability of the passive layer on the sample surface [59,60].

## 5.5 Conclusions

The effect of chemical composition and microstructure on the corrosion resistance of Q&P produced martensitic stainless steels is evaluated. Particularly, the combined effect of C-enriched austenite, C-depleted martensite and inclusions on the corrosion mechanisms is investigated by combining ex-situ and in-situ electrochemical techniques. The following conclusions are drawn.

- The corrosion resistance of Q&P steels is controlled mainly by the presence of inclusions, while chemical composition and phase fractions play a less prominent role. The strong influence of the inclusions is confirmed through SKPFM and potentiodynamic polarisation.
- The alloy displaying TiN and MnS inclusions displayed the worst corrosion resistance. The higher Mn content and grain refinement also contribute to this low corrosion performance.

## References

- [1] D.K. Matlock, J.G. Speer, Third generation of AHSS: microstructure design concepts, *Microstructure and Texture in Steels*, (2009)185 – 205. [https://doi.org/10.1007/978-1-84882-454-6\\_11](https://doi.org/10.1007/978-1-84882-454-6_11)
- [2] X. Hu, Z. Feng, Advanced high strength steel – basics and applications in the automotive industry. Report (2021). <https://doi.org/10.2172/1813170>
- [3] S. Vögele, M. Grajewski, K. Govorukha, D. Rübhelke, Challenges for the european steel industry: analysis, possible consequences and impacts on sustainable development. *Applied Energy*, 264 (2020) 114633. <http://dx.doi.org/10.1016/j.apenergy.2020.114633>
- [4] J.G. Speer, A.M. Streicher, D.K. Matlock, F. Rizzo, G. Krauss, Quenching and partitioning: a fundamentally new process to create high strength trip sheet microstructures. *The Iron & Steel Society*, (2003) 505–522.
- [5] J.G. Speer, D.K. Matlock, B.C. De Cooman, J.G. Schroth, Carbon partitioning into austenite after martensite transformation. *Acta Materialia*, 51 (2003) 2611–2622. [https://doi.org/10.1016/S1359-6454\(03\)00059-4](https://doi.org/10.1016/S1359-6454(03)00059-4)
- [6] J.G. Speer, F. Rizzo, D.K. Matlock, D.V. Edmonds, The “quenching and partitioning” process: background and recent progress. *Materials Research*, 8 (2005) 417–423. <http://dx.doi.org/10.1590/S1516-14392005000400010>
- [7] M. Hillert, J. Argen, On the definitions of paraequilibrium and orthoequilibrium. *Scripta Materialia*, 50 (2004) 697–699. <https://doi.org/10.1016/j.scriptamat.2003.11.020>
- [8] J.G. Speer, D.K. Matlock, L. Wang, D.V. Edmonds, Quenched and partitioned steels. *Comprehensive Materials Processing*, 1 (2014) 217 – 225. <https://doi.org/10.1016/B978-0-08-096532-1.00116-3>
- [9] J.G. Speer, E. De Moor, A.J. Clarke, Critical assessment 7: quenching and partitioning. *Materials Science and Technology*, 31 (2015) 3 – 9. <https://doi.org/10.1179/1743284714Y.0000000628>
- [10] L. Wang, J.G. Speer, Quenching and partitioning steel heat treatment. *Metallography, Microstructure, and Analysis*, 2 (2013) 268 – 281. <https://doi.org/10.1007/s13632-013-0082-8>
- [11] L. Yuan, D. Ponge, J. Wittig, P. Choi, J.A. Jiménez, D. Raabe, Nanoscale austenite reversion through partitioning, segregation and kinetic freezing: Example of a ductile 2 GPa Fe–Cr–C steel. *Acta Materialia*, 60 (2012) 2790–2804, <https://doi.org/10.1016/j.actamat.2012.01.045>
- [12] Q.L. Huang, C. Schröder, H. Biermann, O. Volkova, J. Mola, Influence of martensite fraction on tensile properties of quenched and partitioned (Q&P) martensitic stainless steels. *Steel Research International*, 87 (2016) 1082–1094. <https://doi.org/10.1002/srin.201500472>
- [13] T. Tsuchiyama, J. Tobata, T. Tao, N. Nakada, S. Takaki, Quenching and partitioning treatment of a low-carbon martensitic stainless steel. *Materials Science and Engineering: A*, 532 (2012) 585–592. <https://doi.org/10.1016/j.msea.2011.10.125>

- [14] S.Y. Lu, K.F. Yao, Y.B. Chen, M.H. Wang, N. Chen, X.Y. Ge, Effect of quenching and partitioning on the microstructure evolution and electrochemical properties of a martensitic stainless steel. *Corrosion Science*, 103 (2016) 95–104. <https://doi.org/10.1016/j.corsci.2015.11.010>
- [15] J. Tobata, K.L. Ngo-Huynh, N. Nakada, T. Tsuchiyama, S. Takaki, Role of silicon in quenching and partitioning treatment of low-carbon martensitic stainless steel. *ISIJ International*, 52 (2012) 1377–1382. <https://doi.org/10.2355/isijinternational.52.1377>
- [16] G. Luo, H.Y. Li, Y.G. Li, J.Q. Mo, Microstructures and properties of a low-carbon-chromium ferritic stainless steel treated by a quenching and partitioning process. *Materials*, 12 (2019) 1704. <https://doi.org/10.3390/ma12101704>
- [17] A. Sierra-Soraluce, G. Li, M.J. Santofimia, J.M. Molina-Aldareguia, A. Smith, M. Muratori, I. Sabirov, Effect of microstructure on tensile properties of quenched and partitioned martensitic stainless steels' *Materials Science and Engineering: A*, 864(2023)144540. <https://doi.org/10.1016/j.msea.2022.144540>
- [18] J.L. Yang, Y.F. Lu, Z.H. Guo, J.F. Gu, C.X. Gu, Corrosion behaviour of a quenched and partitioned medium carbon steel in 3.5wt.% NaCl solution. *Corrosion Science*, 130(2018) 64-75. <https://doi.org/10.1016/j.corsci.2017.10.027>
- [19] T. Mehner, R. Morgenstern, P. Frint, I. Scharf, M. F-X Wagner, T. Lampke, Corrosion characteristics of a quenching and partitioning steel determined by electrochemical impedance spectroscopy. *IOP Conference Series: Materials Science and Engineering*, 373(2018) 012003. <https://doi.org/10.1088/1757-899X/373/1/012003>
- [20] S.K. Bonagani, V. Bathula, V. Kain, Influence of tempering treatment on microstructure and pitting corrosion of 13 wt.% Cr martensitic stainless steel. *Corrosion Science*, 131(2018) 340 – 354. <https://doi.org/10.1016/j.corsci.2017.12.012>
- [21] K. Eguchi, Quantitative analysis of initiation site of pitting corrosion on type 304 austenitic stainless steel. *Corrosion Science*, 221(2023) 111312. <https://doi.org/10.1016/j.corsci.2023.111312>
- [22] Z. Duan, C. Man, H. Cui, Z. Cui, X. Wang, Formation mechanism of MnS inclusion during heat treatments and its influence on the pitting behavior of 316L stainless steel fabricated by laser powder bed fusion. *Corrosion Communications*, 7(2022) 12 – 22. <https://doi.org/10.1016/j.corcom.2022.04.002>
- [23] X. Huang, W. Qiu, B. Niu, X. Zou, L. Pan, C. T. Kwok, Role of complex nonmetallic inclusions on the localized corrosion resistance of wire arc additively manufactured super duplex stainless steel. *Journal of Materials Research and Technology*, 28(2024) 799 – 813. <https://doi.org/10.1016/j.jmrt.2023.12.072>

- [24] T. Suter, H. Böhni, A new microelectrochemical method to study pit initiation on stainless steels. *Electrochimica Acta*, 42(1997) 3275-3280. [https://doi.org/10.1016/S0013-4686\(70\)01783-8](https://doi.org/10.1016/S0013-4686(70)01783-8)
- [25] E.G. Webb, T. Suter, R.C. Alkire, Microelectrochemical measurements of the dissolution of single MnS inclusions, and the prediction of the critical conditions for pit initiation on stainless steel. *Journal of The Electrochemical Society*, 148 (2001) B186–B195. <https://doi.org/10.1149/1.1360205>
- [26] P. Schmuki, H. Hildebrand, A. Friedrich, S. Virtanen, The composition of the boundary region of MnS inclusions in stainless steel and its relevance in triggering pitting corrosion. *Corrosion Science*, 47 (2005) 1239–1250. <https://doi.org/10.1016/j.corsci.2004.05.023>
- [27] A. Chiba, I. Muto, Y. Sugawara, N. Hara, Pit initiation mechanism at MnS inclusions in stainless steel: synergistic effect of elemental sulfur and chloride ions. *Journal of The Electrochemical Society*, 160 (2013) C511–C520. <http://dx.doi.org/10.1149/2.081310jes>
- [28] C.H. Paik, H.S. White, R.C. Alkire, Scanning electrochemical microscopy detection of dissolved sulfur species from inclusions in stainless steel. *Journal of The Electrochemical Society*, 147(2000) 4120-4124. <http://dx.doi.org/10.1149/1.1394028>
- [29] T.E. Lister, P.J. Pinhero, The effect of localised electric fields on the detection of dissolved sulfur species from Type 304 stainless steel using scanning electrochemical microscopy. *Electrochimica Acta*, 48(2003) 2371-2378. [https://doi.org/10.1016/S0013-4686\(03\)00228-7](https://doi.org/10.1016/S0013-4686(03)00228-7)
- [30] Y.H. Yin, L. Niu, M. Lu, W.K. Guo, S.H. Chen, In situ characterisation of localised corrosion of stainless steel by scanning electrochemical microscope. *Applied Surface Science*, 255(2009) 9193-9199. <http://dx.doi.org/10.1016/j.apsusc.2009.07.003>
- [31] M. Zhao, Z.H. Qian, Q.J. Qin, J.Y. Yu, Y.J. Wang, L. Niu, In situ SECM study on concentration profiles of electroactive species from corrosion of stainless steel. *Corrosion Engineering Science and Technology*, 48(2013) 270-275. <http://dx.doi.org/10.1179/1743278212Y.0000000066>
- [32] M. Charleux, W.J. Poole, M. Militzer, A. Deschamps, Precipitation behavior and its effect on strengthening of an HSLA-Nb/Ti steel. *Metallurgical and Materials Transactions A*, 32(2001) 1635–1647. <http://dx.doi.org/10.1007/s11661-001-0142-6>
- [33] I. Gutiérrez, effect of microstructure on the impact toughness of Nb-microalloyed steel: Generalisation of existing relations from ferrite–pearlite to high strength microstructures. *Materials Science and Engineering: A*, 571 (2013) 57-67. <http://dx.doi.org/10.1016/j.msea.2013.02.006>
- [34] X.J. Liu, J.C. Yang, C.K. Cai, A.X. Li, X. Lei, C.Q. Yang, Effect of microalloyed elements M (M = Ce, Ti, V, and Nb) on mechanical properties and electronic structures of  $\gamma$ -Fe: Insights from a first-principles study. *Steel research international*, 92 (2021) 2100053. <https://doi.org/10.1002/srin.202100053>
- [35] J. Webel, H. Mohrbacher, E. Detemple, D. Britz, F. Mücklich, Quantitative analysis of mixed niobium-titanium carbonitride solubility in HSLA steels based on atom probe tomography and

- electrical resistivity measurements. *Journal of Materials Research and Technology*, 18(2022) 2048-2063. <http://dx.doi.org/10.1016/j.jmrt.2022.03.098>
- [36] Y. Zou, Y. Han, H.S. Liu, H.X. Teng, M.S. Qiu, F. Yang, Microstructure evolution and enhanced mechanical properties of a novel Nb-Ti micro-alloyed medium-Mn steel. *Materials Characterization*, 187(2022) 111828. <https://doi.org/10.1016/j.matchar.2022.111828>
- [37] Y.J. Zhang, G. Miyamoto, T. Furuhashi, Enhanced hardening by multiple microalloying in low carbon ferritic steels with interphase precipitation. *Scripta Materialia*, 212(2022) 114558. <https://doi.org/10.1016/j.scriptamat.2022.114558>
- [38] J.B. Tan, X.Q. Wu, E.H. Han, W. Ke, X.Q. Liu, F.J. Meng, X.L. Xu, Role of TiN inclusion on corrosion fatigue behavior of Alloy 690 steam generator tubes in borated and lithiated high temperature water. *Corrosion Science*, 88(2014) 349-359. <https://doi.org/10.1016/j.corsci.2014.07.059>
- [39] D.H. Hur, J.H. Han, U.C. Lee, Y.S. Park, Microchemistry of Ti-Carbonitrides and their role in the early stage of pit initiation of alloy 600. *Corrosion*, 62(2006) 591-597. <https://doi.org/10.5006/1.3280673>
- [40] M.B. Leban, R. Tisu, The effect of TiN inclusions and deformation-induced martensite on the corrosion properties of AISI 321 stainless steel. *Engineering Failure Analysis*, 33(2013)430-438. <https://doi.org/10.1016/j.engfailanal.2013.06.021>
- [41] H. Chen, L. Lu, Y.H. Huang, X.G. Li, Insight into TiN inclusion induced pit corrosion of interstitial free steel exposed to aerated NaCl solution. *Journal of Materials Research and Technology*, 13(2021) 13-24. <https://doi.org/10.1016/j.jmrt.2021.04.046>
- [42] P. Liu, Q.H. Zhang, Y. Watanabe, T. Shoji, F.H. Cao, A critical review of the recent advances in inclusion-triggered localised corrosion in steel. *npj Materials Degradation*, 6 (2022) 81. <https://doi.org/10.1038/s41529-022-00294-6>
- [43] G. Li, C. Kwakernaak, A. Smith, M. Muratori, Y. Gonzalez-Garcia, M. J. Santofimia, Microstructure development of quenching and partitioning-processed martensitic stainless steels with different manganese content. *Materials Science and Technology*, 40(2024) 449 – 465. <https://doi.org/10.1177/02670836231215989>
- [44] M.C. Biesinger, B.P. Payne, A.P. Grosvenor, L.W.M. Lau, A.R. Gerson, R.St.C. Smart, Resolving surface chemical states in XPS analysis of first row transition metals, oxides and hydroxides: Cr, Mn, Fe, Co and Ni. *Applied Surface Science*, 257(2011)2717-2730. <https://doi.org/10.1016/j.apsusc.2010.10.051>
- [45] A. Barroux, T. Duguet, N. Ducommun, E. Nivet, J. Delgado, L. Laffont, C. Blanc, Combined XPS/TEM study of the chemical composition and structure of the passive film formed on additive manufactured 17-4PH stainless steel. *Surfaces and Interfaces*, 22(2021)100874. <https://doi.org/10.1016/j.surfin.2020.100874>

- [46] A.R. Pratt, I.J. Muir, H.W. Nesbitt, X-ray photoelectron and Auger electron spectroscopic studies of pyrrhotite and mechanism of air oxidation. *Geochimica et Cosmochimica Acta*, 58 (1994) 827-841. [https://doi.org/10.1016/0016-7037\(94\)90508-8](https://doi.org/10.1016/0016-7037(94)90508-8)
- [47] M. Vayer, I. Reynaud, R. Erre, XPS characterisations of passive films formed on martensitic stainless steel: qualitative and quantitative investigations. *Journal of Materials Science*, 35(2000) 2581–2587. <https://doi.org/10.1023/A:1004719213960>
- [48] S. Marcelin, N. Pébère, S. Régnier, Electrochemical characterisation of a martensitic stainless steel in a neutral chloride solution. *Electrochimica Acta*, 87(2013) 32-40. <https://doi.org/10.1016/j.electacta.2012.09.011>
- [49] P.S. Bagus, C.J. Nelin, C. R. Brundle, B. V. Crist, N. Lahirie, K.M. Rosso, Origin of the complex main and satellite features in Fe 2p XPS of Fe<sub>2</sub>O<sub>3</sub>. *Physical Chemistry Chemical Physics*, 24(2022) 4562 – 4575. <https://doi.org/10.1039/D1CP04886D>
- [50] D.N.G. Krishna, J. Philip, Review on surface-characterization applications of X-ray photoelectron spectroscopy (XPS): Recent developments and challenges. *Applied Surface Science Advances*, 12 (2022) 100332. <https://doi.org/10.1016/j.apsadv.2022.100332>
- [51] N. Rieders, M. Nandasiri, D. Mogk, R. Avci, New Insights into Sulfide Inclusions in 1018 Carbon Steels. *Metals*, 11(2021) 428. <https://doi.org/10.3390/met11030428>
- [52] H. Krawiec, V. Vignal, O. Heintz, R. Oltra, Influence of the dissolution of MnS inclusions under free corrosion and potentiostatic conditions on the composition of passive films and the electrochemical behaviour of stainless steels. *Electrochimica Acta*, 51(2006) 3235 – 3243. <https://doi.org/10.1016/j.electacta.2005.09.015>
- [53] E. Rahimi, A. Rafsanjani-Abbasi, A. Imani, A. Davoodi, TiO<sub>2</sub>/Cu<sub>2</sub>O coupled oxide films in Cl<sup>-</sup> ion containing solution: Volta potential and electronic properties characterisation by scanning probe microscopy. *Materials Chemistry and Physics*, 212(2018) 403-407. <https://doi.org/10.1016/j.matchemphys.2018.03.066>
- [54] E. Rahimi, A. Rafsanjani-Abbasi, A. Imani, S. Hosseinpour, A. Davoodi, Correlation of surface Volta potential with galvanic corrosion initiation sites in solid-state welded Ti-Cu bimetal using AFM-SKPFM. *Corrosion Science*, 140 (2018) 30–39, <https://doi.org/10.1016/j.corsci.2018.06.026>
- [55] D. Kovalov, C.D. Taylor, H. Heinrich, R.G. Kelly, Operando electrochemical TEM, ex-situ SEM and atomistic modeling studies of MnS dissolution and its role in triggering pitting corrosion in 304L stainless steel. *Corrosion Science*, 199 (2022) 110184. <https://doi.org/10.1016/j.corsci.2022.110184>
- [56] S. Tokuda, I. Muto, Y. Sugawara, N. Hara, Effect of Sensitization on Pitting Corrosion at MnS and CrS in Type 304 Stainless Steel. *Journal of The Electrochemical Society*, 168(2021) 091504. <https://doi.org/10.1149/1945-7111/ac28c6>

- [57] Y. Sun, X. Tan, R. Lan, G. Ran, J. Li, Y. Jiang, Mechanisms of inclusion-induced pitting of stainless steels: A review. *Journal of Materials Science & Technology*, 168(2024) 143 – 156. <https://doi.org/10.1016/j.jmst.2023.06.008>
- [58] X. Tan, Y. Jiang, Y. Chen, A. Tong, J. Li, Y. Sun, Roles of different components of complex inclusion in pitting of 321 stainless steel: Induction effect of CaS and inhibition effect of TiN, *Corrosion Science*, 209( 2022) 110692. <https://doi.org/10.1016/j.corsci.2022.110692>
- [59] G. Palumbo, D. Dunikowski, R. Wirecka, T. Mazur, U. Lelek-Borkowska, K. Wawer, J. Banaś, Effect of Grain Size on the Corrosion Behavior of Fe-3wt.%Si-1wt.%Al Electrical Steels in Pure Water Saturated with CO<sub>2</sub>. *Materials* (Basel), 14(2021) 5084. <https://doi.org/10.3390%2Fma14175084>
- [60] M. Soleimani, H. Mirzadeh, C. Dehghanian, Effect of grain size on the corrosion resistance of low carbon steel. *Materials Research Express*, 7 (2020) 016522. <https://doi.org/10.1088/2053-1591/ab62fa>



# 6

## Intergranular Corrosion of TiNb-microalloyed Martensitic Stainless Steels Processed by Quenching and Partitioning

This chapter is based on:

Gaojie Li, Maria Santofimia, Yaiza Gonzalez-Garcia. Intergranular corrosion of TiNb-microalloyed martensitic stainless steels processed by quenching and partitioning. *Submitted*. 2024.



## 6.1 Introduction

Previous chapters have introduced quenching and partitioning (Q&P) heat treatments and their application to our specifically designed martensitic stainless steels [1-7]. In **Chapter 2**, we designed a new class of martensitic stainless steels by accurately selecting chemistries and heat treatment parameters. **Chapters 3** and **4** explored the microstructure evolution, while **Chapter 5** investigated the relationship between microstructure and corrosion performance.

As discussed in **Chapter 5**, incorporating microalloying elements such as Ti and Nb in steels is a common strategy to improve impact toughness and strength through grain size refinement and precipitation strengthening [8-13]. Additionally, microalloying is another strategy to improve the corrosion resistance of stainless steels. Intergranular corrosion (IGC) in stainless steels occurs due to an electrochemical potential difference between the matrix and the Cr-depleted region, formed by the presence of Cr-carbide along the grain boundaries. It has been reported that microalloying with Nb and Ti in ferritic stainless steel is a practical method to reduce the risk of IGC by inhibiting the formation of Cr-carbide because they can react preferentially with carbon and nitrogen rather than Cr [14-22]. No attention has been paid to alloy design and the role of microalloying elements like Nb and Ti in the Q&P treated martensitic stainless steels. The role of Nb and Ti in the IGC behaviour of martensitic steels remains unknown.

In our previous Chapters, a new class of martensitic stainless steels was designed through the accurate selection of chemistries and heat treatment parameters [12,23,24]. We found that chromium carbides precipitate at the grain boundaries before the partitioning treatment in these newly designed martensitic stainless steels [24]. However, the corrosion behavior at grain boundaries cannot be clearly observed. We found that the corrosion resistance of Q&P steels is primarily controlled by the presence of MnS and TiN inclusions, with chemical composition and phase fractions playing a less significant role. This phenomenon is evident in industrially produced materials, where MnS inclusions are formed. Additionally, microalloying elements Ti and Nb contribute to the formation of new inclusions that can also favour the initiation of localised corrosion [23].

This chapter investigates the role of microalloying elements on the corrosion behaviour of Q&P-processed martensitic stainless steels that are processed at laboratory conditions by dilatometry. Under these conditions, the presence of MnS inclusions is minimised. Q&P treated 0.3 wt.% C – 13 wt.% Cr martensitic stainless steels are investigated without and with 0.05 wt.% Ti and 0.05 wt.% Nb. Microstructure and grain boundaries are characterised using scanning electron microscopy (SEM), transmission electron microscopy (TEM) equipped with energy dispersive spectroscopy (EDS), and scanning Kelvin probe force microscopy (SKPFM). Potentiodynamic polarisation (PDP) and double-

loop electrochemical potentiokinetic reactivation (DL-EPR) tests are conducted to inspect the susceptibility of the samples to localised corrosion and to IGC sensitisation, respectively.

## 6.2 Experimental Procedure

### 6.2.1 Materials and Heat-treatment

The chemical compositions of the two stainless steels investigated in this work are given in **Table 6.1**. These are the 3C HMn and 3C HMn-NbTi alloys, which their design is described in **Chapter 2**. The specimens are cylindrical and were generated and dilatometer-processed in the same manner as those in **Chapters 2, 3 and 4**.

**Table 6.1. Chemical composition of the studied martensitic stainless steel, in wt.%.**

Alloy	Fe	C	Mn	Si	Cr	Ni	Al	N	Nb Ti
3C HMn	Bal.	0.30	3.0	0.35	13	0.2	0.01	0.03	..
3C HMn-NbTi	Bal.	0.30	3.0	0.35	13	0.2	0.01	0.03	0.05-0.05

**Figure 6.1** shows a scheme of the heat treatments applied to the cylindrical specimens in the dilatometer. The heat treatment parameters were selected in **Chapter 2** and also reported in [24]. The Q&P specimens are first austenitised at 1100 °C for 15 minutes to obtain full austenitic microstructures, followed by cooling to the optimum quench temperature (OQT) shown in **Chapter 2** (50 °C and 62 °C, respectively). Then, the quenched specimens are reheated to 450 °C and held at this temperature for 5 minutes to allow the partitioning of carbon from martensite to austenite. The process ended with quenching again to room temperature.

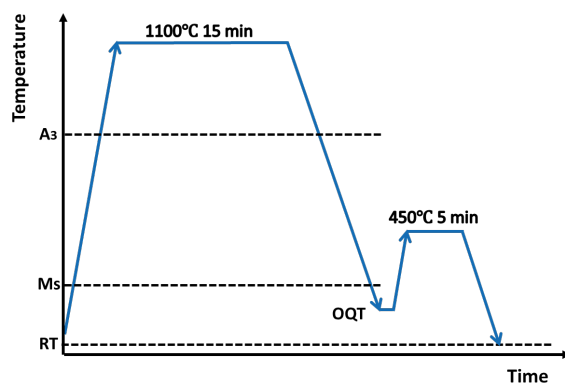


**Figure 6.1. Applied Q&P heat treatment on samples.**

### 6.2.2 Microstructural Characterisation

The surface of the Q&P processed samples is prepared by standard metallographic procedures and finished by OPS (Oxide Polishing Suspensions) polishing for 15 minutes. A Vilella reagent (ASTM E407-80) consisting of 1 g picric acid, 5 ml HCl and 100 ml ethanol is employed. Optical microscopy (Digital Keyence VHX-5000 and optical LEICA DMLM) and a Field Emission Gun Scanning Electron Microscope (FEG-SEM, JEOL JSM-6500F) operating at 15 kV and 10 mm working distance are used to characterise the microstructure.

Thin cross-sections of the samples are made with a TFS Helios Nanolab G3 and secured on the copper half grids for TEM examinations using the lift-out procedure. A 200-nm-thick layer of Pt is deposited initially with a 2 keV electron beam, followed by ion-beam deposition until reaching a Pt thickness of approximately 1  $\mu\text{m}$ . The thinning-down process is done with the Ga ion beam at 30 keV, followed by a quick cleaning at 5 keV.

TEM investigations are performed with a TFS Talos F200X equipped with 4 in-column SDD Super-X detectors. Bright-field (BF) and dark-field (DF) TEM images are taken by inserting objective aperture and beam tilt to choose desired diffraction spots. High-angle annular dark field (HAADF)-STEM/EDS are carried out to elementally map the samples, revealing different inclusions.

The phase fraction after Q&P heat treatment is the same for both alloys, with austenite 0.57 and martensite 0.43, as indicated in **Chapter 2** (2.4.1 *Application of Q&P treatments in the dilatometer*).

### 6.2.3 Electrochemical Tests

The electrochemical experiments are performed using a Biologic VSP-300 potentiostat supported by EC-Lab V11.36 software. The experimental setup is a three-electrode cell, using an Ag/AgCl/KCl(sat.) electrode as a reference electrode (RE), a platinum mesh as a counter electrode (CE), and the sample as the working electrode (WE). The potential scan rate is 0.167 mV/s from -200 mV vs. OCP until the breakdown potential. Prior the potentiodynamic polarisation (PDP) measurements, the open circuit potential (OCP) is measured for 1.5 hours, at which steady-state is achieved. Aerated 3.5 wt.% NaCl aqueous solution is used as the electrolyte, and measurements are carried out at room temperature ( $\sim 20^\circ\text{C}$ ). At least four repetitions are carried out to confirm the reproducibility of the experiments.

The specimens are evaluated for degree of sensitisation (DOS) using a double loop electrochemical potentiokinetic reactivation (DL-EPR) test in 0.01M  $\text{H}_2\text{SO}_4$  solution at room temperature. The potential scan rate is 1.66 mV/s from -600 mV to + 200 mV vs. the RE and then immediately reversed to the starting point as the same scanning rate. DOS is reported as the ratio of maximum current density in the

reactivation loop ( $I_r$ ) to the current density in the activation loop ( $I_a$ ). At least five repetitions are carried out to confirm the reproducibility of the experiments, and the average values are reported.

The SKPFM measurements are performed in the tapping mode using a Bruker Dimension Edge<sup>TM</sup> instrument with Nanodrive v8.05 software. A rectangular conductive cantilever (silicon pyramid single-crystal tip coated with PtIr5, SCM-Pit probe) is employed. A direct current (DC) bias potential is applied to the AFM tip for all measurements. All AFM/SKPFM measurements are performed with a scan rate of 0.15 Hz and a pixel resolution of  $512 \times 512$ . The raw data is analysed using Gwyddion 2.60 software.

## 6.3 Results

### 6.3.1 OM and SEM Microstructures

**Figure 6.2** illustrates the OM and SEM micrographs of the microstructures of the two Q&P treated alloys. OM images in **Figure 6.2** (a) and (b) show that the prior austenite grains are mostly equiaxial. It is also evident that the prior austenite grain size (PAGS) of alloy 3C HMn is much larger than that of alloy 3C HMn-NbTi. The quantitative PAGS statistics indicate that the average PAGS of alloy 3C HMn is  $103 \pm 43 \mu\text{m}$  and of alloy 3C HMn-NbTi is  $30 \pm 15 \mu\text{m}$ . On the sample surface of alloy 3C HMn-NbTi, bright yellow particles are observed, which have been confirmed as TiN particles in ref [23].

Furthermore, segregation bandings are also observed in both samples. From **Chapters 3** and **4**, the dark etched bands correspond to martensite-rich bands and the bright bands to austenite-rich. The selective etching of bands is caused by the elemental segregation of Cr and Mn content during the Q&P treatment. The SEM images in **Figure 6.2** (c) and (d) illustrate that, in both alloys, there is carbide precipitation at the grain boundaries.

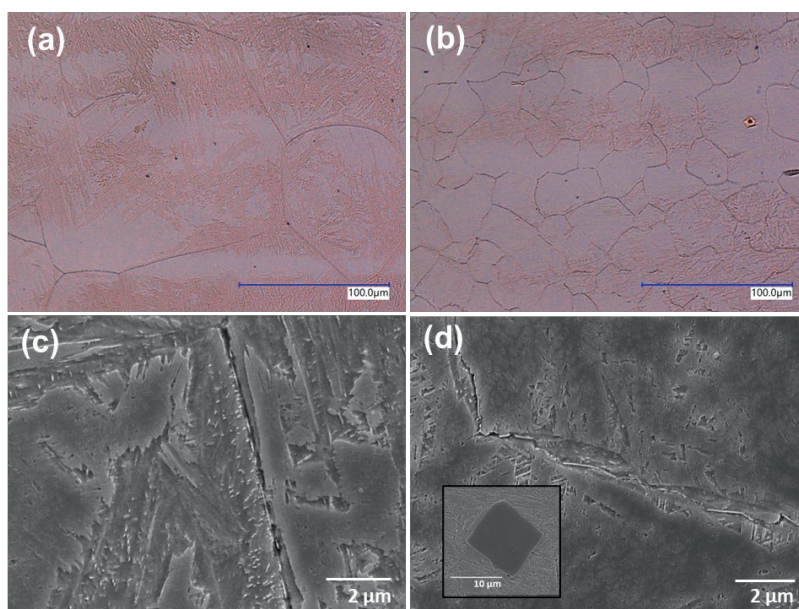


**Figure 6.2.** OM and SEM microstructures of Q&P treated alloys after etching for 15 s: (a)(c) alloy 3C HMn, and (b)(d) alloy 3C HMn-NbTi.

### 6.3.2 Electrochemical Characterisation

The corrosion properties of the samples are studied using PDP experiments to investigate the effect of microstructural characteristics on corrosion performance. **Figure 6.3** (a) and (b) show representative curves and corresponding analysis. **Figures 6.3** (c) and (d) display OM images of the specimens after the potentiodynamic polarisation tests.

The curves in both samples (**Figure 6.3** (a)) show very similar passivity range but did not show a sharp breakdown potential. Instead, there is a gradual increase of current density until a more dramatic change at around a potential of 0 V when we can consider a failure of the passivity. **Figure 6.3** (b) compares the corrosion current density ( $i_{corr}$ ) and corrosion potential ( $E_{corr}$ ) extrapolated from PDP curves, respectively. The corrosion current density and potential values for both alloys fall relatively into the same range.

The optical images of the surface after the tests (**Figures 6.3** (c) and (d)) showed no evidence of pits on the surface of the samples. Instead, the prior austenite grain boundaries appear preferentially attacked for both alloys. Especially in alloy 3C HMn-NbTi, the grain boundaries (GBs) are severely corroded leading to areas with prior austenite grains dropout, which is consistent with the grain-dropout phenomenon previously documented in the literature [14,17,18]. The preferential attack of grain

boundaries and absence of pits could explain the absence of a sharp breakdown potential in the PDP curves.

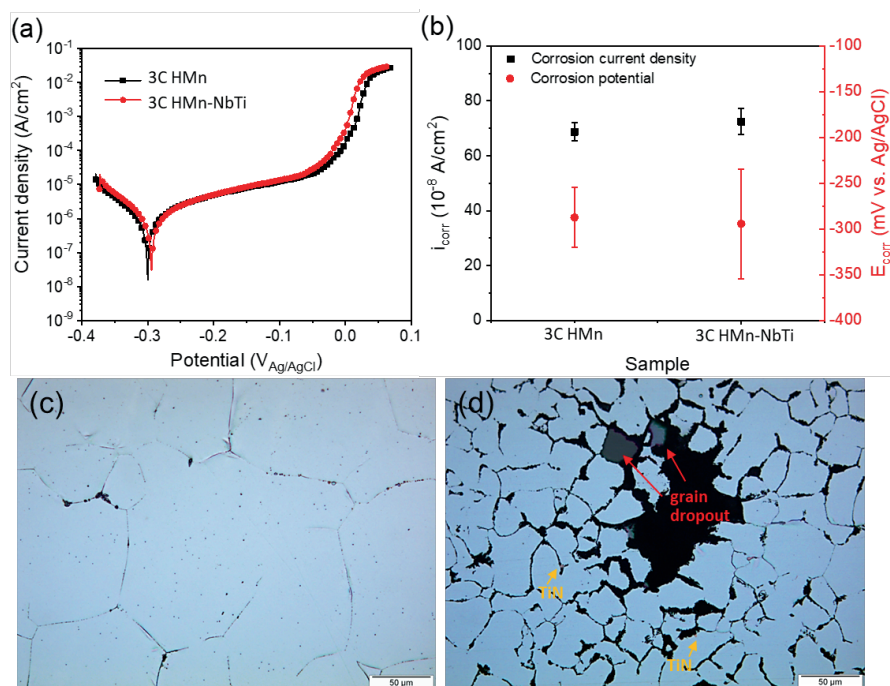


**Figure 6.3. (a) Selected potentiodynamic polarisation curves and (b) averaged values of the corrosion current density and corrosion potential of alloys 3C HMn and 3C HMn-NbTi. (c)(d) OM microstructures after polarisation of alloy 3C HMn alloy 3C HMn-NbTi, respectively.**

6

To further confirm and quantify the susceptibility to intergranular corrosion, DL-EPR experiments are carried out, and the degree of sensitisation (DOS) is estimated for both Q&P-treated samples. **Figure 6.4** shows DL-EPR results for the Q&P treated specimens. From **Figure 6.4** (a), typical DL-EPR curves are seen with significant activation current peaks ( $I_a$ ) and small reactivation current peaks ( $I_{r1}$  and  $I_r$ ). During the anodic scan, the entire surface is activated to form the activation current peak at a potential of approximately -0.35 V ( $E_a$ ). Then, the current decreased within a wide passivity range from -0.35 V to 0.2 V, in which a wide passive film can form on the surface. There is no significant difference between samples regarding the activation scan.

In the reverse scan, the reactivation current peaks are attributed to the defects of passive films, such as the Cr-depleted zones. There is more than one reactivation current peak in each alloy, referred as  $I_{r1}$  and  $I_r$  peaks. The presence of two reactivation peaks can be attributed to not homogenous sensitisation of the steels with not only the Cr-depleted zones but also other features in the microstructure. As observed in the microstructure analysis and discussed in **Chapter 3** [24], these Q&P treated samples

present chemical segregation bands. This could explain the appearance of a second reactivation peak. The second reactivation peak at a lower potential value is attributed to the IGC [25]. These peaks for the investigated alloys are approximately at a potential ( $E_r$ ) value of -0.4 V. The DOS to IGC of each specimen is measured by the ratio  $I_r/I_a$ , corresponding to the reactivation ( $I_r$ ) and activation ( $I_a$ ) current peaks identified in the curve. The DOS values estimated from the curves are shown in **Figure 6.4** (b). The average DOS value for alloy 3C HMn is  $0.73 \pm 1.07$  %, which indicates very low susceptibility to IGC, while alloy 3C HMn-NbTi showed a higher value,  $3.75 \pm 1.13$  %, considered in the range of moderate susceptibility.

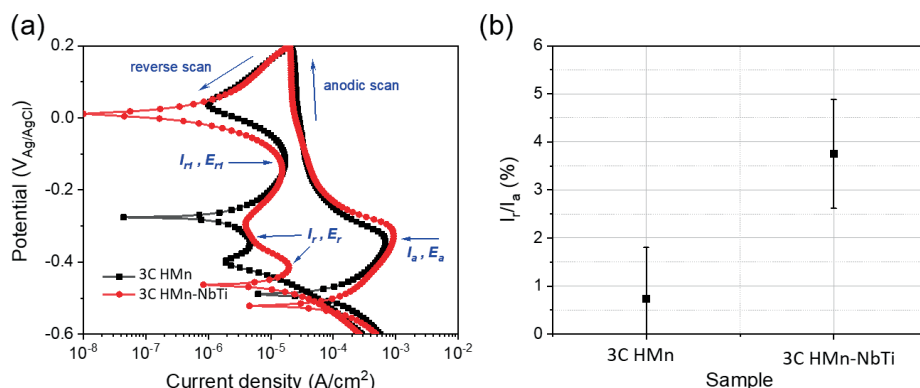


**Figure 6.4.** (a) DL-EPR curves plotted for alloys 3C HMn and 3C HMn-NbTi after Q&P heat treatment, (b) corresponding degree of sensitisation (DOS) values. The values are obtained from average of five repetitions.

### 6.3.3 Grain Boundary Analysis

TEM and STEM measurements are employed to characterise the grain boundaries at the nanoscale. **Figure 6.5** shows the FIB cutting location, TEM micrographs, and EDS analysis results for both alloys. For the case of alloy 3C HMn, **Figure 6.5** (a)(b) shows the cutting location at the grain boundary containing a carbide particle with a diameter of approximately 200 nm. The STEM/EDS analysis indicates that this particle is Cr-carbide, and the Cr-depleted zone in the vicinity of Cr-carbide is clearly observed, as pointed out in figure **Figure 6.5** (b)(c). For alloy 3C HMn-NbTi, as shown in **Figure 6.5** (d), a FIB cut is also made from a grain boundary location, specifically near a TiN particle with a size of 5  $\mu\text{m}$ . The grain boundary precipitate with a length of 200 nm is observed in **Figure 6.5** (e). The EDS analysis of the precipitate also shows high chromium and carbon contents. As such, in both alloys, these GBs precipitates are Cr-carbides.

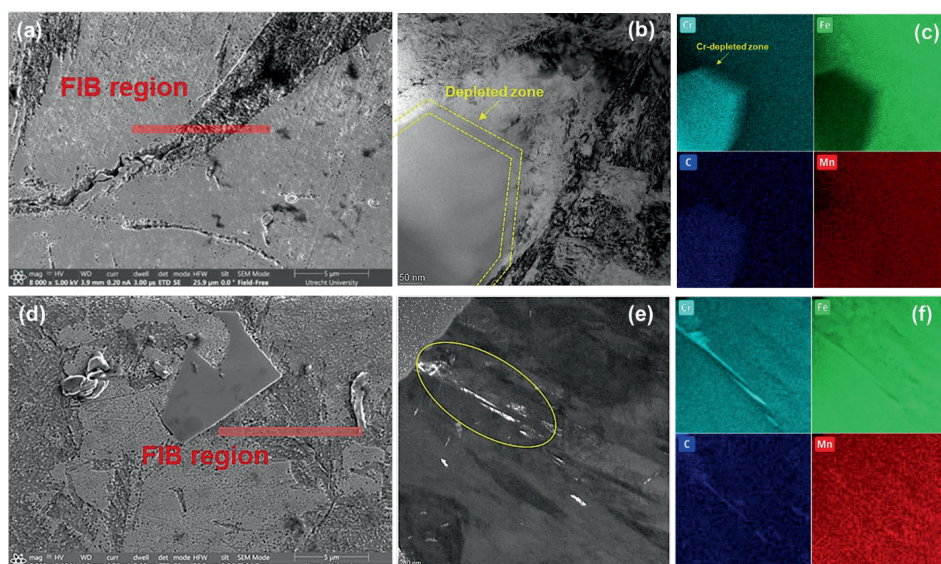


**Figure 6.5.** Area corresponding to FIB cutting, TEM image of the microstructure, and STEM/EDS elemental analysis of GB precipitate in alloys 3C HMn (a)(b)(c) and 3C HMn-NbTi (d)(e)(f), respectively.

**Figure 6.6** displays the STEM with EDS mapping of one representative particle in alloy 3C HMn-NbTi. The spherical particles with a diameter of approximately 50 nm are widely observed at (grain and phase) interfaces. EDS analysis shows high contents of Ti, Nb and N, and low content of Cr and Fe. The Ti and N atoms are primarily located in the particles' centre and surrounded by Nb. These nano-size TiN(Nb) particles have the same/similar composition as the big rectangular/triangle bright yellow particles (in **Figure 6.2**).

Nb-Ti microalloy particles of varying size are widely studied in HSLA steels for precipitation-strengthening purposes [26-29]. It is reported that heterogeneous nucleation sites such as grain boundaries, dislocations, or second-phase particles are preferable for insoluble TiN particles [26]. At a later stage, Nb atoms then precipitate on the pre-existing TiN particles, forming a so-called "core-shell" configuration [27]. TEM analysis demonstrates that the GBs of alloy 3C HMn-NbTi contain not only Cr-carbides but also TiN(Nb) macroparticles (10  $\mu\text{m}$ ) and nanoparticles (50 nm).

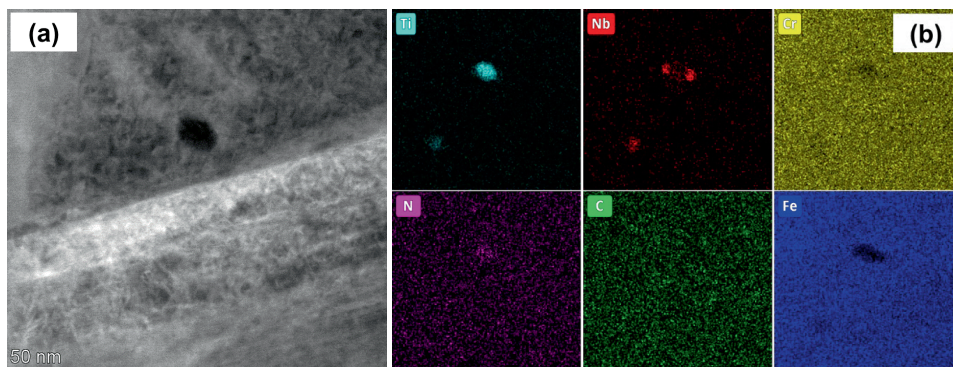


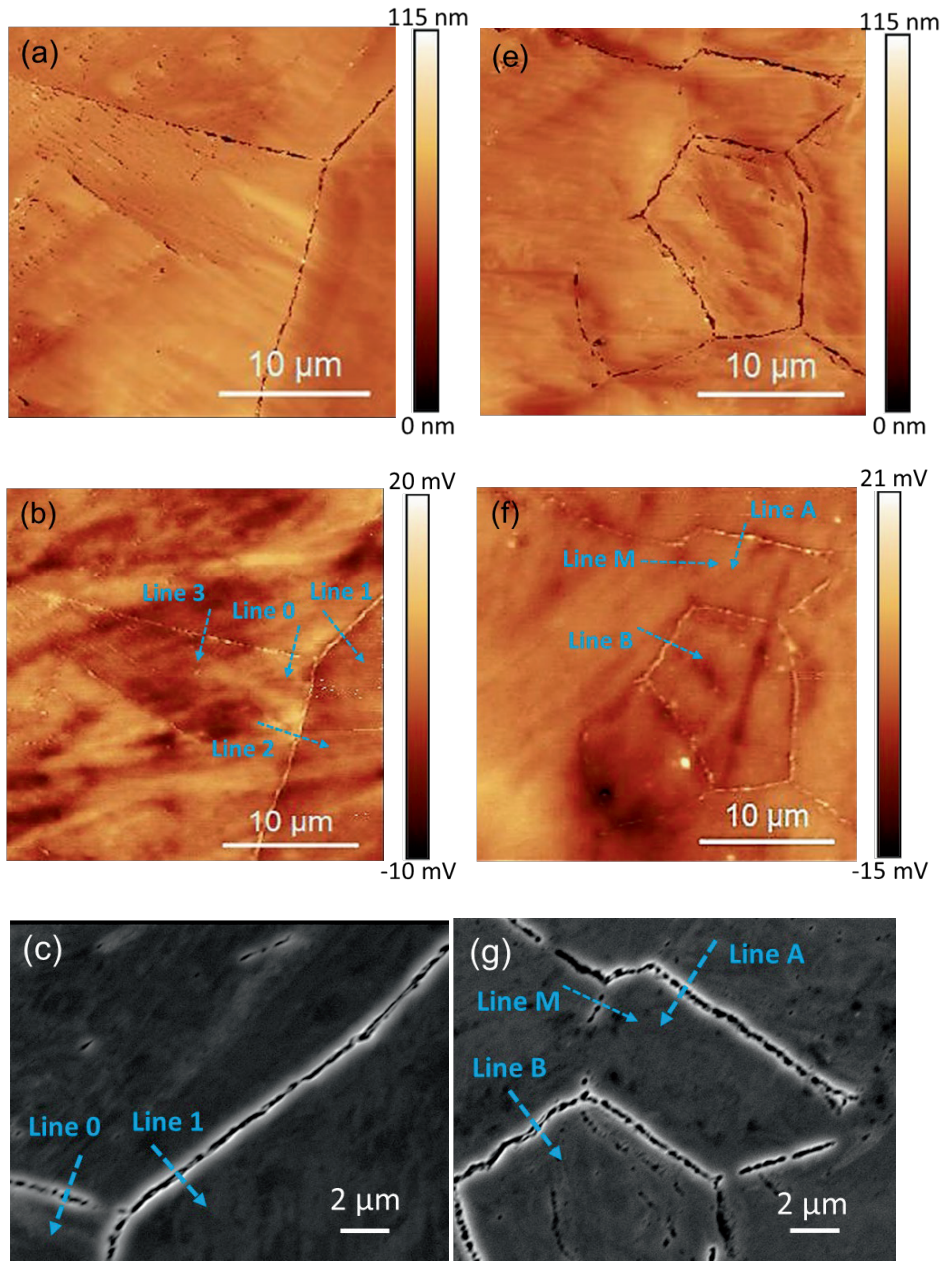
**Figure 6.6. (a) TEM image of the grain boundary and (b) STEM/EDS elemental analysis of precipitate particle in alloy 3C HMn-NbTi.**

In order to further verify the possible different reactivity of the grain boundaries due to the presence of the different precipitates, surface Volta potential mapping by SKPFM is performed along the grain boundaries of the investigated steels.

**Figure 6.7** displays the SKPFM topography and Volta potential maps, and the corresponding SEM micrographs. In order to localise the grain boundaries during SKPFM experiments, the samples were slightly etched using a Vilella reagent solution. Topography maps of both samples in **Figure 6.7** (a) and (e) show that the GBs appear as trenches across the matrix. For alloy 3C HMn, the Volta potential map in **Figure 6.7** (b) shows that the GBs are brighter and have a higher Volta potential than the surrounding matrix. **Figure 6.7** (c) shows an enlarged GB region from which the line Volta potential profile is made. Lines 1 - 3 are made over grain boundaries with Cr-carbides, while Line 0 is over grain boundaries without carbide precipitation. The corresponding Volta potential distribution in **Figure 6.7** (d) shows some difference between the matrix and the GBs. For Line 0, the surface potential waved within the 4 mV range, and there are no potential peak links to carbide. The peaks of the Volta potential at Lines 1-3 are linked to the Cr-carbides precipitated inside GBs. The drop of the Volta potential originates from the Cr-depleted zone induced by Cr-carbide precipitation, as previously displayed in **Figure 6.3**. The Volta potential difference between the Cr-carbide and Cr-depleted zone is up to 9.8 mV, as the graph indicates.

For the case of alloy 3C HMn-NbTi, as seen in **Figure 6.7** (e-h), the GBs on the sample surface exhibit the same characteristics as that of alloy 3C HMn. The Cr-depletion occurring adjacent to the Cr-carbide precipitation leads to low Volta potential, as well the Volta potential peak is recorded on the Cr-carbides, and the potential difference reaches approximately 9.2 mV. For the line profile over the grain boundary without carbide precipitation, Line M shows no signs of a potential peak. Apparently, the Volta potential difference will contribute to the susceptibility to IGC of the investigated Q&P steels,

and the Cr-depleted zone in the vicinity of Cr-carbides would be the active dissolution region when exposed to a corrosive environment.



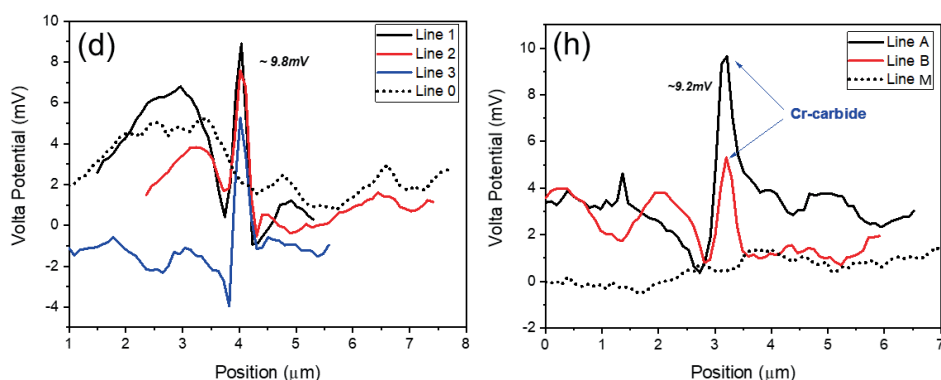


**Figure 6.7. The AFM topography map, Volta potential maps, SEM micrograph, and Volta potential line profiles across the grain boundaries, respectively, of alloy 3C HMn (a-d) and alloy 3C HMn-NbTi (e-h) on the etched sample surface.**

It has been observed that microalloying particles are located at GBs, where they may influence GB activity in the presence of Cr-carbides and Cr-depleted zones. The interplay of these factors on susceptibility to IGC requires further clarification. To explore this further, in alloy 3C HMn-NbTi, the Volta potential distribution along the TiN(Nb) particles was measured using SKPFM. The topography, Volta potential maps and line Volta potential profiles are shown in **Figure 6.8** below. As can be seen from **Figure 6.8** (a), the TiN(Nb) particle stands out from the matrix and has a much higher Volta potential value than the matrix, as already reported in [23]. The line profiles cross the particle in **Figure 6.8** (c) show that the Volta potential of the TiN(Nb) particle is 100 mV higher than that of the matrix. The difference in the chemical composition of TiN(Nb) may affect the Volta potential. Thus, line 2 shows a difference from line 1 regarding the Volta potential measured on the TiN(Nb).

The interface between particle and matrix on both line profiles, as indicated in the figure, shows a significant Volta potential drop of 10 mV compared to the matrix. This can be attributed to the difference in chemical composition at the interface, i.e. the Nb clustering, as observed under TEM in **Figure 6.4**.

As such, the phase exhibiting positive Volta potential values relative to the matrix would show cathodic behaviour [25]. Thus, the TiN(Nb) particle with a relatively high Volta potential would serve as the micro-cathode, and the surrounding steel matrix (specifically, the interface) would serve as the micro-anode. Considering that the TiN(Nb) particles were also identified at GBs in the case of alloy 3C HMn-NbTi, they can exacerbate the sensitivity of IGC, which was initially only caused by Cr-carbides. As a result, its DOS to IGC is higher than alloy 3C HMn, as reported in **Figure 6.4**.

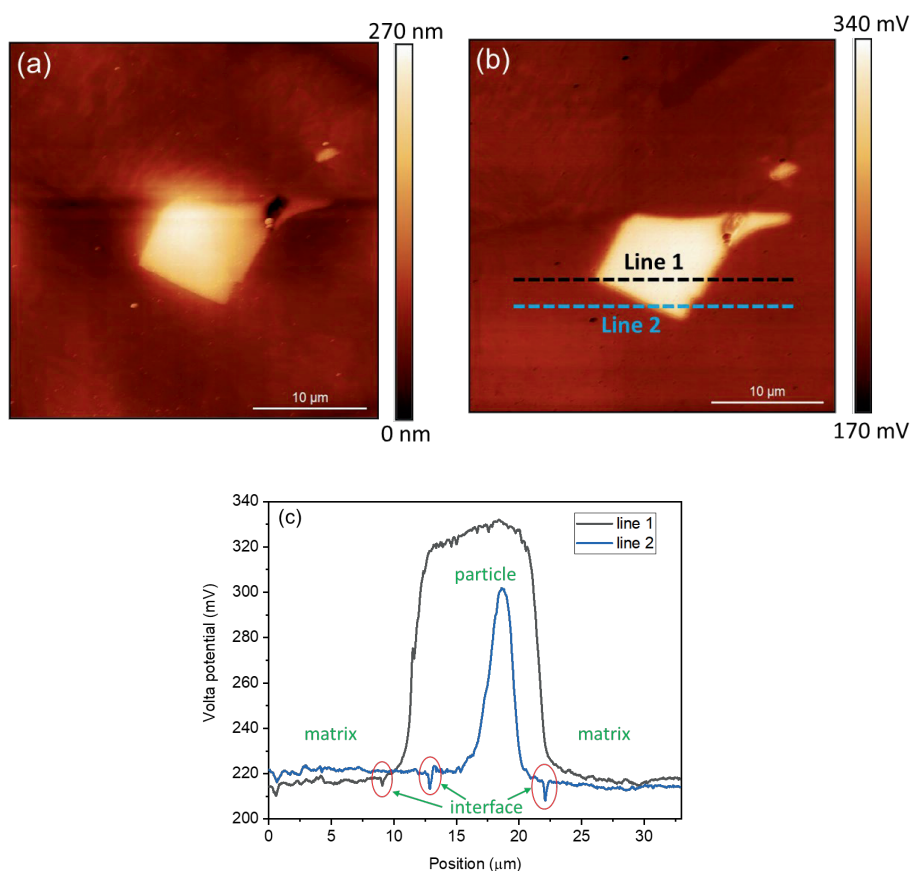


**Figure 6.8.** (a) Volta-potential map, (b) topography map, and (c) line profile of TiNb particle in alloy 3C HMn-NbTi (polished surface).

## 6.4 Discussion

The Q&P martensitic stainless steels processed under laboratory conditions in this work exhibited a different corrosion mechanism from the previously reported pitting corrosion in **Chapter 5**. Cr-carbides are present in both alloys, even after the Q&P heat treatment. The microalloying elements Nb and Ti did not play a role in reducing the precipitation of Cr-carbides at grain boundaries, as reported previously for the case of ferritic stainless steels [14-22]. Contrary to our previous work in **Chapter 5** and [23], in this case, pitting corrosion is not the dominant mechanism, given the absence of inclusions. In this case, the grain boundaries of the martensitic steels became the preferential sites for localised attack.

The addition of microalloying elements Nb and Ti refined the prior austenite grain size from  $103 \pm 43 \mu\text{m}$  in alloy 3C HMn to  $30 \pm 15 \mu\text{m}$  in alloy 3C HMn-NbTi. TiN(Nb) precipitation is observed in alloy 3C HMn-NbTi. However, the electrochemical results revealed no significant difference in the corrosion resistance when considering the differences in the chemical composition of the alloys and different grain sizes. The influence of grain size on the corrosion resistance of different stainless steels has been reviewed by Ralston et al. [30]. Refining of the grain size is reported to increase or decrease the susceptibility to corrosion depending on the alloy and the processing route. In the case of alloy 3C HMn and alloy 3C HMn-NbTi, these were not observed. Potentiodynamic polarisation results showed no significant differences between the alloys.

The presence of Cr-carbides at grain boundaries, confirmed by TEM analysis, explains the susceptibility of the alloys to intergranular corrosion. The degree of susceptibility (DOS) increases in alloy 3C HMn-NbTi due to the additional presence of TiN(Nb) particles. TEM and SKPFM results demonstrated that, in both alloys, the Cr-depleted regions (Cr-carbide/matrix interface) were preferentially dissolved as the anode during the corrosion process, while the Cr-(rich)carbide in GBs was not dissolved as the cathode. Additionally, in alloy 3C HMn-NbTi, TiN(Nb) particle was detected both in the macro scale ( $10 \mu\text{m}$  under SEM) and nanoscale ( $50 \text{ nm}$  under TEM). An extra galvanic effect was thereby formed, in which the TiN(Nb)/matrix interface (probably Nb clustering) served as the anode during the corrosion process, while the TiN(Nb) particle was the cathode.

From these results, the IGC mechanism is elucidated in the diagram of **Figure 6.9**. For the case of alloy 3C HMn, the IGC process can be seen in **Figure 6.9** (a-c). The grain boundaries (GBs) region contains Cr-carbides and adjacent Cr-depleted zone. The interface of the Cr-carbides, indicated in red, shows a lower Volta potential. When the sample surface is exposed to corrosive environments, such as NaCl solution (illustrated in **Figure 6.9** (b)), the presence of chloride ions ( $\text{Cl}^-$ ) makes the GBs and the particle/matrix interfaces particularly susceptible to anodic dissolution. Starting from a selected dissolution of the matrix around particles at GBs, the dissolution process gradually extends into the Cr-depleted zone over time. Eventually, the isolated localised corrosion pits deepen and merge, resulting in the formation of corrosion ditches along the GBs, which is characteristic of intergranular corrosion.

For the case of alloy 3C HMn-NbTi, as shown in **Figure 6.9** (d-f), not only the Cr-carbides interface but also the TiN(Nb) particle interface becomes the anodic sites. It would continuously exert the galvanic effect. Thus, it will take a shorter time for separated local corroding sites at the boundary to connect, leading to intergranular corrosion. For specific locations with macro-size TiN(Nb) particles, the micro-galvanic effect is still triggered, enhancing the attack of the surrounding matrix and generating deeper trenches and with the possible neighbouring grain "dropout", as reported in [14,17,18]. This leads to the microstructure observed in **Figure 6.3** and **Figure 6.9** (f). In summary, the

presence of Cr-carbides at GB compromise the corrosion resistance of the steel, leading to IGC as the failure mechanism. The addition of micro-alloying elements, increases the susceptibility of the steel to IGC due to the formation of nano- and micro-meter TiNb precipitates also located at the grain boundaries and surroundings, respectively.

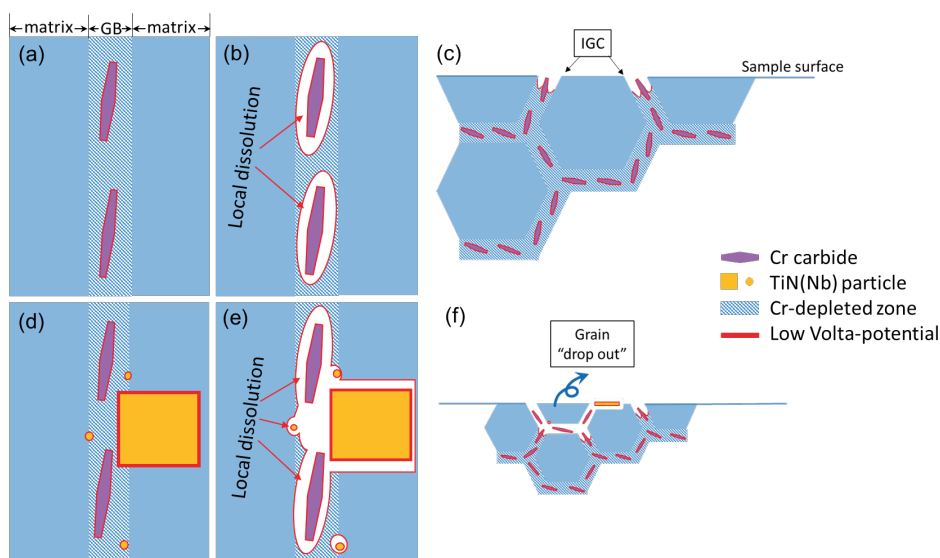


**Figure 6.9. Schematic diagram illustrating the microstructure of grain boundary, local dissolution of grain boundary in electrolyte and cross-section view in an electrolyte, respectively, of alloy 3C HMn (a-c) and alloy 3C HMn-NbTi (d-f).**

## 6.5 Conclusions

The effect of microalloying elements Nb and Ti on the intergranular corrosion performance of Q&P treated martensitic stainless steels is investigated by microstructure characterisation and electrochemical examination in two alloys, one containing Nb and Ti. The steels were processed under controlled laboratory conditions. The main conclusions are drawn as follows:

- Steels processed under laboratory conditions exhibited some microstructure differences compared to those produced industrially [23]. The absence of MnS inclusions, the presence of segregation banding and, more interesting, the formation of Cr-carbides at the grain boundaries.
- The microalloying elements Nb and Ti did not significantly affect Cr-carbide precipitation at GBs. Furthermore, the quenching and partitioning process was unable to redissolve these carbides.

- Microalloying elements Nb and Ti formed TiN(Nb) precipitates at GBs and grains, with a "core-shell" structure comprising early precipitation of TiN particles on which Nb precipitates.
- The electrochemical analysis showed that these microstructural differences lead to a preferential attack at grain boundaries (IGC) instead of localised pitting corrosion.
- In both alloys, the presence of Cr-carbides along GBs and Cr-depletion zones at the carbide-matrix interface region are the main reasons for IGC susceptibility when exposed to a corrosive environment.
- Alloy 3C HMn-NbTi showed higher IGC susceptibility than alloy 3C HMn from the DOS analysis. The addition of Nb and Ti exacerbates the reactivity of the GBs due to the presence of additional particles, which are assumed to be cathodic with respect to the matrix.

These findings highlight a distinct corrosion mechanism in laboratory-processed Q&P steels, differing from the behaviour observed in industrially processed martensitic stainless steels, as demonstrated in **Chapter 5**. The influence of microalloying elements and precipitates on intergranular corrosion susceptibility was elucidated, offering new insights into the interplay between microstructure and localised corrosion in these advanced steels.

## References

- [1] N. Fonstein, Evolution of strength of automotive steels to meet customer challenges, In: *Advanced High Strength Sheet Steels*. Springer, Cham. (2015) 1–16. [https://doi.org/10.1007/978-3-319-19165-2\\_1](https://doi.org/10.1007/978-3-319-19165-2_1)
- [2] W. Wang, M. Li, C.W. He, X. Wei, D.Z. Wang, H.B. Du, Experimental study on high strain rate behavior of high strength 600–1000 MPa dual phase steels and 1200 MPa fully martensitic steels. *Materials and Design*, 47(2013) 510–521. <https://doi.org/10.1016/j.matdes.2012.12.068>
- [3] A. Grajcar, R. Kuziak, W. Zalecki, Third generation of AHSS with increased fraction of retained austenite for the automotive industry. *Archives of Civil and Mechanical Engineering*, 12(3) (2012) 334–341. <https://doi.org/10.1016/j.acme.2012.06.011>
- [4] A. Contreras, A. López, E.J. Gutiérrez, B. Fernández, A. Salinas, R. Deaquino, A. Bedolla, R. Saldaña, I. Reyes, J. Aguilar, R. Cruz, An approach for the design of multiphase advanced high-strength steels based on the behavior of CCT diagrams simulated from the intercritical temperature range. *Materials Science & Engineering A*, 772(2020) 138708. <https://doi.org/10.1016/j.msea.2019.138708>
- [5] J.G. Speer, A.M. Streicher, D.K. Matlock, F. Rizzo, G. Krauss, Quenching and partitioning: a fundamentally new process to create high strength trip sheet microstructures. *The Iron & Steel Society*, (2003) 505–522.
- [6] J.G. Speer, D.K. Matlock, B.C. De Cooman, J.G. Schroth, Carbon partitioning into austenite after martensite transformation. *Acta Materialia*, 51 (2003) 2611–2622. [http://dx.doi.org/10.1016/S1359-6454\(03\)00059-4](http://dx.doi.org/10.1016/S1359-6454(03)00059-4)
- [7] J.G. Speer, F. Rizzo, D.K. Matlock, D.V. Edmonds, The “quenching and partitioning” process: background and recent progress. *Materials Research*, 8 (2005) 417–423. <http://dx.doi.org/10.1590/S1516-14392005000400010>
- [8] M. Charleux, W.J. Poole, M. Militzer, A. Deschamps, Precipitation behavior and its effect on strengthening of an HSLA-Nb/Ti steel. *Metallurgical and Materials Transactions A*, 32(2001) 1635–1647. <http://dx.doi.org/10.1007/s11661-001-0142-6>
- [9] I. Gutiérrez, effect of microstructure on the impact toughness of Nb-microalloyed steel: Generalisation of existing relations from ferrite–pearlite to high strength microstructures. *Materials Science and Engineering: A*, 571 (2013) 57–67. <http://dx.doi.org/10.1016/j.msea.2013.02.006>
- [10] X.J. Liu, J.C. Yang, C.K. Cai, A.X. Li, X. Lei, C.Q. Yang, Effect of microalloyed elements M (M = Ce, Ti, V, and Nb) on mechanical properties and electronic structures of  $\gamma$ -Fe: Insights from a first-principles study. *Steel research international*, 92 (2021) 2100053. <https://doi.org/10.1002/srin.202100053>

- [11] J. Weibel, H. Mohrbacher, E. Detemple, D. Britz, F. Mücklich, Quantitative analysis of mixed niobium-titanium carbonitride solubility in HSLA steels based on atom probe tomography and electrical resistivity measurements. *Journal of Materials Research and Technology*, 18(2022) 2048–2063. <http://dx.doi.org/10.1016/j.jmrt.2022.03.098>
- [12] Y. Zou, Y. Han, H.S. Liu, H.X. Teng, M.S. Qiu, F. Yang, Microstructure evolution and enhanced mechanical properties of a novel Nb-Ti micro-alloyed medium-Mn steel. *Materials Characterization*, 187(2022) 111828. <https://doi.org/10.1016/j.matchar.2022.111828>
- [13] Y.J. Zhang, G. Miyamoto, T. Furuhashi, Enhanced hardening by multiple microalloying in low carbon ferritic steels with interphase precipitation. *Scripta Materialia*, 212(2022) 114558. <https://doi.org/10.1016/j.scriptamat.2022.114558>
- [14] J.K. Kim, Y.H. Kim, S.H. Uhm, J.S. Lee, K.Y. Kim, Intergranular corrosion of Ti stabilized 11wt% Cr ferritic stainless steel for automotive exhaust systems. *Corrosion Science*, 51(2009) 2716–2723. <https://doi.org/10.1016/j.corsci.2009.07.008>
- [15] J.K. Kim, B.J. Lee, B.H. Lee, Y.H. Kim, K.Y. Kim, Intergranular segregation of Cr in Ti-stabilized low-Cr ferritic stainless steel. *Scripta Materialia*, 61(2009) 1133–1136. <https://doi.org/10.1016/j.scriptamat.2009.08.045>
- [16] J.K. Kim, Y.H. Kim, K.Y. Kim, Influence of Cr, C and Ni on intergranular segregation and precipitation in Ti-stabilized stainless steels. *Scripta Materialia*, 63(2010) 449–451. <https://doi.org/10.1016/j.scriptamat.2010.05.002>
- [17] J.K. Kim, Y.H. Kim, J.S. Lee, K.Y. Kim, Effect of chromium content on intergranular corrosion and precipitation of Ti-stabilized ferritic stainless steels. *Corrosion Science*, 52(2010) 1847–1852. <https://doi.org/10.1016/j.corsci.2010.01.037>
- [18] J.K. Kim, Y.H. Kim, B.H. Lee, K.Y. Kim, New findings on intergranular corrosion mechanism of stabilized stainless steels. *Electrochimica Acta*, 56(2011) 1701–1710. <https://doi.org/10.1016/j.electacta.2010.08.042>
- [19] J.K. Kim, J.S. Lee, K.Y. Kim, Intergranular precipitation and corrosion in weld of low Cr ferritic stainless steel. *Metals and Materials International*, 18(2012) 619–624. <https://doi.org/10.1007/s12540-012-4008-9>
- [20] J.H. Park, J.K. Kim, B.H. Lee, S.S. Kim, K.Y. Kim, Three-dimensional atom probe analysis of intergranular segregation and precipitation behavior in Ti–Nb-stabilized low-Cr ferritic stainless steel. *Scripta Materialia*, 68(2013) 237–240. <https://doi.org/10.1016/j.scriptamat.2012.10.022>
- [21] J.H. Park, J.K. Kim, B.H. Lee, H.S. Seo, K.Y. Kim, Effect of Zr addition on intergranular corrosion of low-chromium ferritic stainless steel, *Scripta Materialia*, 76(2014) 77–80. <https://doi.org/10.1016/j.scriptamat.2014.01.001>

- [22] J.H. Park, H.S. Seo, K.Y. Kim, Alloy design to prevent intergranular corrosion of low-Cr ferritic stainless steel with weak carbide formers. *Journal of The Electrochemical Society*, 162(2015) C412–C418. <https://doi.org/10.1149/2.1001508jes>
- [23] G. Li, Z. Li, E. Rahimi, M. Muratori, A. Smith, M. J. Santofimia Navarro, Y. Gonzalez-Garcia, Pit initiation in quenching and partitioning processed martensitic stainless steels. *Electrochimica Acta*, 498(2024) 144646. <https://doi.org/10.1016/j.electacta.2024.144646> (Chapter 5)
- [24] G. Li, C. Kwakernaak, A. Smith, M. Muratori, Y. Gonzalez-Garcia, M. J. Santofimia, Microstructure development of quenching and partitioning-processed martensitic stainless steels with different manganese content. *Materials Science and Technology*, 40(2024) 449 – 465. <https://doi.org/10.1177/02670836231215989>
- [25] S. Hu, Y. Mao, X. Liu, E.H. Han, H. Hänninen, Intergranular corrosion behavior of low-chromium ferritic stainless steel without Cr-carbide precipitation after aging. *Corrosion Science*, 166(2020) 108420. <https://doi.org/10.1016/j.corsci.2019.108420>
- [26] M. Charleux, W.J. Poole, M. Militzer, A. Deschamps, Precipitation behavior and its effect on strengthening of an HSLA-Nb/Ti steel. *Metallurgical and Materials Transactions A*, 32(2001) 1635–1647. <https://doi.org/10.1007/s11661-001-0142-6>
- [27] X. Ma, C. Miao, B. Langelier, S. Subramanian, Suppression of strain-induced precipitation of NbC by epitaxial growth of NbC on pre-existing TiN in Nb-Ti microalloyed steel. *Materials & Design*, 132(2017) 244-249. <https://doi.org/10.1016/j.matdes.2017.07.006>
- [28] J. Webel, H. Mohrbacher, E. Detemple, D. Britz, F. Mücklich, Quantitative analysis of mixed niobium-titanium carbonitride solubility in HSLA steels based on atom probe tomography and electrical resistivity measurements. *Journal of Materials Research and Technology*, 18(2022) 2048-2063. <https://doi.org/10.1016/j.jmrt.2022.03.098>
- [29] Z. Zeng, C. Li, Z. Li, Y. Zhai, J. Wang, Z. Li, Effect of Nb content and thermal deformation on the microstructure and mechanical properties of high-strength anti-seismic rebar. *Materials Science and Engineering: A*, 840(2022) 142929. <https://doi.org/10.1016/j.msea.2022.142929>
- [30] K. D. Ralston, N. Birbilis, Effect of grain size on corrosion: A review. *Corrosion*, 66(7)(2010) 075005–075005-13. <https://doi.org/10.5006/1.3462912>

# 7

## General Discussions and Conclusions



The aim of this thesis is to investigate the microstructure development of newly designed martensitic stainless steels during the quenching and partitioning (Q&P) process and elucidate the microstructure–corrosion relationships. Two different high carbon steels with varying manganese contents are analysed to understand the impact of Q&P heat treatment on microstructural evolution during the Q&P process using experiments and advanced simulations. Three different steels with varying carbon, manganese and microalloying elements are investigated to build the relationship between microstructure and pitting corrosion. Further, two high carbon, high manganese steels with/without microalloying elements are focused on studying the specific role of microalloying elements on corrosion behaviour. The current research has led to the fundamental understanding of the microstructural evolution during the Q&P processes of the martensitic stainless steels, mechanisms related to interface movement and competing reactions during the partitioning stage, and the microstructure–corrosion relationships. The key conclusions from individual chapters of this Ph.D. thesis are summarised as follows.

- Chemical segregation leads to microstructural heterogeneity, which forms martensite and austenite bands. The increasing addition of Mn and its chemical segregation leads to a larger heterogeneous distribution of carbon and a larger Ms temperature scatter between bands. The carbon concentration in austenite after the partitioning step calculated assuming full carbon partitioning from martensite to austenite overestimates the actual carbon enrichment observed in austenite. This is due to the precipitation of carbides, including precipitates at prior austenite grain boundaries that formed during the first quenching and small particles inside tempered martensite grains that formed during partitioning. These precipitates consume carbon that is no longer available to partition into austenite (Chapter 3).
- Investigations showed the elimination of microstructural bands after partitioning for 5 minutes at 400 °C in a 3C HMn alloy. Quenching to room temperature and partitioning at 400 °C allows distinctly separate quenching and partitioning stages, facilitating a focused examination of the pure partitioning behaviour. A partitioning model, considering carbon interface partitioning, carbon diffusion, and interface migration, explains the evolution mechanism of banding microstructure elimination. The increasing manganese content accelerates banding microstructure elimination because eliminating the bands is influenced by both the local (microstructural heterogeneity) and global equilibrium (phase fraction evolution). Decreasing the global equilibrium leads to a slower elimination of the bands. Altogether, the high manganese steel under local equilibrium-negligible partitioning (LENP) conditions brings the most realistic outcome, where banding elimination, although slower, occurs. At the same time, the global fractions are closer to the experimentally observed (Chapter 4).

- Irrespective of the chemical composition and phase fraction, localised corrosion initiation in Q&P processed martensitic stainless steels is predominantly governed by the presence of inclusions. The lower surface potential at MnS results in selective dissolution of the MnS site, while the higher surface potential at TiN results in selective dissolution at the interface between TiN and the matrix. The corrosion resistance of three steels is investigated by combining ex-situ and in-situ electrochemical techniques, and the inclusion-induced pit corrosion mechanism is proposed (Chapter 5).
- Different corrosion mechanisms are observed when the inclusions are not predominant in the microstructure. For this case, the precipitation of Cr-carbides at prior austenite grain boundaries plays a deceiving role and intergranular corrosion induced by Cr-carbides precipitation is dominant. The presence of TiN(Nb) particles, when also present together with the Cr-carbides at prior austenite grain boundaries, intensifies the susceptibility of the steel to intergranular corrosion attack (Chapter 6).

This thesis provides a broader understanding of the microstructural evolution, microstructure–corrosion relationship and mechanisms involved in the Q&P process. However, it simultaneously opened up new challenges that can be further investigated:

- In Chapter 3, the CCE model has been effectively used to study the partitioning stage during the Q&P process regarding competitive reactions. If the nature of the carbides precipitated during the partitioning stage can be characterised by high-resolution transmission electron microscopy (HR-TEM) observations, quantitative estimation of carbon partitioned into austenite and carbon consumed by carbides will be possible.
- In Chapter 4, both the experimental and simulation models elucidate the “martensite/austenite interface movement” involvement in partitioning. An in-situ experimental technique can help further clarify the effect of Mn on the interface movement. Additionally, the impact of carbides/competing reactions on austenite decomposition or martensite/austenite interface migration during the partitioning stage can also be studied.
- The investigated steels exhibit microstructural heterogeneity. On the one hand, optimising the smelting process before Q&P heat treatment can help generate a homogeneous microstructure and is conducive to the systematic study of the properties of a certain phase content. On the other hand, producing a uniform microstructure could be industrially challenging. Hence, it is highly recommended to study microstructure evolution during the Q&P process at different thickness levels of the steel.
- Although the final Q&P microstructures retain a significant fraction of austenite, the thermal and mechanical stability of these heat-treated alloys should be studied. This further

investigation will help determine the effectiveness of Q&P heat treatments on the designed stainless steels compared to other 3rd-generation advanced high-strength steels.

- Exploration of alternative alloying strategies: Building on the findings of this study, future work could focus on modifying alloy designs to further enhance material properties. This includes the careful incorporation of microalloying elements such as Nb and Ti to refine grain structures and optimise precipitation strengthening. The addition of these elements must be precisely controlled to achieve the desired strengthening effects while minimising excessive precipitation, which can lead to increased susceptibility to corrosion. Moreover, improving inclusion control is crucial for enhancing corrosion resistance. Additionally, high Mn content has been shown to improve hardenability, while careful attention to the material production process is essential to ensure a homogeneous chemical distribution and to prevent the formation of MnS inclusions.



# Appendix

## A: Supplementary Materials of Chapter 4

### 1. Model description

We use the model described in [1] without considering the segregation to defects, i.e. we consider the diffusion of carbon (concentration gradient-driven [2] and interface partitioning [3]. In particular, the redistribution of carbon is realised by numerically solving the carbon concentration  $x_{C,i}$  at each element  $i$  by the following expression for the “n<sup>th</sup>” iteration:

$$x_{C,i}^{n+1} - x_{C,i}^n = \sum_j^{p_i=p_j} A_{ij} \cdot (x_{C,j}^n - x_{C,i}^n) + \sum_j^{p_i \neq p_j} A_{ij} \cdot (x_{C,j}^n - x_{C,i}^{p_i,eq,p_j,n}) \quad (\text{A-1})$$

where in **Equation (A-1)**,

- $j$  is index indicating that it is an element neighbour to  $i$ .
- $p_i$  is the phase, taking values of 0 (FCC) and 1 (BCC).
- $A_{ij}$  is the rate factor, a constitutive state variable, as it depends not only on the mesh size and time step but also on the local phase due to the diffusivity of carbon being different for the two lattices [4],[5].

As for the interface migration, this is simulated based on the local driving forces, by employing a deterministic cellular automata method. The switching rate at each cell  $i$  based on [6] is:

$$1/\delta t_{g_i \rightarrow g_j} = M_{g_i \rightarrow g_j} \cdot \frac{\sum_k \bar{F}_{ik}}{V_i} \quad (\text{A-2})$$

where in **Equation (A-2)**,

- $k$  is index representing that cell  $k$  is also (like  $j$ ) neighbour to cell  $i$ .
- $M_{g_i \rightarrow g_j}$  is the mobility of the boundaries migrating toward element  $i$  – assumed here equal everywhere.
- $V_i$  is the volume of cell  $i$ .
- $\delta t_{g_i \rightarrow g_j}$ : the time required for the boundaries to sweep the volume of  $i$  and hence to switch the state variable (here crystal orientation and phase) accordingly.

The driving force arises from the chemical potential difference of the substitutional lattice in BCC and FCC [7], and hence the force at each boundary is:

$$\bar{F}_{ij} = (\mu_{Fe,j} - \mu_{Fe,i}) \cdot A_{ij} \quad (\text{A-3})$$

where  $A_{ij}$  is the area of boundary  $ij$ .

## 2. Model tests – uniform shrinkage/expansion

This section investigates the model's applicability using the inputs of **Table 4.2** with the aim of testing the effects of grid anisotropy. As for the global equilibrium, the austenite carbon concentration is expected to be 3.8 wt. % and the austenite fraction equal to 0.08.

**Figures A and B** show the simulation evolution in a case where the starting austenite fraction compared to the equilibrium value is higher and smaller, respectively. As shown, the austenite full equilibrium fractions (and thus carbon concentration) are reached in both cases. Most importantly, in both cases, i.e. expansion and shrinkage, the circles grow/shrink uniformly, thus confirming that for the present input values, the simulations are not biased against modelling (grid) artefacts.

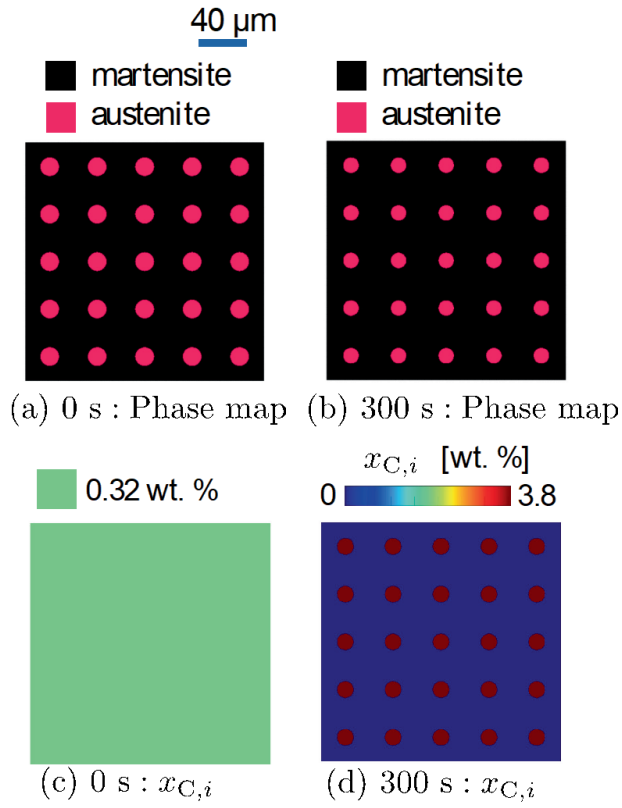


**Figure A.** Simulation of carbon redistribution and interface migration in uniform representative volume element (RVE); The initial austenite fraction is equal to 13%. The top row (i.e. (a), (b)) shows the phase maps and the bottom row (i.e. (c), (d)) the carbon concentration.

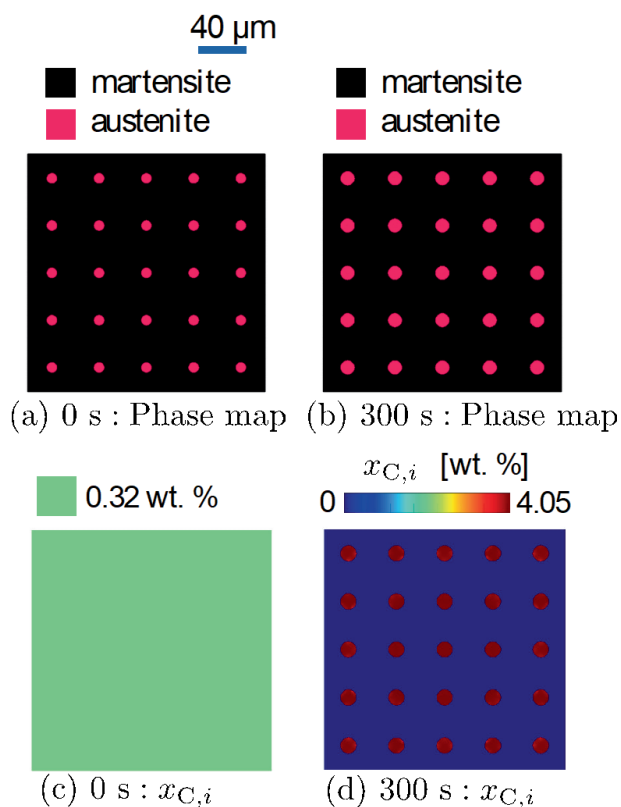
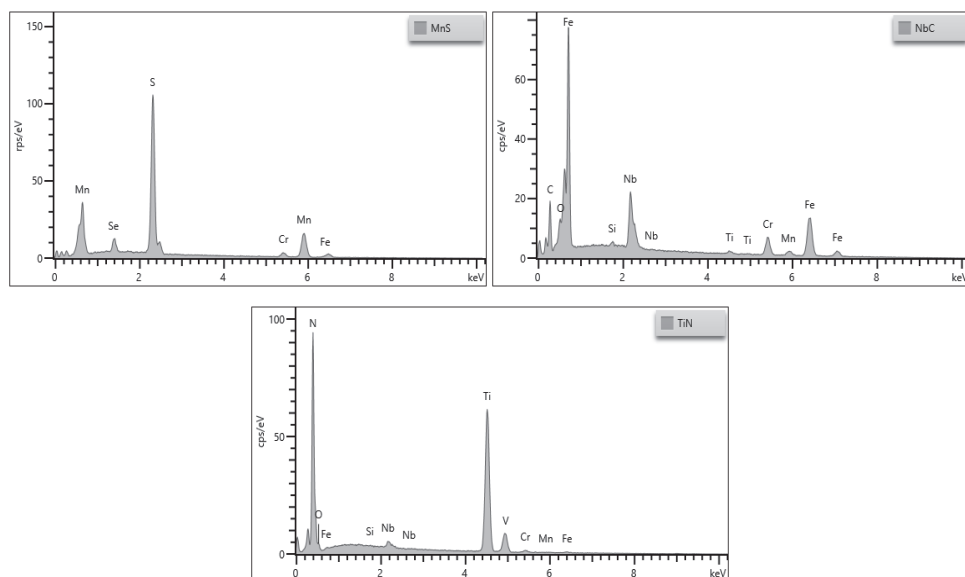


Figure B. Simulation of carbon redistribution and interface migration in uniform RVE; The initial austenite fraction is equal to 5%. The top row (i.e. (a), (b)) shows the phase maps and the bottom row (i.e. (c), (d)) the carbon concentration.

## B: Supplementary Materials of Chapter 5



**Figure S1.** EDS analysis particles detected in SEM images (a) black round particles MnS in alloys 2C LMn, 3C LMn, 3C HMn-NbTi (b) white round particles NbC in alloy 3C HMn-NbTi, (c) black rectangle particles TiN in alloy 3C HMn-NbTi.

## References

- [1] K. Traka, J. Sietsma, M. J. Santofimia, Modeling the interaction of carbon segregation to defects and carbon partitioning in multiphase steels, *Acta Mater.*, 277(2024) 120204. doi: 10.1016/j.actamat.2024.120204.
- [2] A. Fick, Ueber Diffusion, *Ann. Phys. Chem.*, 170(1) (1855) 59–86. doi: 10.1002/andp.18551700105.
- [3] S. Matas, R. F. Hehemann, Retained austenite and the tempering of martensite, *Nature*, 187(4738) (1960) 685–686. doi: 10.1038/187685a0.
- [4] J. Agren, Diffusion in phases with several components and sublattices, *J. Phys. Chem. Solids*, 43(5) (1982) 421–430. doi: 10.1016/0022-3697(82)90152-4.
- [5] J. Agren, A revised expression for the diffusivity of carbon in binary Fe-C austenite, *Scr. Metall.*, 20(11) (1986) 1507–1510. doi: 10.1016/0036-9748(86)90384-4.
- [6] K. Traka, K. Sedighiani, C. Bos, J.G. López, K. Angenendt, D. Raabe, J. Sietsma, Topological aspects responsible for recrystallization evolution in an IF-steel sheet – Investigation with cellular-automaton simulations, *Comput. Mater. Sci.*, 198 (2021) 110643. doi:10.1016/j.commatsci.2021.110643.
- [7] M. J. Santofimia, L. Zhao, J. Sietsma, Model for the interaction between interface migration and carbon diffusion during annealing of martensite–austenite microstructures in steels, *Scr. Mater.*, 59(2) (2008) 159–162. doi: 10.1016/j.scriptamat.2008.02.045.

## Acknowledgement

At the end of thesis, I would like to acknowledge and express my gratitude to all the parties that supported me during the research from 2019 to 2023.

I am very grateful for the guidance from my supervisors at TU Delft. I would like to thank Prof. dr. Maria J. Santofimia Navarro for she has been amazing promotor. The trust, support and freedom she offered me during this journey have let me develop as a confident, independent researcher. I also would like to thank my daily supervisor and co-promoter, Dr. Yaiza Gonzalez-Garcia for her professional and efficient support during this journey. This thesis would not have been the same without you. I thank you for all those wonderful scientific discussions, for being patient in explaining things to me, and especially for providing great support during the Covid times.

I express my gratitude to European Commission and Research Fund for Coal and Steel (RFCS) for funding this project, QPINOX (proposal number: 847195). I would like to thank my project partners, Dr. Ali Smith (RINA, Italy), Marta Muratori (ACERINOX, Spain), Dr. Ilchat Sabirov (IMDEA, Spain), and Andres Sierra-Soraluce (IMDEA, Spain) for all those discussions during our meetings.

I extend my appreciation to the members of my thesis committee: Prof. dr. ir. Erik Schlangen, Prof. dr. ir. Roumen Petrov, Prof. dr. Iris De Graeve, and Dr. David San Martin, for their valuable insights and constructive feedback, which greatly improved the quality of this thesis.

Throughout the course of my project, I received a great deal of support and assistance from numerous individuals. I have been deeply thankful for our secretary, Prisca Koelman's unwavering support. She's taken care of every detail, making sure my transition to the Netherlands went smoothly and that life and work here stayed on track. Throughout my four years as a PhD student, she's been there every step of the way. Her support and dedication mean the world to me and are something I'll always treasure. In addition, I am deeply grateful to Prof. dr. ir. Jilt Sietsma for the valuable discussions and his meticulous review of this thesis, particularly his detailed insights on the summary and *samenvatting*. I would like to thank Ehsan and Ziyu for assisting performing part of experimental tests; Konstantina for providing simulation model and being an amazing co-author; and Zhaoying for sharing experience in preparing dissertation and defence. I would also like to thank the colleagues at Vrije Universiteit Brussel, Reynier and Xinhua, for the knowledge transfer, training and guidance during my visit in Belgium.

It has been an incredible experience working with colleagues/friends from different parts of the world. I greatly acknowledge the conversations with Sudhindra, Vibhor, Ankit, Farnaz, Soroush, Jithin, Aravind, Jaji, Prasaanth, Prasad, Viviam, Arthur, John and Daniel, helped me learn many things. The greatest appreciation goes to my office mate Dr. Vitoria Mattos Ferreira whom I cannot thank enough for all the love, support and affection. Although I have been quite far from my family in China, I seldom felt it that way. You have been like a real family far from home.

I would like to thank my Chinese friends: Meng, Yuliu, Wei, Quanxin, Jianing, Zhaorui, Xiaohui, Keer, Jiayang, Kai, Yue (Li), Xukai (Zhang), and Bin (Chen), you guys have filled me with love and peace whenever we met, thank you for being with me during this journey. I also would like to thank my lifelong friends in China: Shichao, Pingjie, Pengfei, Weisheng and Teng, you will always be special people in my life. A very special thanks to my previous supervisor, Prof. dr. Mingxing Guo, for guiding me into academia and being the belief and pillar in many aspects.

I offer my deepest gratitude to my family, whose love and support have been my guiding light throughout this journey, especially during the four years I was unable to go home. To my parents, thank you for instilling in me the courage to face every challenge that came my way. I am especially grateful to my younger brother, Yuyang, who has always been my most faithful and understanding listener. My heartfelt thanks also go to my partner, Xi, whose companionship and shared burdens have been a source of comfort in the darkest of times. No words can truly capture the depth of your support, which has carried me through the trials and triumphs alike.

At journey's end, to the self who began, to the self who persevered, and to the self who stands here today: thank you.

# Curriculum Vitae

## Gaojie LI

Born on October 10, 1993, in Rizhao Shandong, China

### Professional Experience

- |                    |   |
|--------------------|---|
| 06.2024 – present  | Postdoc. Researcher<br>Delft University of Technology<br>Project: Optimisation of Metal-Based Electrodes/Electrocatalysts for Energy Application                  |
| 09. 2019 – 11.2023 | Ph.D. Researcher<br>Delft University of Technology<br>Project: Development of New Martensitic Stainless Steels for Automotive Lightweight Structural Applications |

### Education

- |                   |  |
|-------------------|--|
| 09.2019 – 11.2023 | Ph.D. in Materials Science and Engineering<br>Faculty of Mechanical Engineering<br>Delft University of Technology, The Netherlands                           |
| 09.2016 – 01.2019 | Master of Materials Science and Engineering<br>State Key Laboratory for Advanced Metals and Materials<br>University of Science and Technology Beijing, China |
| 09.2012 – 06.2016 | Bachelor of Materials Science and Engineering<br>School of Materials Science and Engineering<br>University of Science and Technology Beijing, China          |

### Languages

- |         |   |
|---------|---|
| Chinese | Native                                  |
| English | Advanced. Full Professional Proficiency |
| Dutch   | NT2 – niveau A2                         |



## List of Publications

### Journal Papers

1. **Gaojie Li**, Ali Smith, Maria J. Santofimia Navarro, Yaiza Gonzalez-Garcia. *Intergranular Corrosion of TiNb-microalloyed Martensitic Stainless Steels Produced by Quenching and Partitioning*. Submitted. 2024.
2. **Gaojie Li**, Maria Santofimia, Yaiza Gonzalez-Garcia. *Competition Between Banding-Selective Corrosion and Intergranular Corrosion in Q&P-Treated Stainless Steels*. To be Submitted.
3. **Gaojie Li**, Ziyu Li, Ehsan Rahimi, Marta Muratori, Ali Smith, Maria J. Santofimia Navarro, Yaiza Gonzalez-Garcia. *Pit initiation in quenching and partitioning processed martensitic stainless steels*. *Electrochimica Acta*. 2024; 498:144646.
4. **Gaojie Li**, Konstantina Traka, Kees Kwarkernaak, Yaiza Gonzalez-Garcia, Maria Santofimia. *Modelling the evolution of microstructural bands in a martensite/austenite Q&P-processed stainless steel*. *Scripta Materialia*. 2025; 257:116457.
5. **Li G**, Kwarkernaak C, Smith A, Muratori M, Gonzalez-Garcia Y, Santofimia MJ. *Microstructure development of quenching and partitioning-processed martensitic stainless steels with different manganese content*. *Materials Science and Technology*. 2024; 40(6):449-465.
6. Ziyu Li, **Gaojie Li**, Peter Visser, Axel Homborg, Yaiza Gonzalez-Garcia, Arjan Mol. *Local scanning electrochemical microscopy analysis of a lithium-based conversion layer on AA2024-T3 at progressive stages of formation*. *Electrochimica Acta*. 2023; 469:143270.
7. A. Sierra-Soraluce, **G. Li**, M.J. Santofimia, J.M. Molina-Aldareguia, A. Smith, M. Muratori, I. Sabirov. *Exploring the effect of complex hierarchic microstructure of quenched and partitioned martensitic stainless steels on their high cycle fatigue behaviour*. *Materials & Design*. 2023; 233:112286.
8. A. Sierra-Soraluce, **G. Li**, M.J. Santofimia, J.M. Molina-Aldareguia, A. Smith, M. Muratori, I. Sabirov. *Effect of microstructure on tensile properties of quenched and partitioned martensitic stainless steels*. *Materials Science and Engineering: A*. 2023; 864: 144540.

## Conferences

1. **Gaojie Li**, Kees Kwakernaak, Marta Muratori, Ali Smith, Maria Santofimia, Yaiza Gonzalez-Garcia. *Corrosion Properties of Quenching and Partitioning-Processed Martensitic Stainless Steels*, 2023 ECS - The Electrochemical Society. Meet. Abstr. MA2023-02 1052.
2. **Gaojie Li**, Kees Kwakernaak, Ali Smith, Marta Muratori, Maria Santofimia, Yaiza Gonzalez-Garcia. *Intergranular Corrosion of Q&P Processed Martensitic Stainless Steels*, EUROCORR 2023 – Oral Presentation.
3. **Gaojie Li**, Kees Kwakernaak, Ali Smith, Marta Muratori, Yaiza Gonzalez-Garcia, Maria Santofimia. *Martensitic Transformation Kinetics in Q&P Processed Martensitic Stainless Steels with the Existence of Segregation Bands*, THERMEC'2023 – Oral Presentation.
4. **G. Li**, A. Sierra-Soraluce, Y. Gonzalez-Garcia, I. Sabirov, J.M. Molina-Aldareguia, A. Smith and M.J. Santofimia. *Mechanical Stability of Retained Austenite in Q&P Processed Martensitic Stainless Steels*, MSE 2022 – Oral Presentation.
5. **Gaojie Li**, Leon Crousens, Adnan Akman, Benne de Bakker, Kees Kwakernaak, Maria Santofimia, Yaiza Gonzalez-Garcia. *Corrosion Behaviour of Quenched and Partitioned Martensitic Stainless Steel: Effect of Composition and Microstructure*, EUROCORR 2022 – Oral Presentation.
6. **Gaojie Li**, Yaiza Gonzalez-Garcia, Kees Kwakernaak, Maria J. Santofimia. *Thermal Stability of Retained Austenite of Martensitic Stainless Steels Treated by Quenching and Partitioning*, EUROMAT 2021 – Oral Presentation.

*“For darkness restores what light cannot repair.”*

— Joseph Brodsky

